STUDY OF HIERARCHY AND PORE ARCHITECHTURE OF POROUS MATERIALS

by

Poroshat Taheri

DISSERTATION

Presented to the Faculty of the Graduate School of The University of Texas at Arlington in Partial Fulfillment of the Requirements for the Degree of

DOCTOR OF PHILOSOPHY

UNIVERSITY OF TEXAS AT ARLINGTON

May 2021

Supervising committee:

Dr. Peter Kroll, Supervising Professor

Dr. Frederick MacDonnell

Dr. Daniel Armstrong

Dr. Junha Jeon

DEDICATION

I would like to dedicate this thesis to my dearest father, Dr. Parviz Taheri, who has fought bravely with Coronavirus disease 2019 (COVID-19) as well as my adamant mother, Mrs. Parvin Bayareh, who has stood next to my father with her unconditional love and has taken care of him though she was also infected with the disease while I was writing this work miles away from them.

AKNOWLEDGEMENTS

First, I would like to express my gratitude to my advisor Professor Peter Kroll, who provided me with continuous support and opportunities through my doctorate degree. I am truly thankful for all the projects and conferences that I had the opportunity to experience, as well as the freedom and trust to develop my researcher skills in my doctorate degree.

I specially want to thank Dr. John Lang, for giving me the opportunity to work with him. I learned a lot from his skills and he always provided me his continuous support and knowledge. I am also very grateful for collaborating with Micromeritics, especially Dr. Jeff Kenvin, as well as having the opportunity to work and research there as an intern. I would like to thank everyone at UTA who help me throughout my degree: Dr. Edwards and Dr. McDougald who helped me to maintain lab instruments. I also want to thank all my amicable group members, Ms. Akshada Hande, Ms. Hanof Alkhaldi, and Mr. Shariq Haseen, for their assistance and support. I also want to thank the departmental staff, Ms. Stephanie Henry, Ms. Jill Howard, and Ms. Debbie Cooke, at UTA for their hard work. Many thanks to the undergraduate students, Ms. Kendall Hendrix, and Ms. Karissa Cordero, who I had the honor to train and introduce them to research skills.

I want to thank my beloved parents for their unconditional love. It was such a hard decision for them to see their young daughter leaving them to study abroad and finding her fortune in another

country, but they have always supported me, encouraged me, and provided me with the necessary strength to always keep going. I could not have done it without them. I want to thank my beloved sister, Dr. Pantea Taheri, who has decided to take care of and live with the family while I was miles away from home. Finally, I want to thank my darling husband, Dr. Jonathan Cole, for his supportive love. Hardly I could accomplish this journey without him.

ABSTRACT

STUDY OF HIERARCHY AND PORE ARCHITECHTURE OF POROUS MATERIALS

Poroshat Taheri, PhD

University of Texas at Arlington, 2020

Supervising Professor: Peter Kroll

Research to design, synthesize, and characterize porous materials is a rapidly growing field due to porous materials' potential use in a wide range of applications. For any application, insights into the structure formation parameters and properties relating to those parameters are highly desired. This thesis deals with the combination of two classes of materials, aerogels and polymer-derived ceramics. Polymer Derived Ceramics (PDCs) are processed using liquid-based, hydrocarbon polymeric precursors at lower temperature, followed by heat treatments at higher temperature. Silicon oxycarbide (SiCO) is one type of PDC. Various types and ranges of porosity can be introduced into SiCO when using sol-gel methods of synthesis. These adaptations can be exploited for different applications such as gas separation membranes, environmental remediation, or lithium-ion storage. Such porous SiCO aerogels are the focus of this study.

The choice of precursors. synthesis conditions, and post-synthesis processing influence unique physical and chemical properties of the final SiCO ceramics by introducing specific microstructure, porosity, content of free carbon, and specific surface are. This report of the research consists of three sections: effect of synthesis conditions on porosity, the interdependence of the assessment of microstructure and the techniques utilized for evaluating it, and the role of precursor role on the composition of SiCO and the resulting microstructure. In the first section we investigate the effect of the synthesis solvent, as one of the important synthesis conditions, and its systematic correlation with Hansen Solubility Parameters (HSP) with the resulting SiCO microstructure. In the second section, we apply different methods for characterizing porosity, highlighting a recently developed technique known as Differential Hysteresis Scanning (DHS) to quantify hierarchical connectivity in two SiCO aerogels. This technique contrasts strikingly the structures obtained from two different solvents used in the synthesis, and characterizes their respective changes on pyrolysis to 1000 °C. Finally, we study a novel crosslinking agent as a substitute for DVB to explore the possibility of new microstructures, functionalities, and different chemical compositions of the SiCO ceramics before and following calcination.

TABLE OF CONTENTS

LIST OF FIGURES AND TABLES

LIST OF ABBREVIATIONS

IUPAC:	International Union of Pure and Applied Chemistry
MOFs:	Metal Organic Frameworks
COFs:	Covalent Organic Frameworks
SSA:	Specific Surface Area
BET:	Brunauer–Emmett–Teller
PSD:	Pore Size Distribution
HK:	Horvath-Kawazoe
DFT:	Density Function Theory
MC:	Monte Carlo
BJH:	Barrett-Joyner-Halenda
MIP:	Mercury Intrusion Porosimetry
CT:	Computerized x-ray Tomography
MRI:	Magnetic Resonance Imaging

TEOS:	Tetraethyl orthosilicate
DCCA:	Drying Control Chemical Additives
PDC:	Polymer Derived Ceramic
PIP:	Polymer Infiltration Pyrolysis
SiC:	Silicon carbide
SiCO:	Silicon Oxycarbide
SiCN:	Silicon Carbonitride
NLDFT:	Non-Local Density Function Theory
PMHS:	Polymethylhydrosiloxane
DVB:	Divinylbenzene
DVT:	Divinylthiophene
HF:	Hydrofluoric acid
PTFE:	Polytetrafluoroethylene
RED:	Relative Energy Distance
HSP:	Hansen Solubility Parameter
PDMS:	Polydimethylhydrosiloxane
TEM:	Transmission Electron Microscopy

SEM:	Scanning Electron Microscope
DHS:	Differential Hysteresis Scanning
MW:	Molecular Weight
TVP:	Total Pore Volume
LPH:	Low Pressure Hysteresis
NNLS:	Non-Negative Least Squares
TMTV:	2,4,6,8-tetramethyl2,4,6,8-tetravinylcyclotetrasiloxane
TGA:	Thermogravimetric Analysis
TG-MS:	Thermal Gravimetric Mass Spectrometry
FT-IR:	Fourier-Transform Infrared spectroscopy
EDS:	Energy-Dispersive X-ray spectroscopy
ATR:	Attenuated Total Reflectance
TTT:	1,3,5-triallyl-1,3,5-triazine-2,4,6 (1H,3H,5H)-trione
IC:	Ion Current
TIC:	Total Ion Current
QMD:	Quadrupole Mass spectrometer Detector
DTA:	Differential Thermal Analysis

CHAPTER I: INTRODUCTION

1.1 Porous Materials

Porous materials exist in nature abundantly. They play significant roles in human biology, being integral to the structure of bone tissue and in skin, allowing us to balance our body temperature. Porous materials are also important in areas such as chemistry,[1] materials engineering,[2] the oil industry,[3] and geology.[4] As a standard, the International Union of Pure and Applied Chemistry (IUPAC), states that a material can be defined as porous "…when it contains pores, *i.e.* cavities, channels or interstices, which are deeper than they are wide."[5]

Porous materials can arise in different ways. In one pathway, particles may bond together weakly to form a loosely consistent secondary particle called an aggregate.[1, 6] Aggregates can then consolidate to form agglomerates. The empty spaces/voids among aggregates may have different geometries as illustrated in Figure 1-1.

a)

b)

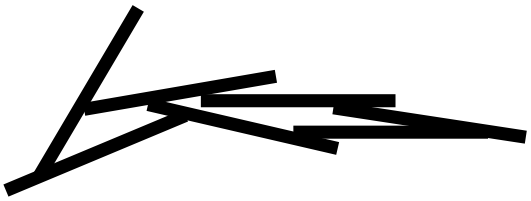

Figure 1-1. Different types of aggregates generating pores: a) spherical particles; b) plate- like particles.

Some materials may also be porous by virtue of their crystal structure. Zeolites,[7] metal organic frameworks (MOFs),[8] and covalent organic frameworks (COFs)[9] all contain cavities naturally arising within their crystal structure and therefore belong in this category.

Finally, pores can be generated by selective removal of elements from an original, non-porous structure. For example, chemical etching and thermal decomposition are common methods of generating pores in some materials, including silicon oxycarbide.[10]

IUPAC classifies pores according to their accessibility to an external fluid.[10] Different morphologies of pores are shown in Figure 1-2. Closed pores (a) are completely isolated and are not connected to the exterior surface of the material. This type of pore therefore cannot participate in gas sorption. Pores that do have continuous access to the external surface are called open pores and may either be open at one end only, in which case they are subcategorized as blind pores (b and f), or they are open from both ends, in which case they are subcategorized as through pores (c, d, and e, all of which are connected in a network). The roughness of an external surface (g) is considered porous only when it contains irregularities that are deeper than they are wide.

A separate categorization of pores is based on their shape: cylindrical (c, e, and f in Figure 1-2, and I in Figure 1-3), bottleneck (b in Figure 1-2, and III in Figure 1-3), slit (II in Figure 1-3), or wedge (d in Figure 1-2, and IV in Figure 1-3).

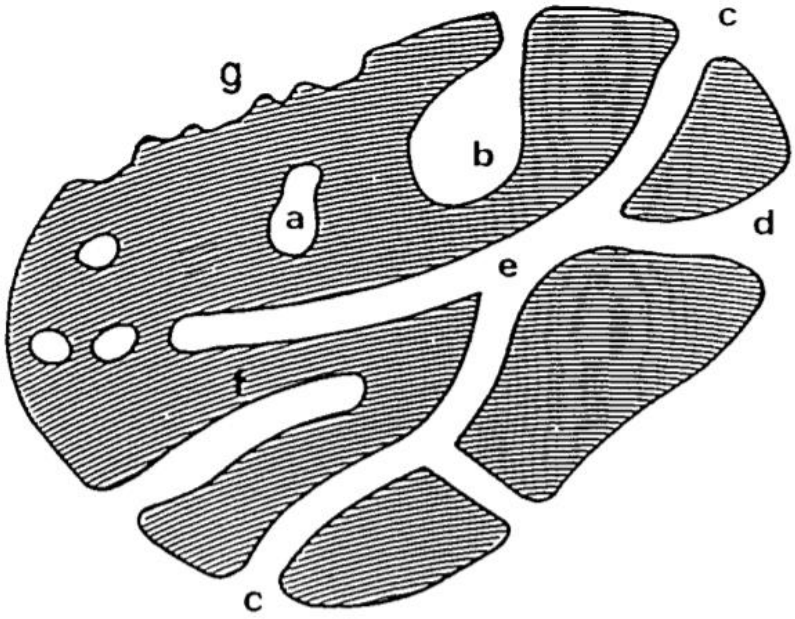

Figure 1-2. Schematic cross-section of a porous solid. (a) Closed pore, (b) & (c) Open blind pores (open only at one end), (d) through pores, and (e) surface roughness. Figure adopted from Raquel *et al.* 1994.[11]

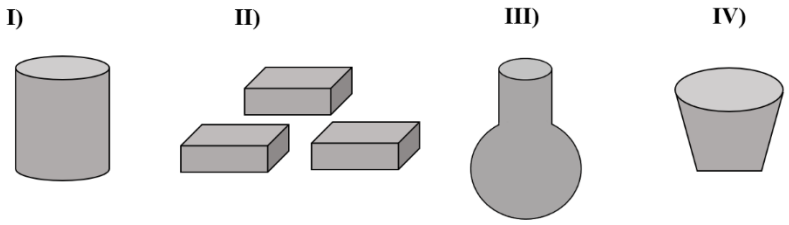

Figure 1-3. Different pore shapes: I) cylindrical, II) slit, III) bottleneck, IV) wedge.

1.2 Quantification of Porous Systems

Porous systems are quantitatively described by porosity, specific surface area, and size.

1.2.1 Porosity

Porosity is defined as a fraction (ε):

$$\varepsilon = \frac{V_p}{V} \tag{1-1}$$

where V_p is the cumulative total volume of pores within the sample and V is the apparent volume of the sample (volume without interparticle voids). The measured value of porosity can vary depending on the method used to determine volumes V_p using gas sorption, mercury intrusion, radiation scattering *etc.* and V via helium pycnometer (true density measurement) or bulk/geometry density measurement.[10] It can also depend on the size of the probe, *i.e.*, the adsorbate molecule size, wavelength of radiation, *etc.*

1.2.2 Specific Surface Area

Specific surface area (SSA) is defined as the area of solid surface available to fluid adsorption per unit mass of material. Like porosity, its measured value also depends on the method that is used and on the size of the probe. In addition, different mathematical models are used for interpretation of raw data to calculate the SSA of a material. The Brunauer-Emmett-Teller (BET) model is the most common and is critically dependent on identification of the completion of the monolayer,[12] while other empirical models include the t-method[13] and the a_s-method.[14-15]

1.2.3 Pore Size

IUPAC classifies pores according to their physical size: pores having widths less than 2 nm are called micropores, those having widths between 2 and 50 nm are called mesopores, and those

having widths larger than 50 nm are called macropores.[16-17] However, the precise shape of a pore can render it impossible to classify according to one single characteristic dimension. Pore shapes are most often highly irregular (Figure 1-2). Moreover, pores of different sizes can exist within an interconnected network. Therefore, different models allowing for pore geometries with varying degrees of connectivity have been established,[17] and pore size distributions are estimated based on the pore geometry assumed within the applied model (*e.g.*, cylindrical, bottleneck, slit-shaped, *etc.*). A selection of these models is escribed in Section 1.4.

1.3 Adsorption and Desorption

Adsorption is the accumulation of molecules, atoms, or ions in the vicinity of an interface. In fluid/solid systems, adsorption takes place in the vicinity of the solid surface and outside the solid structure (called the 'interfacial layer' or 'adsorption space').[18] Adsorbate is the material in the adsorbed state, while the adsorptive is the same component in the fluid phase. Desorption is the opposite of adsorption, *i.e.*, the loss of fluid from the same region. Depending on their size and geometry, porous materials can exhibit hysteresis, in which the amount of fluid accumulated on a porous surface at some equilibrium pressure depends on the direction from which that equilibrium pressure was approached.[18-19] Hysteresis is identified as the lack of coincidence of the adsorption and desorption branches of the isotherm. This is generally attributed to the effects of pore condensation and surface tension at constricted geometries and is described in greater detail in Section 1.3.2.

1.3.1 Chemisorption and Physisorption

Chemical adsorption, or chemisorption, occurs when the interactions between the solid phase and fluid phase form chemical bonds. This type of adsorption is necessarily limited to a monolayer given a finite number of reactive sites being present on a solid surface. A chemisorbed molecule undergoes either a reaction or dissociation process upon desorption, thus losing its original identity. The energy (which is associated with enthalpy of adsorption, ΔH(ads)) of chemisorption is equivalent to the energy associated with the exchange of chemical bonds, just as in conventional chemical reactions. Similarly, some activation energy must often be overcome to achieve chemisorption that depends on the temperature of the system.

On the other hand, physical adsorption, or physisorption, occurs when the interactions between the solid phase and fluid phase are constituted by physical forces such as van der Waals forces. The species interacting with the solid surface retains its identity upon adsorption. With increasing pressure, physisorption generally results in a multilayer since the attractive force of the solid surface can extend beyond one or more layers of adsorbed fluid. Physisorption is always an exothermic process, and the adsorption energy generally is not much larger than the energy of condensation of the adsorptive.[20] The experiments expounded upon in this work exclusively regard physisorption processes.

1.3.2 Adsorption-Desorption Isotherms

In a given gas-solid system, the amount, n^a, of gas adsorbed by mass, m^s, of solid is dependent on the temperature, T, and equilibrium pressure, p, of the system:

$$\frac{n^a}{m^s} = f(p, T) \tag{1-2}$$

If the gas is held at a constant *T* below the critical temperature, the equation (1-2) becomes

$$\frac{n^a}{m^s} = f\left(\frac{p}{p_0}\right)_T \tag{1-3}$$

where p_0 is the saturation pressure of the adsorptive at temperature T. Equation 1-3 represents the adsorption isotherm of the system, the functional form of which can be experimentally obtained and presented in graphical form.[5]

Various characteristic shapes of experimental adsorption isotherms have been recorded in the literature for many different gas–solid systems. Useful preliminary information can be inferred about the pore structure of the adsorbent by simple inspection of these shapes, even before any precise calculations have been applied. IUPAC has classified isotherm shapes into eight groups, illustrated in Figure 1-4.[21]

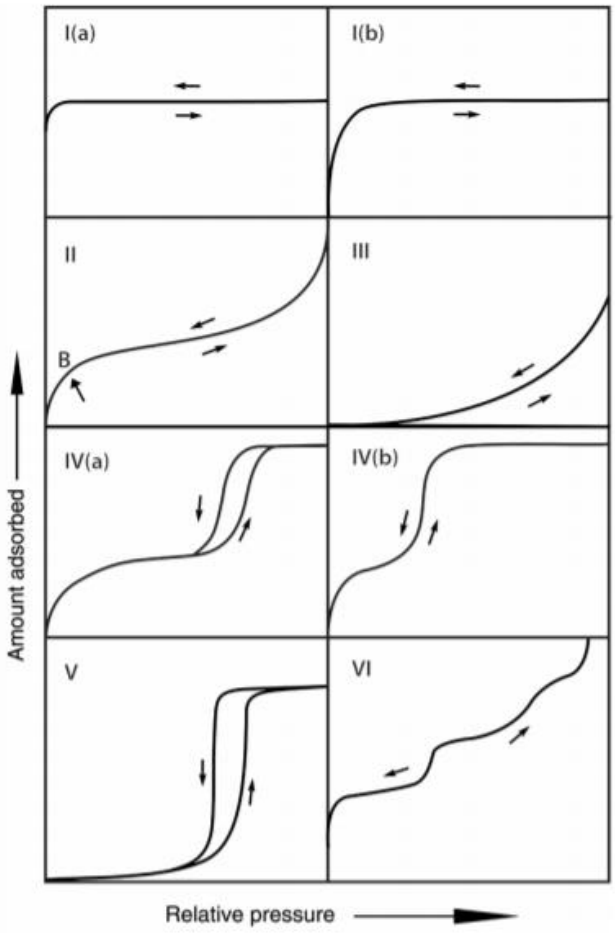

Figure 1-4. Classification of physisorption isotherms. Adopted from Thommes *et al*. 2015.[18]

Microporous solids (where the pore widths are smaller than 2 nm) and narrow mesopores (where the pore widths are smaller than 2.5 nm) which have most of their surface area contained within pores instead of on their external surface exhibit reversible Type I isotherms. This type of isotherm is concave down to the $\frac{p}{p_0}$ axis, and the adsorption amount approaches a limit determined by the accessible micropore volume. Strong adsorbent-adsorbate interactions cause increase in the adsorption energy within these very narrow micropores allowing them to have high uptake at very

low $\frac{p}{p_0}$. Once they are filled at very low relative pressures, the amount adsorbed does not increase at higher $\frac{p}{p_0}$ as there is very little external surface area available; hence, there is a plateau in the isotherm. Type I(a) isotherms arise in materials having mainly narrow micropores of width less than 1 nm while Type I(b) isotherms arise in materials with relatively wider micropores or narrow mesopores. Activated carbons and molecular sieve zeolites as well as some porous oxides exhibit reversible Type I isotherms.[18, 20]

Most gases on nonporous or macroporous adsorbents yield reversible Type II isotherms. The Type II shape is the result of unrestricted monolayer and multilayer adsorption all the way up to $\frac{p}{p_0}$ = 1. When the equilibrium pressure equals to the saturation vapor pressure, the adsorbed layer becomes a bulk liquid or solid. This type of isotherm also features a segment concave to the $\frac{p}{p_0}$ axis at the low end which transitions into a nearly linear segment. Point B (concave curve down) in Figure 1-3 denotes this transition point, which is where formation of a monolayer nears completion and formation of a multilayer begins. The sharpness of Point B reflects how much overlap there is of monolayer and multilayer formation, with greater sharpness indicating less overlap. The thickness of the adsorbed multilayer then usually increases without limit as $\frac{p}{p_0}$ approaches 1. Porous clays, pigments, or cements usually exhibit reversible Type II isotherms.[18, 20]

In the case of Type III isotherms, there is no Point B transition as in Type II, indicating that there is no identifiable point at which monolayer formation completes. This occurs on nonporous or macroporous solids when their interactions with the adsorbate are weak, and the adsorbed molecules therefore cluster around the most favorable sites on the surface. Nitrogen adsorption on

polyethylenes exhibits this type of isotherm.[16] The amount adsorbed is finite as $\frac{p}{p_0}$ approaches 1.[18, 20]

Type IV isotherms occur in mesoporous materials. Both adsorbent-adsorbate interactions as well as adsorbate-adsorbate interactions in a condensed state within mesopores determine the shape of this type of isotherm. Type IV takes the same path as Type II during initial monolayer and multilayer formation on the mesopore walls, and this eventually gives way to pore condensation, whereby a gas condenses into a geometrically stabilized liquid-like phase inside of a pore despite being below the saturation pressure, p_0, of the bulk liquid. Typically, there is a final saturation plateau in the isotherm with variable length depending on maximum size of pores (unless, of course, there are any significant free flat zones). Oxide gels (*e.g.*, SiO_2, TiO_2, and ZrO_2), and silica and alumina molecular sieves exhibit this type of isotherm.[18, 20]

There are two subcategories of Type IV isotherms. In the case of a Type IV(a) isotherm, capillary condensation within specific pore geometries causes hysteresis. For hysteresis to occur, pores must exceed a certain critical width that is a function of temperature. As an example, adsorption of N_2 at 77 K, or of Ar at 87 K, within cylindrical pores will show hysteresis if those pores are wider than 4 nm.[22] Type IV(b) isotherms are observed in materials with mesopores smaller than 4 nm in width that are conical, with the tapered end being closed, or cylindrical in shape. Although capillary condensation still occurs within such pores, it does not result in hysteresis.[18, 20]

Type V isotherm takes the same path as Type III at low $\frac{p}{p_0}$ due to relatively weak adsorbent–adsorbate interactions, but at higher $\frac{p}{p_0}$ pores are filled by molecular clustering. The different

between Type III and this type of isotherm is that Type V mostly is associated with adsorption in mesoporous adsorbents, where condensation of the adsorbate (formation of bulk liquid) in the porous structure is possible. Water adsorption on hydrophobic microporous and mesoporous adsorbents typically exhibits Type V isotherms.[18, 20]

The reversible Type VI isotherm is step-like due to layer-by-layer adsorption on a highly uniform nonporous surface. The height of each step is proportional to the capacity of each adsorbed layer. The sharpness of each step, like Point B in Type II, indicates the level of overlap between formation of one layer and the next one. Adsorption of Ar or Kr at low temperature on graphitized carbon black yields this type of isotherm.[18, 20]

1.3.3 Hysteresis

Hysteresis loops appear in the multilayer stage of physisorption in isotherms. They are generally associated with capillary condensation and/or network effects. IUPAC has classified hysteresis shapes into five groups, illustrated in Figure 1-5.[21]

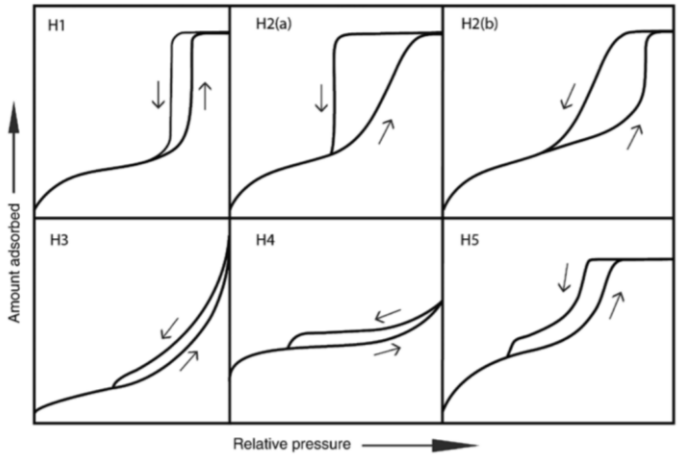

Figure 1-5. Classification of hysteresis. Adopted from Thommes *et al*. 2015.[18]

The Type H1 loop (Figure 1-5) is found in materials with a narrow range of uniform mesopores. Usually, capillary condensation is the main reason of the hysteresis. In general, hysteresis loops of Type IV(a) are attributable to capillary condensation in the mesopore regime where the capillary window is of more variable dimension.[23] The H1-Type hysteresis can be ascribed best to materials whose porosity consists of a narrow range of mesopores where the neck of these pores is only slightly narrowed as for instance in templated silicas (*e.g.* MCM-41, MCM-48, SBA-15), some controlled pore glasses and ordered, mesoporous carbons(depending on $\frac{p}{p_0}$).[18]

Hysteresis loops of Type H2 are given by more complex pore structures in which network effects are dominant. Type H2 has two sub-groups (Figure 1-5). Pore-blocking/percolation in a narrow range of pore necks or to cavitation-induced evaporation causes a very steep desorption branch in H2(a) loops as it can be observed in the hysteresis of many silica gels, some porous glasses (*e.g.*, vycor), and ordered mesoporous materials (*e.g.,* SBA-16 and KIT-5 silicas). Hysteresis of Type H2(b) appears in the isotherm of materials consisting of a greater differential in neck and pore size distributions. In applications this can result in not only a network or percolation effect, where transverse transport can be enhanced,[24] but also pore-blocking and, with processing such as annealing, cavitation or collapse.[23] This type of hysteresis loops has been observed in analyses of meso-cellular silica foams and certain mesoporous ordered silicas after hydrothermal treatment.[18]

Type H3 loop has two distinctive features as it is illustrated in Figure 1-5. One is that the adsorption branch resembles a Type II isotherm, and the other one is that the lower limit of the desorption branch has a characteristic desorption shoulder. Examples of this type of hysteresis loops have been observed with non-rigid aggregates of plate-like particles (*e.g*. clays) as well as

materials which their pore network consists of macropores that cannot be filled completely with pore condensate.[18]

The H4 loop has also two distinctive features. One is that the adsorption branch resembles a Type I isotherm, and the other one is that the lower limit of the desorption branch associated with the filling/desorption of micropores like Type II isotherm (Figure 1-5). This type can be observed often in the analyses of crystals of zeolites, some mesoporous zeolites, and micro-mesoporous carbons. [18]

Type H5 loop is typically uncommon (Figure 1-5). It has a distinctive form attributed to certain pore structures containing both open and partially blocked mesopores (*e.g.* plugged hexagonal templated silicas).[18]

1.4 Pore Size Distributions

IUPAC categorizes pores based on their sizes into 3 classes: micropores, mesopores, and micropores.

1.4.1 Micropores

In the micropore size range, various semi-empirical methods exist for estimating pore size distributions (PSDs), such as Horvath and Kawazoe (the HK method),[25] Saito and Foley,[26] and Cheng and Yang,[27] all of which typically underestimate actual pore sizes.[23, 28] A more accurate approach is based on the fundamental statistical mechanics of adsorption and phase behavior of fluids confined within well-defined pore structures. Density functional theory (DFT)[22] as well as

Monte Carlo simulation (MC)[29] are two well-known approaches to PSD analysis over the complete micropore range.

1.4.2 Mesopores

For many years, mesopore size distributions were analyzed primarily using the Kelvin equation.[30] The Kelvin equation describes the impact of curvature of a gas-liquid interface on the observed equilibrium vapor pressure of that liquid, in contrast with that liquid's equilibrium vapor pressure without any curvature. The Kelvin equation, which relates the change in Gibbs free energy of the liquid as a consequence of its curved surface to the corresponding change in its vapor, is

$$r_k = \frac{2v_m \gamma}{RTln\frac{p}{p_0}} \tag{1-4}$$

where r_k is the radius of curvature of the gas-liquid interface for a geometry of circular cross section perfectly wetting the confining solid, v_m is the molar volume of the gas phase, γ is the surface tension of the gas-liquid interface, R is the ideal gas constant, T is temperature, p is the observed vapor pressure, and p_0 is the saturated vapor pressure of the liquid when there is no curvature. Within confined pore radius r_k, this relationship necessitates that condensation will occur at sub-p_0 pressure. In the case of contact angle, θ, at the liquid-pore wall interface between 0 and π, condensation occurs when $r_p = r_k\cos\theta$. Pore radius, r_p, can therefore be determined by observing the pressure at which early condensation occurs.

Since condensation typically occurs after an adsorbed layer has already formed on pore walls, it is necessary to also account for the thickness of this adsorbed film (Figure 1-6). Barrett,

Joyner, and Halenda (BJH)[31] proposed a modified Kelvin equation for the special case of cylindrical pore geometry,

$$r_p = r_k cos\theta + t_a \quad (1\text{-}5)$$

where t_a is the thickness of the adsorbed film. If the contact angle is assumed to be zero:

$$r_p = r_k + t_a \quad (1\text{-}6)$$

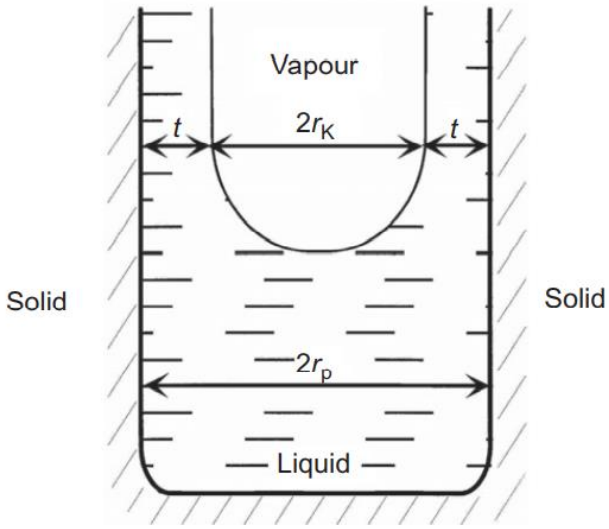

Figure 1-6. Relation between the Kelvin radius rk and the pore radius rp in a cylindrical mesopore. Adopted from Rouquerol et al. 1999[28]

Various methods have been developed to evaluate t_a as a function of relative pressure. The most common method, known as the "t-method," was proposed by de Boer.[32] In this method an adsorption amount as a function of relative pressure is first determined on certain well-defined nonporous solids, resulting in a "standard isotherm" or "t-curve" that is independent of the nature of the adsorbent. The adsorption amount is then converted to a thickness. For example, in the case of N_2,[31]

$$t_a[nm] = 0.1\sqrt{\frac{13.99}{0.034-0.4343ln\frac{p}{p_0}}} \quad (1\text{-}7)$$

It is worthwhile to mention that the standard t-curve is not satisfactory for measurement of t_a inside narrow mesopores with r_p < 10 nm,[33-35] as the film curvature and enhanced wall attractions are not properly considered in those instances. Similarly, the Kelvin equation cannot be applied accurately within the same size range to determine r_k. Several studies showed that the BJH method underestimated the size of narrow mesopores for these reasons.[21-22, 36] One solution is to treat narrow mesopores in the same way as micropores by applying the semi-empirical and molecular simulation-based methods mentioned in Section 1.4.1. These can be used to simulate the isotherms of both micropore and mesopore systems, including hysteresis.[22, 37] In reverse, useful information can thus be obtained from both the adsorption and desorption branches of an observed hysteresis loop by deconvolving it into component theoretical loops contributed by specific pore shapes and sizes. A commercial DFT software, developed and released by Micromeritics, is available for determining PSDs of different adsorbent-adsorbate systems and pore geometries (*e.g.*, cylindrical, slit, or hybrid).

1.4.3 Macropores

The conventional method for characterization of macroporous materials (up to 400 μm pore size) is Mercury Intrusion Porosimetry (MIP).[38] This method uses a pressurized chamber to force mercury into pores. Mercury fills the larger pores first, followed by smaller pores as pressure increases. However, mercury can cause several safety and environmental issues. Therefore, other

techniques can be used such as Electron microscopy (TEM or SEM), Computerized X-ray Tomography (CT), Magnetic Resonance Imaging (MRI), or liquid permeametry.[11]

1.5 Porous Gel Formation

A gel consists of a three-dimensional porous solid network where the pores are filled with another substance, usually a liquid. IUPAC defines a gel as a "Non-fluid colloidal network or polymer network that is expanded throughout its whole volume by a fluid".[39] Polymeric gels can have a distinctive set of properties, such as swelling and aging, that will be described in Sections 1.7 and 2.5. The solid network formation can be prepared through different routes that are described in this section. If the fluid is evacuated from the network by drying, a porous solid with cavities and channels will be produced. These pores may be regularly or irregularly arranged, and the physical properties of the resulting porous solid is influenced by the shape and size of the pores. These porous materials can be categorized according to the technique used to remove the pore fluid. The various drying techniques will be discussed in Section 1.7.

1.5.1 Sol-Gel Process

The sol-gel process is considered a conventional method to produce three-dimensional gel networks historically using silicate materials (Figure 1-7) as well as metal oxides.[40] Sol-gel mechanism typically includes nucleation, particle growth and ripening steps, which their gel particle size are controlled through different steps of well-manipulated chemical reactions and the kinetics of those reactions.[41-42] Metals are less electronegative than silicon. Therefore, they are more susceptible to nucleophilic attack.[43] The process starts with dissolution of molecular

precursors. They form a colloidal solution known as a sol. Afterward, sol particles react to form the gel network, either by aggregation under certain conditions or *via* chemical condensation reaction. Condensation reaction is a class of organic addition reactions that produce small molecule byproducts such as water, ammonia, ethanol, or acetic acid.

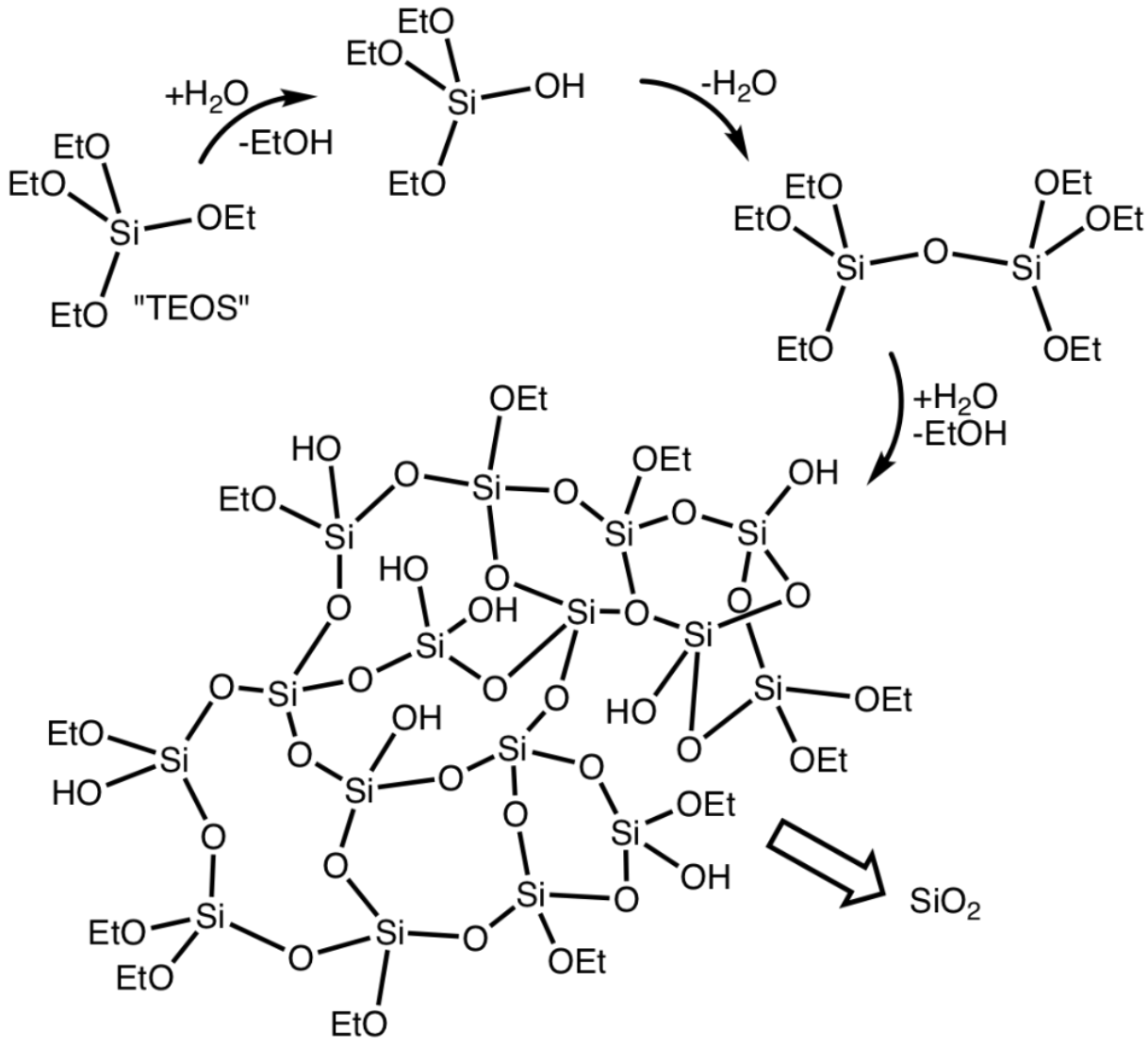

Figure 1-7. Hydrolysis of tetraethyl orthosilicate (TEOS) under acidic conditions and formation of SiO_2.[44]

The result of this process will be an irregular, three-dimensional, branched gel network.

1.5.2 Epoxide-Initiated Gelation

In epoxide-initiated gelation, the formation of metal oxides from metal salt precursors and water initiate a proton scavenger, usually an organic epoxide.[45] .Consequently, the pH increases, causing the formation of metal hydroxides and in the next step to the metal oxides like sol-gel route. This is useful to produce gels of many metal oxides, whose alkoxides may be hardly available.[45-46]

1.5.3 Gelation *via* Hydrosilylation Reaction

This reaction typically happens in the presence of an organometallic catalyst. The precursors are organic compounds with unsaturated bonds onto which Si-H bonds are added to form a three-dimensional network. Alkenes, alkynes, aldehydes, and ketones can be used as a precursor for this reaction.[47] This addition happens through a mechanism known as the Chalk-Harrod mechanism,[48] shown in Figure 1-8.

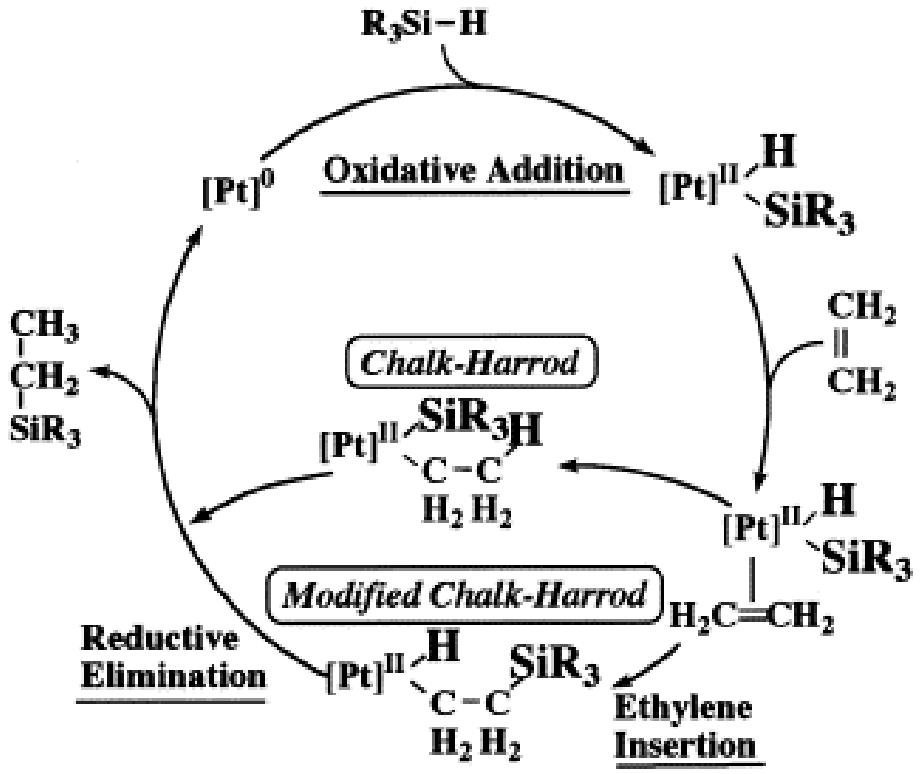

Figure 1-8. The Chalk-Harrod mechanism. [Pt] refers to an organoplatinum coordination complex. Adopted from Sakaki *et al.*1999.[48]

As a catalyst, organoplatinum has been used for hydrosilylation.[49] For example, Karstedt's catalyst, shown in Figure 1-9, has been well studied and is used widely in industry for hydrosilylation reactions.[47, 50]

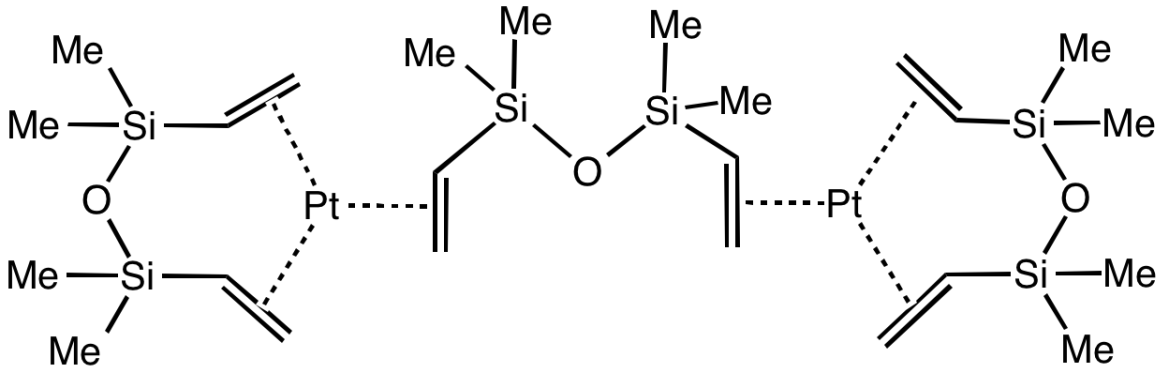

Figure 1-9. Karstedt's catalyst.[50]

1.6 Drying of Gels

Evaporation of the liquid phase from a wet gel by drying happens in two stages. In the first stage, as evaporation occurs, the gel deforms by shrinking, which squeezes additional liquid from the inside of the gel body to its surface, which is known as the syneresis process.[51] This stage of the drying process is critical to the final porosity of the dry gel. The shrinking is due to formation of a meniscus within the gel's pores, which creates high magnitude negative (relative to ambient) capillary pressure within the liquid phase, that in turn places compressive stress on the gel network. In the case of a cylindrical pore, capillary pressure, P_c, is described by the Young–Laplace equation,[6]

$$P_c = \frac{2\gamma cos\theta}{r_p} \tag{1-7}$$

P_c can be decomposed into a sum of radial and axial components P_r and P_a, shown graphically in Figure 1-10:

$$P_r = \gamma \sin\theta \tag{1-8}$$

$$P_a = \gamma \cos\theta \tag{1-9}$$

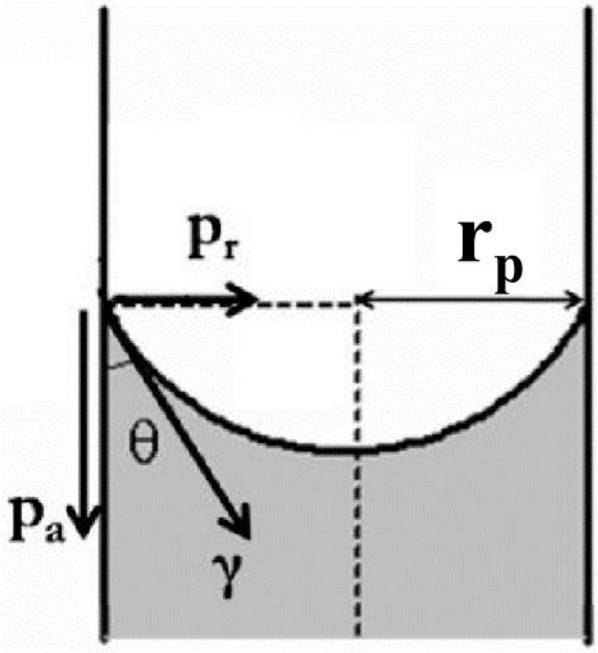

Figure 1-10. Radial and axial pressures acting on the cylindrical pore wall.

The second stage of evaporation starts when OH groups at the inner surface of the gel become close enough because of the initial shrinkage to react with each other. At this point, the network becomes increasingly stiffer, inhibiting further shrinkage and deformation of the gel.[52]

Most gels consist of a network of different sized pores filled with liquid. In larger pores, because they empty faster than smaller ones during evaporation, the meniscus of the liquid recedes faster because the vapor pressure in the liquid phase with the pore with the larger meniscus is higher. Therefore, walls between pores of different size, such as in Figure 1-11, are subject to uneven stress, which causes cracks in the dried gel.

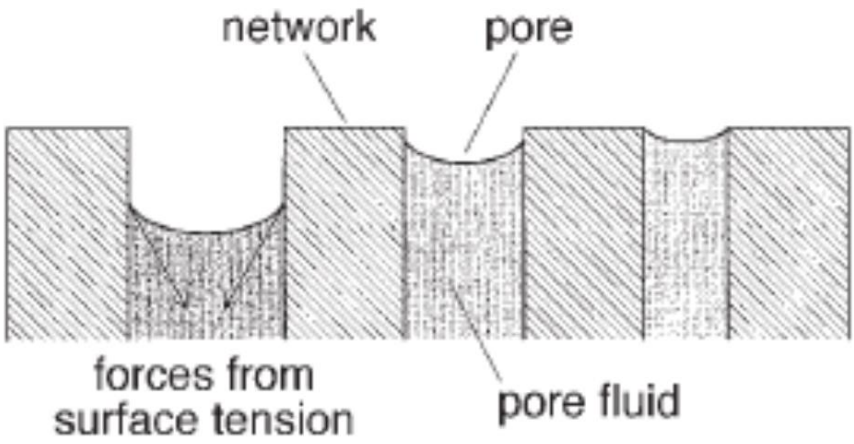

Figure 1-11. At the same pressure, the curvature of all menisci in the pores is the same. The larger pores empty first, which creates an uneven stress in pores of different size during drying. Adopted from Hüsing and Schubert 1998.[53]

1.7 Different Types of Gels

Methods have been studied to conserve the pore structure of gels to avoid or minimize pore shrinkage. Dry gels can be categorized based on the method by which they are dried, some of which are introduced in this section.

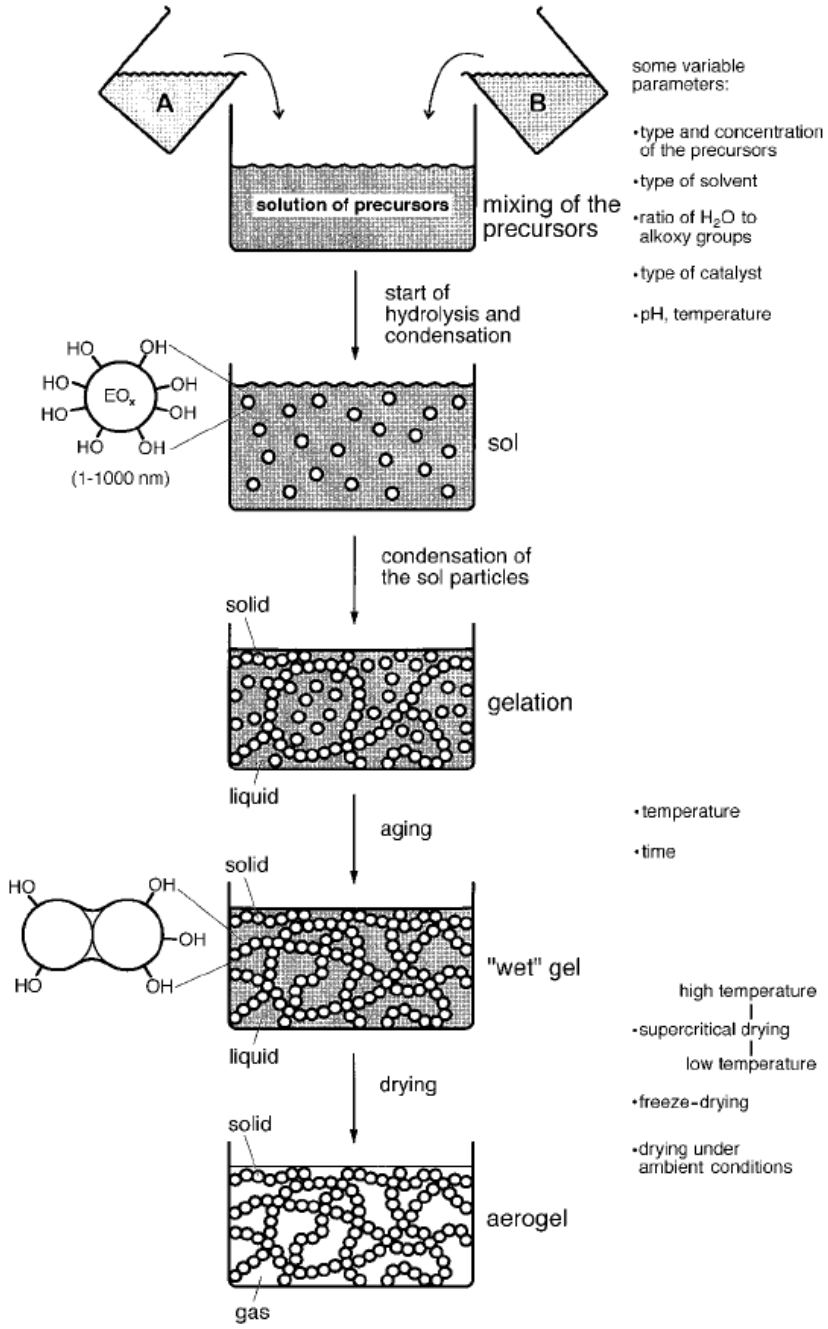

Figure 1-12. General scheme for gel formation by sol-gel process and some typical variable parameters as well as drying techniques, which produce different types dried gels. Adopted from Hüsing and Schubert 1998.[53]

1.7.1 Xerogels

A xerogel is formed by pure evaporative drying of a wet gel. The capillary forces lead to large shrinkage as well as near destruction of the initially uniform gel body.[45 54]

1.7.2 Aerogels

Aerogels are lightweight, highly porous solids. They were first invented by S. S. Kistler in 1932, who defined them as "gels in which liquid has been replaced by air, with
very moderate shrinkage of the solid network."[55] Since then, the term aerogel has been defined in the literature in different ways. IUPAC defines aerogel as "gels comprised of a microporous solid in which the dispersed phase is a gas."[39] However, there are some examples of microporous materials like zeolites that are not aerogels. Hüsing and Schubert also described aerogels broadly as "materials in which the typical structure of the pores and the network is largely maintained (which is not always the case for supercritical drying) while the pore liquid of a gel is replaced by air."[53] Leventis defined the term "aerogel" more precisely as "an open non-fluid colloidal network or polymer network that is expanded throughout its whole volume by a gas, and is formed by the removal of all swelling agents from a gel without substantial volume reduction or network compaction."[56]

From all definitions mentioned above one can conclude that aerogels are derived from wet gels where the pore-filling solvent is removed in a way that preserves the porous skeletal framework of the wet-gel with minimum volume shrinkage.

1.7.2.1 Supercritical Drying

To remove the pore liquid without developing a meniscus inside the pores that applies stress to the pore walls (when the contact angle is not zero), the liquid can be brought to a supercritical state where there are no gas-liquid interfaces in the pores during drying. To reach the pressure and temperature required to achieve a supercritical state, the wet gel is placed in an autoclave and either covered with the same solvent that composes the gel or washed with a different solvent. After the autoclave is closed, the temperature is slowly increased until the critical point of the solvent is surpassed. The supercritical state is held for a period of time to ensure all pore fluid equilibrates. The fluid is then purged, while still above the critical temperature, until ambient pressure is reached. Finally, the autoclave is cooled to room temperature while still open, replacing the fluid that occupied the pores of the gel with air. Supercritical drying has two variations depending on the supercritical fluid that is used.

1.7.2.1.1 Drying in Organic Solvents

When the solvent used for drying is the same as that used for making the wet gel, the method is also known as “Hot” drying.[53] Generally, the solvents used for making wet gels can be brought to supercritical condition. Table 1-1 shows the critical constants for some conventional solvents.

Solvent	Tc (K)	Pc (bar)
Acetone	508.15	47
Ethanol	516.15	63
Methanol	513.15	79
2-Propanol	508.15	47

Water	647.15	221

Table 1-1. The critical constants for some conventional solvents.

However, since solvents are typically flammable or toxic, they can be especially dangerous at supercritical condition. Supercritical water is highly reactive and can dissolve some metal oxides. There is also the risk of rearrangement within the gel network at high temperatures. It is typical used for drying hydrogels as water is not flammable or toxic.

1.7.2.1.2 Drying in Carbon Dioxide Solvent

In contrast with hot drying, the other supercritical drying method is known as "Cold" drying, which is frequently used to overcome the drawbacks associated with hot drying.[53]

Solvent	Tc (K)	Pc (bar)
Carbon dioxide	304.15	73

Table 1-2. The critical constants for carbon dioxide.

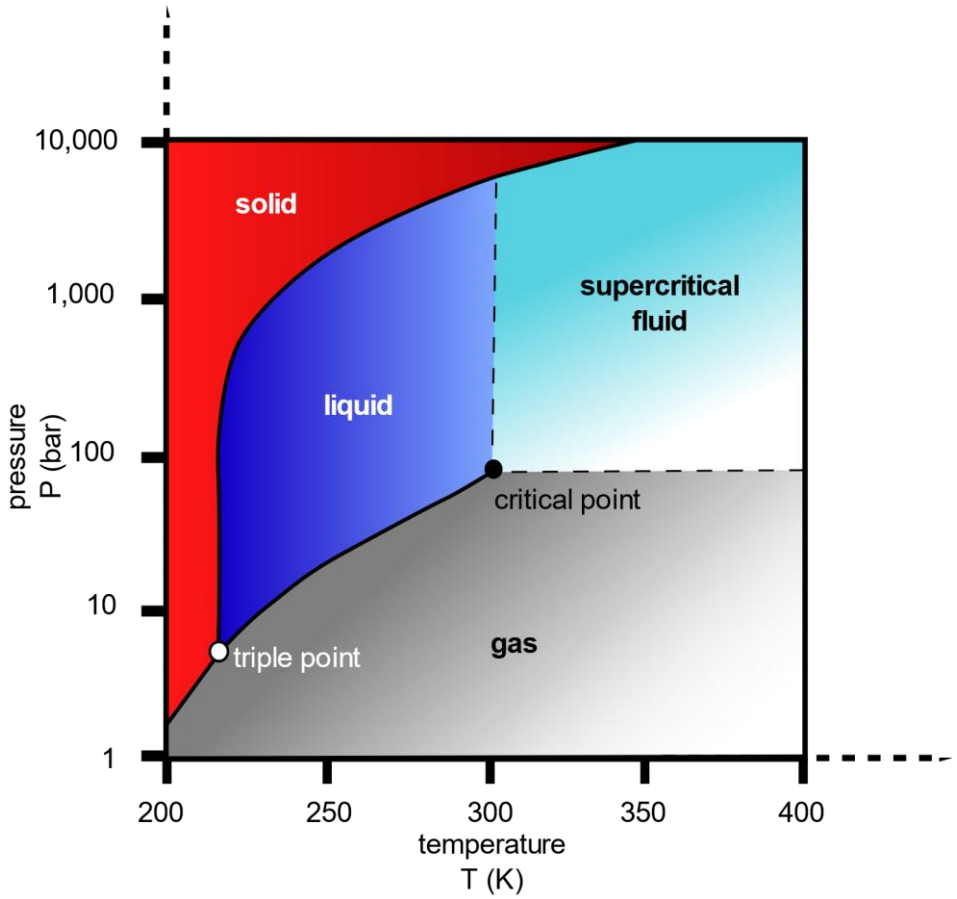

Figure 1-13. The Temperature-Pressure phase diagram of CO_2.[57]

As shown in Table 1-2 and Figure 1-13, CO_2 has more moderate critical constants compared to organic solvents or water. To utilize this property for drying, the gel liquid is first exchanged with several washes of liquid CO_2 after inserting the sample into an autoclave. Once CO_2 has fully replaced the pore liquid, temperature and pressure of the autoclave are adjusted to values above the critical conditions. Finally, CO_2 is removed while in a supercritical phase by controlled pressure release.

This method also has some limitations. For example, some solvents are not miscible with liquid CO_2, the most prominent example being water. To solve this problem, an intermediate liquid

exchange step can be introduced first using a liquid solvent that is miscible with both the starting solvent and with CO_2. Another disadvantage of cold drying is that it is more time consuming. Diffusion of carbon dioxide into the gel controls the time required for exchanging the original pore liquid, which in turn depends on the dimensions of the gel body.

1.7.3 Ambient Dry Gels (Ambigels)

Supercritical drying is costly and requires equipment such as an autoclave. It can be also a dangerous procedure. Therefore, supercritical drying is not an appealing technique for industrial scale processing, and ways to dry aerogels at ambient conditions have been investigated. Gels that are dried in ambient conditions are known as ambigels.

The overall strategy behind ambient drying methods is to modify the gel system to create some combination of minimizing shrinkage in the first place and making shrinkage reversible. As described in Section 1.6, shrinkage is caused by capillary pressure, which is proportional to surface tension γ. Manipulating γ by solvent exchange or chemically modifying the gel surface can therefore reduce the compressive stress that acts on the gel during drying and again manipulating contact angle. In addition, shrinkage is generally irreversible on account of surface OH groups that attract each other once the gel walls have contracted. By replacing surface OH groups with alternative chemical terminations, some reversibility of shrinkage can be attained by a phenomenon that is referred to as the "spring-back effect." [52, 54] As an example, Smith *et al.*[52] and Prakash *et al*.[54] prepared silicon-based ambigels *via* solvent exchange and surface modification. For solvent exchange, water was substituted with a mixture of isopropyl alcohol and n-hexane.

The hydroxylated surface (Si-OH) of the inorganic gel was derivatized with organosilanes, for example trimethylchlorosilane, through standard silylation routes to Si-O-SiR_3. Because organosilyl-terminated surfaces do not participate in condensation reactions or hydrogen bonding, the shrinkage that occurred during drying was rendered reversible, and the gel subsequently expanded back to almost its original size as proven by environmental scanning electron microscopy (ESEM) snapshots.[54] Besides solvent exchange, reduction of surface tension at the liquid-pore wall interface can also be accomplished with drying control chemical additives (DCCAs). For example, formamide (NH_2CHO) and glycerol ($C_3H_8O_3$) have been reported to be used to generate a wide range of sizes and shapes of dried gel monoliths of SiO_2, Li_2O-SiO_2, Na_2O-SiO_2, and Na_2-B_2O_3-SiO_2.[58-59] Different routes to generate xerogel, ambigel and aerogel are illustrated in Figure 1-14.

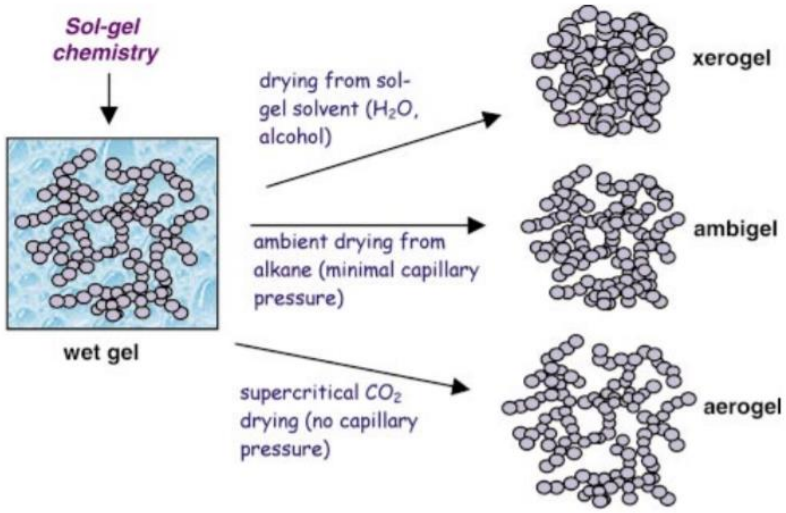

Figure 1-14. Different ways to produce xerogel, ambigel and aerogel. Adopted from Rolison *et al.* 2001.[60]

1.7.4 Freeze Dry Gels (Cryogels)

Another way to avoid meniscus formation during drying is to adjust the temperature and pressure of the system to instead create a rigid solid-gas interface. In other words, the pore liquid can be solidified and then sublimed, instead of evaporated, from the pores.[40, 61-62] This can require an extended aging period to stabilize the gel network, exchange of the gel solvent for another with a low expansion coefficient and a high sublimation pressure, or addition of salts to reach lower freezing temperatures.[53]

1.8 Polymer Derived Ceramics (PDCs)

The transformation of polymer to ceramic was a revolution in ceramic science and technology. The production of ceramics from polymeric precursors was first reported in 1960s by Ainger and Herbert,[63] as well as Chantrell and Popper.[64] After a decade, Verbeek reported the first practical transformation of organosilicon polymer into ceramic fibers composed of a homogeneous mixture of silicon carbide and silicon nitride.[65] Yajima[66] as well as Fritz[67] published a procedure for synthesizing a polycarbosilane that could be melt-spun to produce SiC fibers after pyrolysis. The chemical composition of these ceramics is derived from inorganic and organic components of the polymeric precursor.

Using PDCs for manufacturing ceramics provides different advantages. For one, the object can be processed and shaped at low temperature. Conventional polymer forming techniques also can be applied such as extrusion, injection molding, coating from solvent, Polymer Infiltration

Pyrolysis (PIP), or resin transfer molding.[68] Once formed, they can then be converted to ceramic components by addition of heat. Another advantage is that the PDC approach is free of burdens such as the need for sintering additives and technical application limitations associated with traditional ceramic manufacturing.[68] Moreover, PDCs' thermo-mechanical properties with respect to creep, oxidation, crystallization, and phase separation are in general enhanced compared to traditionally-made ceramics.[68] They can also have ternary compositions (*i.e.*, containing three elements) that cannot be easily obtained with other processing methods. For example, C or N cannot be dissolved into binary Si_3N_4 or SiC compositions to form ternary SiCN compositions, and C or O cannot be dissolved into binary SiO_2 or SiC to form SiCO ceramics. SiCN and SiCO compositions can only be synthesized using PDC routes.

PDCs are polyorganosilicon compounds. A simplified formula of an organosilicon polymer that can be used as a precursor for the synthesis of ceramics is shown in Figure 1-15, where -Si-X- makes up the polymer backbone, and R^1 and R^2 are organic functional groups . Si-based polymers are classified according to the identity of X. Chemical and thermal stability, solubility, and electronic, rheological, and optical properties of each class of polymer depend on R^1 and R^2, and by changing them suitable properties can be achieved.

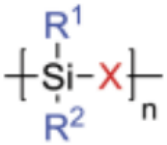

Figure 1-15. The simplified formula of an organosilicon polymer. X= Si is polyorganosilanes, X = CH_2 is polyorganocarbosilanes, X = O is polyorganosiloxanes, X = NH is polyorganosilazanes, and X = [N=C=N] is polyorganosilylcarbodiimides. Adopted from Colombo 2010.[68]

The general classes of organosilicon polymers used as precursors for making PDCs include polycarbosilanes, polycarbosiloxanes, polysiloxanes, polysilazanes, polysilylcarbodiimides, polyborosiloxanes, polyborosilanes, polyborosilazanes, polysilsesquiazanes, and polysilsesquicarbodiimides. Figure 1-16 diagrams the typical classes of organosilicon polymers used as precursors for ceramics. Silicon carbide (SiC), silicon oxycarbide (SiCO), and silicon carbonitride (SiCN) are some of the ceramics that can result from annealing of organosilicon polymers at high temperature.[68-69]

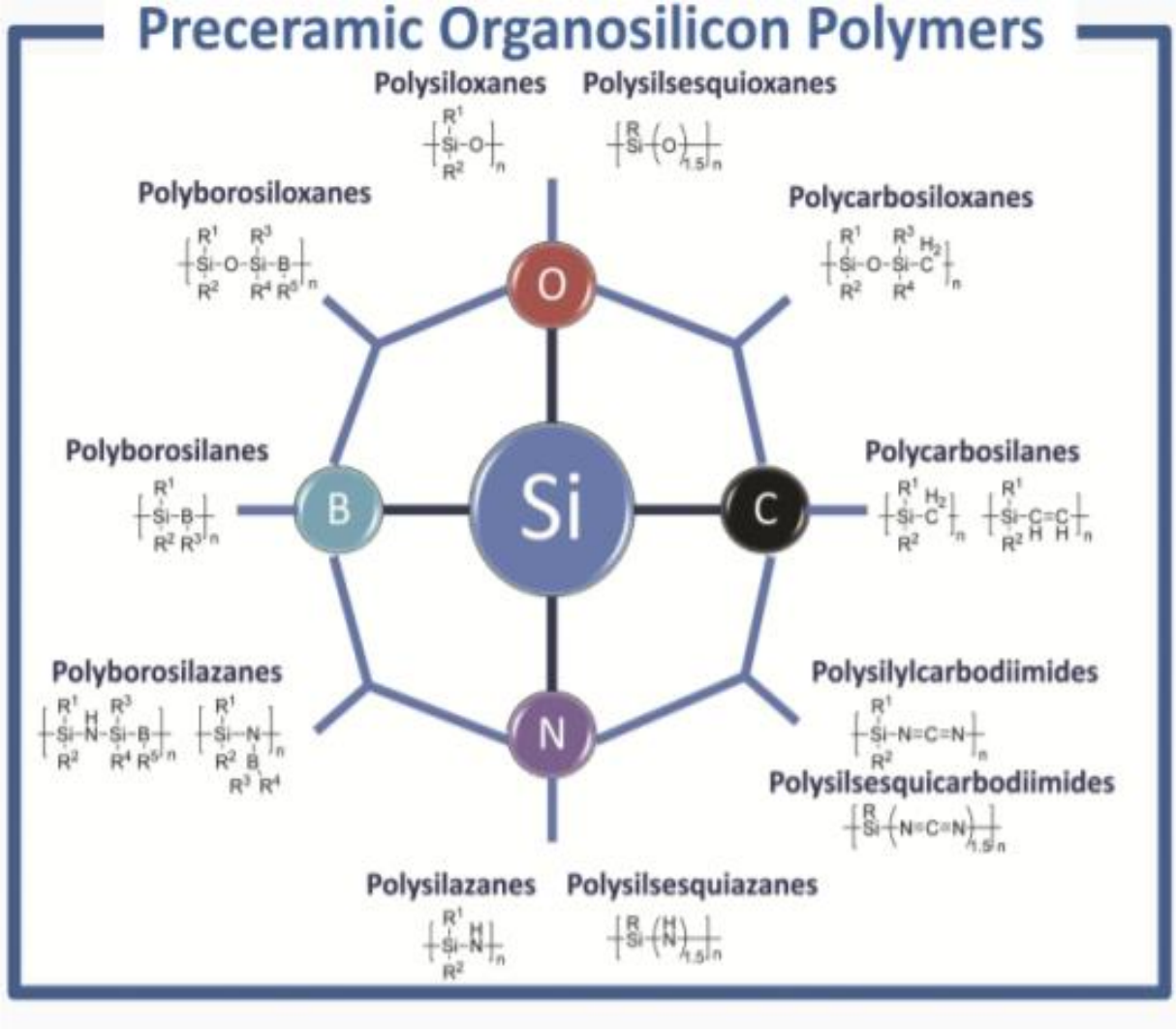

Figure 1-16. General classification of organosilicon polymers. Adopted from Colombo 2010.[68]

Transformation of a silicon-based polymer to a ceramic happens through controlled thermal decomposition. The resulting nano-structured ceramics are influenced not only by the chemistry and architecture of the precursor polymer but also by the processing route and annealing parameters such as heating rate, reactivity of the annealing atmosphere, and dwell time. Transformation of polymer precursors as a function of temperature is show in Figure 1-17.

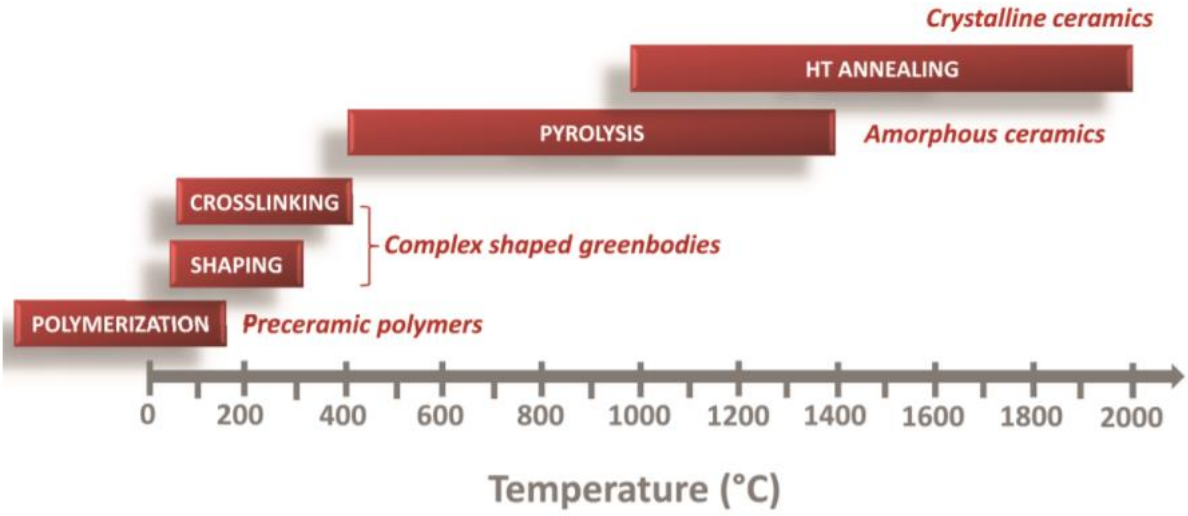

Figure 1-17. Polymer-to-ceramic transformation. Adopted from Ionescu and Riedel 2012.[69]

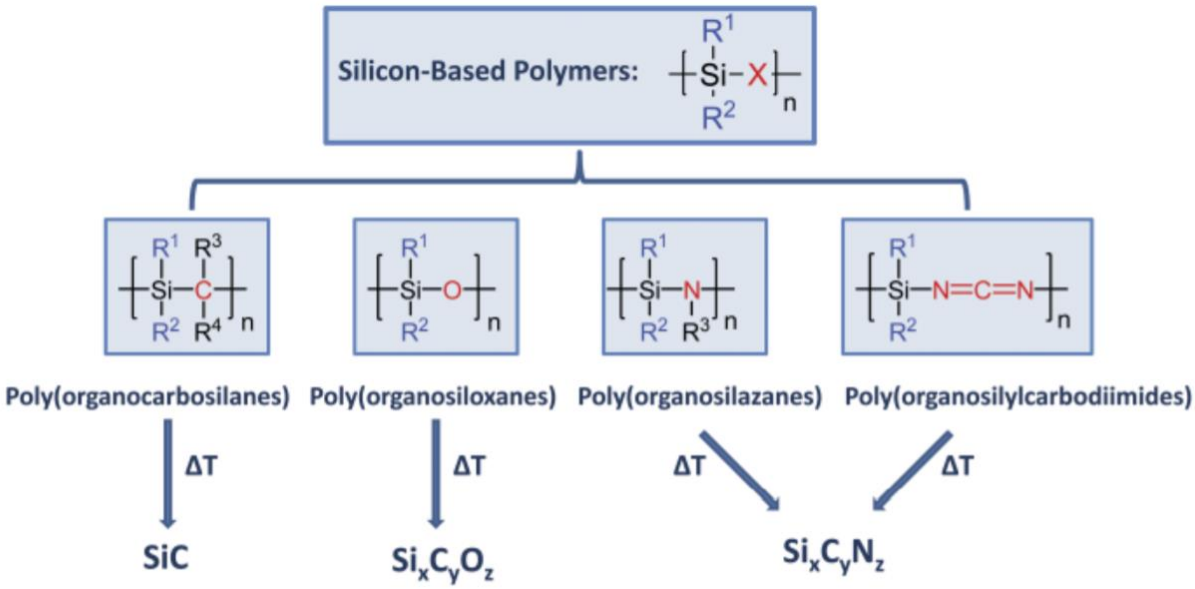

Figure 1-18. Polymer-to-Ceramic Conversion. Adopted from Colombo 2010.[68]

1.9 Porous Polymer Derived Ceramics

Porous ceramics have played important roles in various engineering applications. Highly porous ceramics can be manufactured in different shapes such as foams, honeycombs, fibers mats, *etc.* There are numerous applications in various fields, including as filters, catalyst supports, supports for space mirrors, biomedical devices, kiln furniture, reinforcement for metal matrix composites, bioreactors, thermal protection systems, components in solid oxide fuel cells, lightweight sandwich structures, and heat exchangers.[70] Hence, production of highly porous ceramic components that can be used in a wide range of applications requires well-controlled and diverse processing strategies. Suitability for such applications is driven by the chemical composition of the porous scaffold materials and their porosity characteristics, such as specific surface area (SSA),

pore size distribution (PSD), and interconnectivity. Figure 1-19 shows different types of porous structure of PDCs.

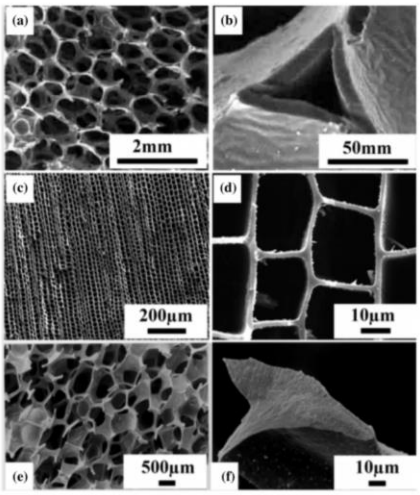

Figure 1-19. Scanning Electron Microscope (SEM) micrographs of: (a,b) a porous SiBOC foam annealed at 1400 °C, (c,d) porous SiC/C annealed at 1500 °C, (e) the open-cell structure and (f) the structure of a SiCSi3N4 foam produced from PS/Si3N4 (80/20 wt%) after pyrolysis at 900 °C. Adopted from Vakifahmetoglu *et al.* 2016.[71]

1.9.1 Processing Routes

Processing of PDCs offers unique advantages. Conventional plastic forming techniques such as injection molding, extrusion, resin transfer molding, melt spinning, *etc.*, can be applied, generally at low cost, to pre-ceramic polymers.[68, 72] Imparting porosity to the polymer prior to annealing can be accomplished by many different processes, including sacrificial templating, blowing, etching, freeze casting, emulsion formation, spinning, and gel formation coupled with different drying techniques (yielding xerogels, aerogels, ambigels, or cryogels).[71]

1.9.2 Applications

Porous ceramics have high specific surface area, low density, low thermal conductivity, low dielectric constant, high permeability, and good resistance to chemical attack.[68] This combination of excellent physical and chemical properties makes them critical for many applications. Historically, they have been used on the U.S Space Shuttle for providing thermal protection by producing composites obtained from SiCO and Nicalon.[73] Porous ceramic filters that remove particles at high temperature and pressure have efficiencies higher than scrubbers, cyclones, or electrostatic precipitators in terms of particle sizes removed per unit particle.[74] They can be used for recovery of CH_4 from mines, removal of CO_2 and H_2S from natural gas, and recovery of H_2 in petroleum refining. Since they have outstanding resistance to chemical attack at high temperatures, porous ceramics have been employed as filters for different molten metals including super alloys such as cast aluminum, iron, steel, and some nonferrous metals.[74-76] They also can be employed as support materials for advanced catalysts operating at high temperature and under harsh mechanical and chemical conditions.[68, 77] In the biomedical field, unique characteristics of porous ceramics have led to their use as implant support materials. In that instance, the material surface characteristics such as porosity have a direct influence on growth and proliferation of cells on the support materials.[71] Highly porous silicon oxycarbide glasses are potential candidates for use as drug delivery carriers. A study by Tamayo *et al*. shows that it is possible to adjust the adsorption and release properties of the silicon oxycarbide by surface modification.[78] Metallic ions such as Ca^{2+}, Mg^{2+}, and Ag^{+} can be incorporated into the PDCs' network structure, which impart antibacterial properties and bioactive behavior.[79] Finally, porous ceramics are used as anode material in lithium ion batteries.[80]

1.9.3 Thesis Objectives and Overview

The overall objective of this thesis is to investigate the porosity of materials, their connectivity types in a porous network, and correlating the materials' different pore characteristics to the effects of synthesis conditions and precursor role on the microstructure and the composition of the materials. This is achieved through various studies:

i) The effect of solubility and swelling of the SiCO wet gels synthesized in different solvents and processed in different solvents and different mixtures was studied. The basic principle "like-dissolve-like" was first applied to investigate the solubility parameters of the polymeric precursor used for preparing the aerogels. Subsequently, the solubility rules were applied to predict swelling degree of wet gels in different solvents and their mixtures.

ii) A quantitative analysis on the geometry and hierarchical structure of the SiCO aerogels was investigated to achieve an insight on the role of the synthesis solvent on the pore architecture. The relation between the mesopore structure and hysteresis behavior was examined. These measurements were coupled with an advanced modeling framework based on nonlocal Density Function Theory (non-local DFT). [25]

iii) A novel crosslinking agent for forming the aerogel network was introduced and its effects on the aerogel's microstructure and functionality were studied.

CHAPTER II: EFFECT OF SOLVENT ON POROSITY

This chapter starts with an introduction to silicon oxycarbide ceramic, particularly in the aerogel form, which is the porous material of the study. Subsequently, the experimental methods to produce porous silicon oxycarbide pre-ceramic and ceramic aerogels are described. Some details about the required the reagents and equipment to obtain these aerogels, the reagents as well as the study's characterization techniques are explained. Finally, the of solubility/swelling of polymeric SiCO wet gels in different solvents and solvents' mixtures are discussed.

2.1 Silicon Oxycarbide

Among organosilicon polymers that mentioned in the Section 1-8, a significant research amount has been devoted to studying poly(organosiloxanes) which produce silicon oxycarbide (SiCO) ceramic after the heat treatment (Figure 1-15).This type of ceramic is stable at high temperatures, tolerant of oxidative and corrosive environments, and can have different properties like electrical conductivity and piezoresistivity.[68, 81-83]

SiCO can be obtained by annealing either polysiloxanes, polysilsesquioxanes, or polycarbosiloxanes.[68] The annealing procedure consists of different stages of mass loss, depending on the chemical composition and side groups within the polymer. Typically, up to 400 °C, no significant decomposition occurs. Most of the mass loss happens in the temperature range of 400 °C - 800 °C, due to the release of cyclic siloxane species as well as hydrocarbons like methane, ethane, ethylene, and styrene.[84-85] As gaseous species leave the material, they can create significant porosity inside the material so long as there is not simultaneous collapse. Above 800 °C, the only mass loss is from residual hydrogen and free radical reactions and viscous flow start to destroy pore surfaces that they were created at the previous stage.[84-86] Approximately at the temperature range of 800 °C – 1100 °C the material consists of an amorphous SiCO matrix. In this matrix Si is tetrahedrally bonded to either O or C forming SiO_xC_{4-x} bonds, plus a carbon phase that is called free carbon.[87-88] The elemental composition of the SiCO can be written as $Si_xO_yC_z$, which can be plotted on a ternary elemental diagram (Figure 2-1).[89-90] The elemental diagram can be also used for an estimation the possible phases of SiCO.[91] The composition of SiCO has no free carbon on the line between SiO_2 and SiC, then the resulting SiCO material and it is composed of amorphous SiCO phase (the purple volume).[92] Therefore, composition of SiCO has a portion of

free carbon in the space among the tie lines, which is favored for technologically significant SiCO ceramics.

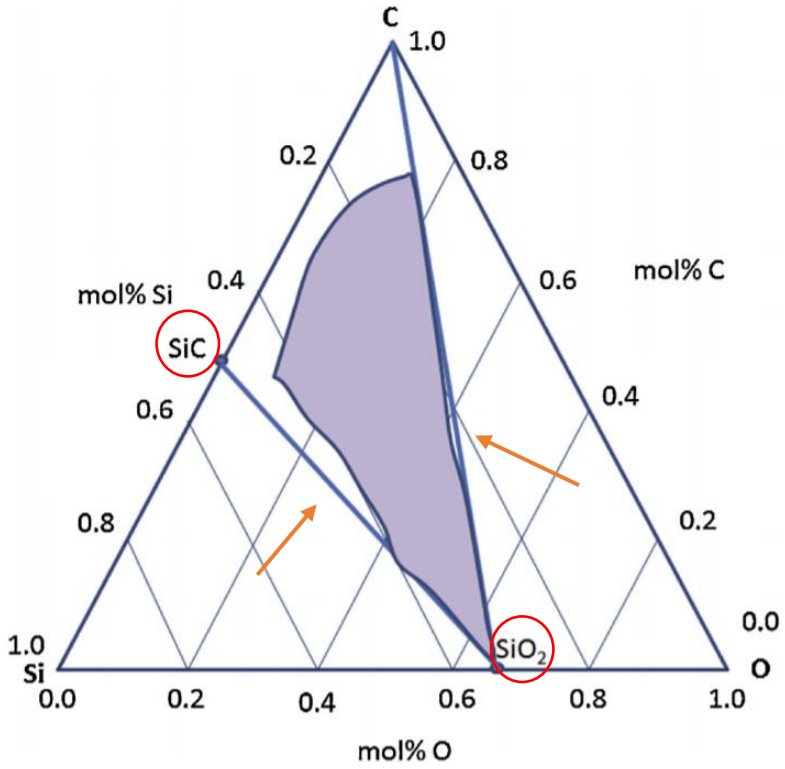

Figure 2-1. SiCO elemental diagram. The binary stable thermodynamic phases (SiO_2 and SiC) at high temperatures are indicated by red circles. The composition of the stoichiometric SiCO glasses ($SiC_xO_{2(1-x)}$) are on the SiC–SiO_2 line indicated by orange arrows. The purple volume indicates compositions of SiCO glasses that are well-studied and reported in the literature. Adopted from Lu 2015.[90]

Different models of SiCO system and attempts to simulate the pyrolysis of preceramic polymer into SiCO have been studied. At the inception of this study Kroll modelled a low-density porous structure of α-SiCO embedding a triple-chain of carbon atoms taken from a graphite sheet structure to study the "free carbon" phase in silicon oxycarbide glasses.[93] However, hydrogen was not involved in the model and it has been known that hydrogen is present since experimentally it

continues to be released at high pyrolysis temperatures (>1200 °C). Recently, Ponomarev, van Duin, and Kroll modelled the conversion of polymethylhydrosiloxane (PMHS) crosslinked with divinylbenzene (DVB) to SiCO by heat treatment process.[94] They observed formation of graphene segregations embedded in an amorphous oxycarbide matrix.

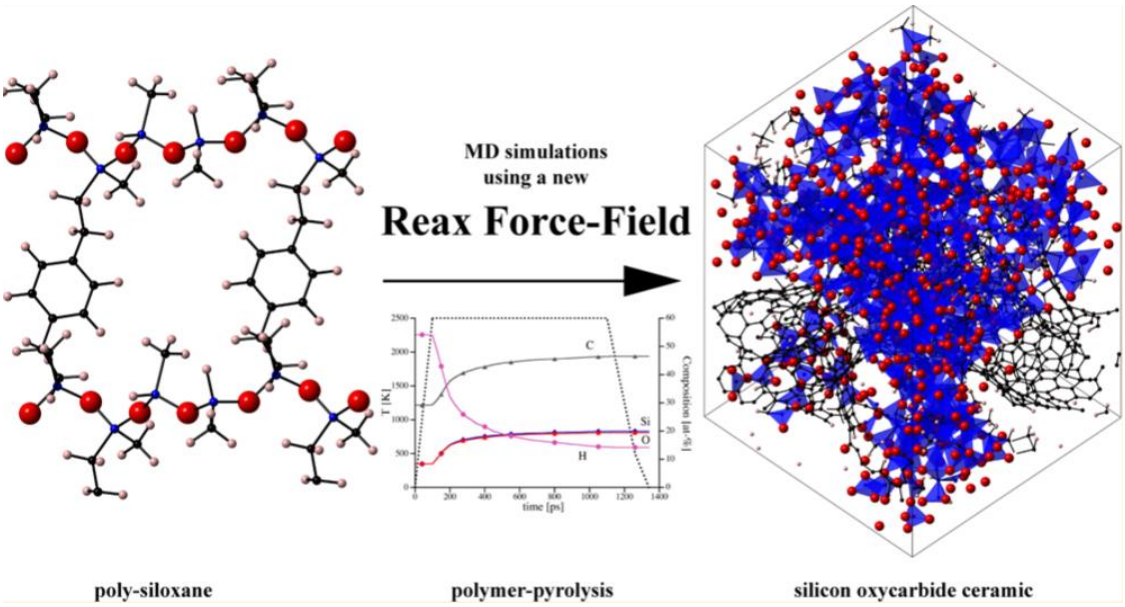

Figure 2-2. Pyrolysis of polysiloxanes into SiCO ceramics using Reactive Force Field simulation. Reproduced from Ponomarev *et al.*[94]

2.1.1 Porous Silicon Oxycarbide

Porous SiCO has unique properties, such as being stable at high temperature and resistant to oxidation in harsh environments, , that they make it a promising material in several applications. Some of these applications are anodes in lithium ion batteries, thermal barriers, filtration, and catalyst supports.[72, 90] There are different routes to introduce porosity into SiCO systems. It can be introduced into a system during the fabrication process, network formation on crosslinking with a polymeric precursor, and during or after pyrolysis. This diversity of choices results in a high

degree of control of the size (micro, meso, or macropore) and distribution of pores. Different morphologies of SiCO have been successfully fabricated, such as aerogels,[95-96] foams,[72, 97] or fibers[98-99] based on the demands of different fields. Techniques, such as freeze casting, foaming, and sacrificial templating can be used during crosslinking of the preceramic polymer or during annealing and after phase separation decomposition of one polymer in a polymer, can be used to create porosity ranging from micropores to macropores.[72, 86, 90, 100-103] Selectively etching the material using hydrofluoric acid (HF) after annealing also can be applied, which remains some of SiCO, SiC, and carbon phases.[104-105] The etching method can produce pore sizes ranging between micropores and mesopores, and is dependent on several processing parameters such as annealing temperature and the SiCO composition.[106-108]

2.2 Fabrication

Fabrication of polymer derived SiCO ceramics involves three steps. The first step is the crosslinking of the polymer precursor. Next step is the polymer-to-ceramic conversion. Finally, the last step is the phase formation that occurs at high temperature.

2.2.1 Shaping and Crosslinking

The polymer precursors can be either liquid or solid. The liquid polymers must be able to crosslink (*i.e.,* they have functional groups that can form a network or they can react with an external crosslinking agent). The solids must be able to melt and be cured. If they cannot melt, they should be soluble in a solvent. The liquid precursors can be fabricated into the desired via conventional plastic forming technologies, such as casting, drawing, injection molding, and infiltration.[68]

Historically, SiCO is synthesized through sol-gel processing that was described in the Section 1.5.1 via hydrolysis and condensation of molecular precursors such as tetraethyl orthosilicate.[87, 92, 109] Another recently developed route is through the hydrosilylation reaction, which was discussed in the Section 1.5.3. The key factors of pore formation at the network formation stage are the degree of dilution, polymer interactions with the solvent, choice of the crosslinking agent (in case that the precursor polymer does not have the functional groups to form the network), and degree of crosslinking, which can depend on time and the temperature of the reaction. In this thesis the effect of polymer interactions with the solvent as well as the choice of the crosslinking agent on pore formation and the pore structure will be discussed in Section 2.5 and Chapter III.

2.2.2 Polymer-to-Ceramic Conversion

Pores in micro and meso sizes are formed during the SiCO precursor transformation from the polymeric to the ceramic phase due to the evaporation of low molecular weight molecules and oligomers.[90] .These pores present in the porous structure up to 600 °C.[90] However, these pores are dramatically reduced their sizes or they completely collapse during the annealing procedure at higher temperatures. The porosity elimination at higher temperature than 600 °C causes a significant shrinkage and densifies SiCO systems regardless of its precursors' composition.[86]

2.2.3 Phase Formation at Higher Temperature

Starting around 1400 °C, carbothermal reduction reaction happens between SiCO and free carbon mixture, which converts the mixture to a SiC ceramic. Therefore, porous SiC can be generated. By

adjusting the annealing temperature at this stage the porosity of the porous SiC ceramics can be controlled within a range of 32–64%. [90]

2.3 Fabrication Equipment Supplies

Fabrication equipment supplies can vary depending on the application of the final porous SiCO material and the pore architecture that is targeted. Among mentioned morphologies of SiCO ceramics in the Section 2.1.1, the SiCO aerogel is the focus of this study. Therefore, here we discussed those supplies that we applied in this thesis work.

2.3.1 Parr Digestion Vessel

Most gel formation reactions that have been studies in this thesis require temperatures that increases the crosslinking rate of the polymer network formation but simultaneously they are above the 1-atmosphere boiling temperature of the synthesis solvents. To solve the evaporation problem digestion vessels are applied to keep the solvent liquid during the crosslinking and formation of the gel. The digestion vessel must tolerate the pressure inside and the reaction temperature as well as being non-reactive with any of the chemicals used. Parr digestion vessels (Parr Instrument Company) are chosen to be used in this thesis. They have chrome plated bronze jacket to provide the mechanical strength required for closing the system. Additionally, they have an inner chemically inert PTFE (polytetrafluoroethylene) liner and a sealing cap provided with a spring, which can release any unpredicted high pressure build up. The model that has been used for all gel formation of this work was a Parr Digestion Vessel 4749, with an inner cup capacity of 23 mL, a

maximum temperature allowed of 250 °C and a maximum pressure of 125 bar, which is shown in the Figure 2-3.

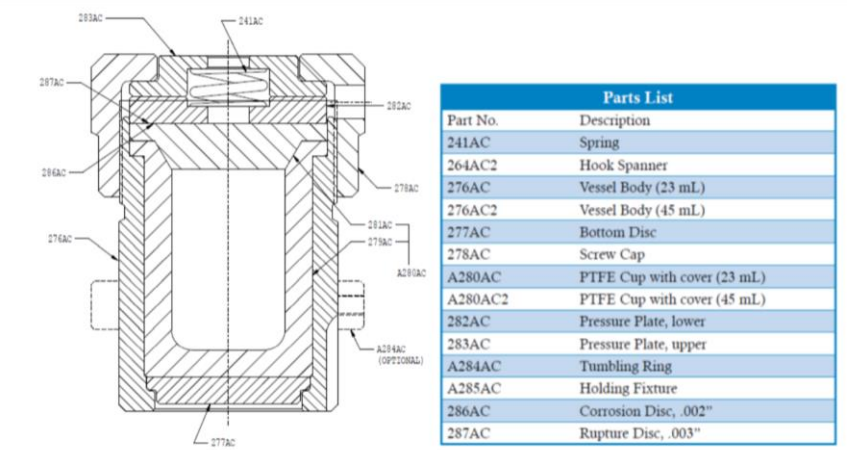

Parts List	
Part No.	Description
241AC	Spring
264AC2	Hook Spanner
276AC	Vessel Body (23 mL)
276AC2	Vessel Body (45 mL)
277AC	Bottom Disc
278AC	Screw Cap
A280AC	PTFE Cup with cover (23 mL)
A280AC2	PTFE Cup with cover (45 mL)
282AC	Pressure Plate, lower
283AC	Pressure Plate, upper
A284AC	Tumbling Ring
A285AC	Holding Fixture
286AC	Corrosion Disc, .002"
287AC	Rupture Disc, .003"

Figure 2-3. Different parts of Parr digestion vessels made by Parr Instrument Company (top), chrome plated bronze jacket and PTFE digestion vessel with a sealing cap (bottom).

2.3.2 Autoclave

As it was mentioned in the Section 1.7.2.1 an autoclave is needed to remove residual solvent contained in the pores and the solvent must be substituted with liquid CO_2 through multiple washing before bringing the CO_2 above its critical point and remove it as a supercritical fluid. The autoclave should withstand the high pressure (100 -120 bar) and its temperature can be precisely controlled. Therefore, a custom autoclave was built by the University of Texas Arlington Physics' workshop using the schematics,[110] ideas and solutions from professor G.D.Sorarù,[111] in University of Trento in Italy. The autoclave, shown in Figure 2-4, has two glass windows, which enable looking inside the chamber for liquid level evaluations as well as monitoring samples behavior during all the liquid exchange steps and drying. The autoclave is designed in the way that its temperature can be adjusted by a device connecting it to a thermostatic water bath (purchased from NESLAB). So, the temperature of the autoclave chamber can be adjusted to be as low as 1 or 2 °C for filling it with liquid CO_2 and as high as 45 or 50 °C to bring the whole system above the critical temperature of CO_2. It is worthy to mention that the autoclave has no pump connected to the system and, in absence of other external factors, the equilibrium pressure would be quickly reached on both the branches of the system. So, by adjusting the temperature of the autoclave below room temperature a stable pressure difference between the CO_2 source (which is at room temperature) and the autoclave can be created, deriving the flow of liquid CO_2 from the tank to the chamber in each exchange step.

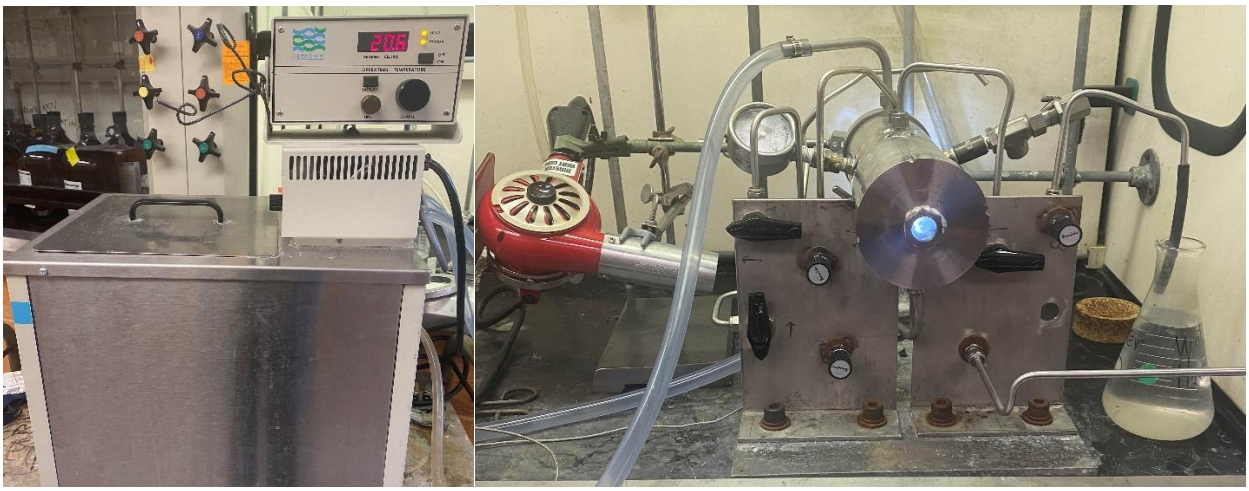

Figure 2-4. The thermostatic water bath (left), the autoclave (right).

2.3.3 Furnace

A thermal treatment in an inert environment such as N_2 or Ar, in air, or any other environments such as H_2 can be done in a high temperature furnace. Tubular furnaces are designed to control the atmosphere inside the tube, so often they are used for this kind of treatments. Within this work thesis a tubular furnace (purchased from ATS Applied Test System, 3110 series) with maximum temperature of 1200 °C equipped with a quartz tube with 50 mm outer diameter, 44 mm inner diameter, and 1000 mm length (MTI Corporation), a water cooled sealing flange for 50 mm diameter tube(MTI Corporation), polyurethane tube (12 mm x 8 mm) for water chiller (MTI Corporation), and high temperature silicone rubbers O-ring 50 mm diameter (MTI Corporation) was applied as it is shown in Figure 2-5.

Figure 2-5. Th tubular furnace (top) and its temperature control system (bottom).

2.4 Chemical Reagents

Chemical reagents also can vary depending on the application of the final porous SiCO material and the pore architecture as well as the specific chemistry that are targeted. Here we discussed those supplies that we applied in this thesis work.

2.4.1 Polymethylhydrosiloxane

Polymethylhydrosiloxane (PMHS), or polyhydridomethylsiloxane (PHMS) in some studies,[112-113] in is a transparent liquid silicone oil possessing low viscosity and widely used as mild reducing agent to transfer hydrides to metal complexes in organic chemistry.[114] Some properties of PMHS are reported in table 2-1, collected from various datasheet from reference literature, Sigma-Aldrich, and Alfa Aesar.[115-116] The polymer used in this thesis work was purchased from Sigma-Aldrich and possessed an average M_n ~1,700-3,200, viscosity of 12-45 cP, and density of 1.006 g/mL at 25 °C. It has a linear structure and does not any crosslinking functional group to form a network through the aging process. Therefore, it must be modified to be crosslinked prior annealing to be used as a pre-ceramic. There are two typical ways of modification reported in literature. As it is shown in Figure 2-6, PMHS has Si-H group. A first method is converting part of the Si-H moiety to Si-OH, so Si-OH groups can then go through condensation reactions and produce oxygen bridges.[117] Another route, first reported by Y. Blum,[118-119] is to use the Si-H bonds to crosslink and functionalize the polymer with a vinyl bearing moiety in another siloxane polymer or a small molecule that has a unsaturated bond enable to do hydrosilylation reaction described in Section 1.5.3. The later route was used in this thesis work and the small molecule with unsaturated moiety was divinylbenzene (DVB). Depending on the amount of DVB used, SiCO ceramic after annealing procedure yield different amount of free carbon content.[119] The FT-IR of PMHS is shown in the Figure 2-7.

Polymethylhydrosiloxane	
Appearance	Transparent
Density	1.006 g/mL at 25 °C
Viscosity	12-45 cPs
Flash Point	204 °C
Moisture sensitivity/absorption	Slightly moisture sensitive
Storage	Cool and dry place, no special requirements

Table 2-1. Physical properties of PMHS.

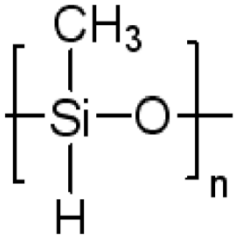

Figure 2-6. Structural formula of PMHS.

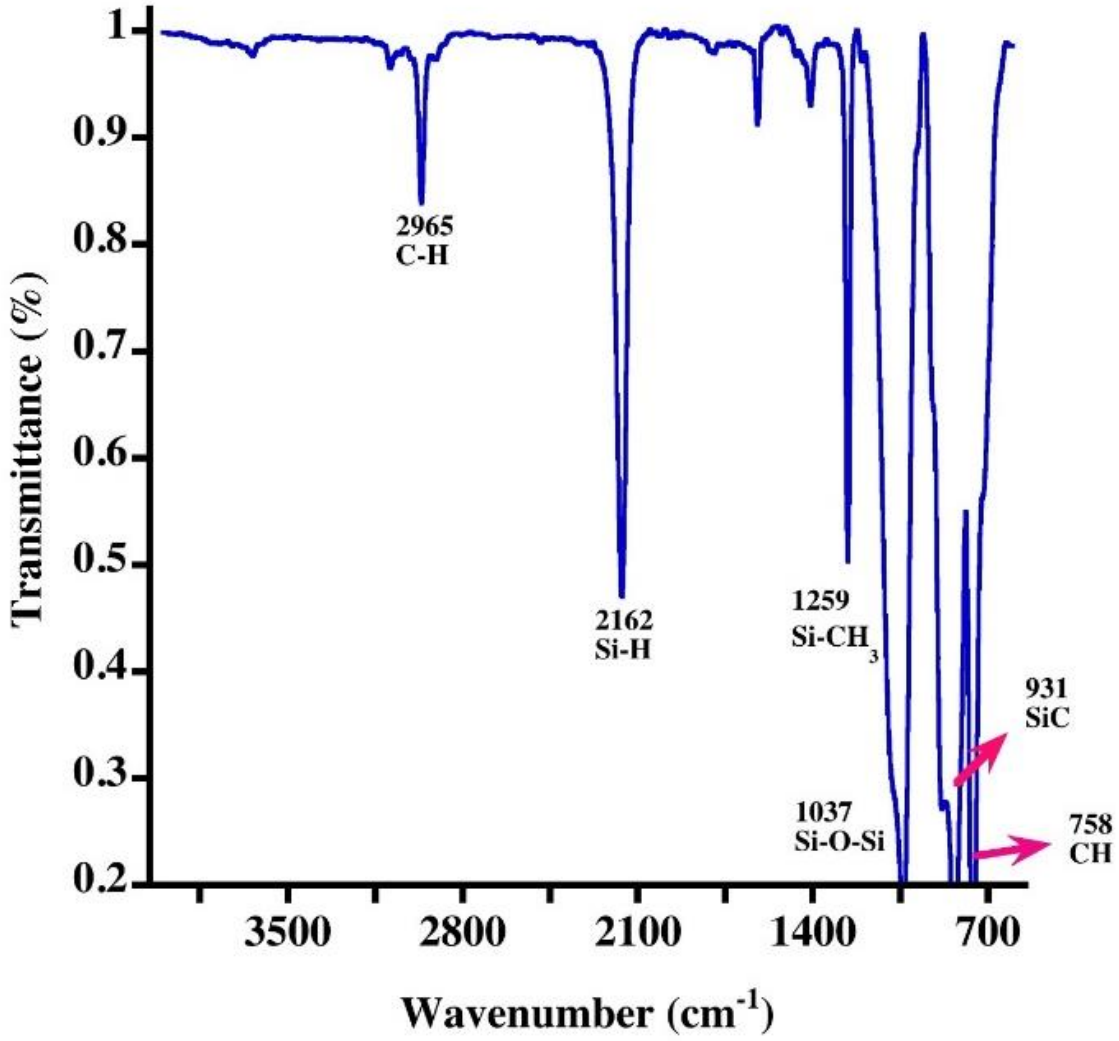

Figure 2-7. FT-IR spectrum of PMHS.

2.4.2 Crosslinking Agents

As it was noted before, PMHS can make a preceramic network by means of hydrosilylation reaction. This type of addition reaction is can be efficiently catalyzed by Pt compounds and it is free of by-products, allowing the curing of the pre-ceramic PMHS and the crosslinking agent at

low-to-mild temperature (RT to 200°C). In this work, two crosslinking agents, divinylbenzene and divinylthiophene, were used.

2.4.2.1 Divinylbenzene

Divinylbenzene (DVB), shown in the Figure 2-8, consists of an aromatic ring with two vinyl groups in ortho, meta, or para positions. The DVB used in this work was purchased from Sigma Aldrich. It is a technical grade and it is a combination of meta and para isomers. It is a colorless transparent liquid with a sharp odor. Although it contains 1% of polymerization inhibitor this bottle must be stored in a cold place (2-8 °C). The FT-IR spectrum of DVB is reported in Figure 2-9 and confirms the structure is the mixture of o- and m- disubstituted benzene.

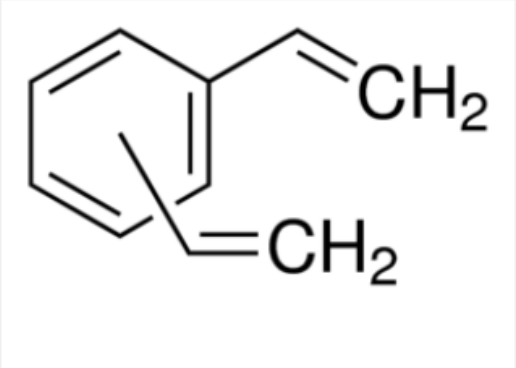

Figure 2-8. Structural formula of DVB.

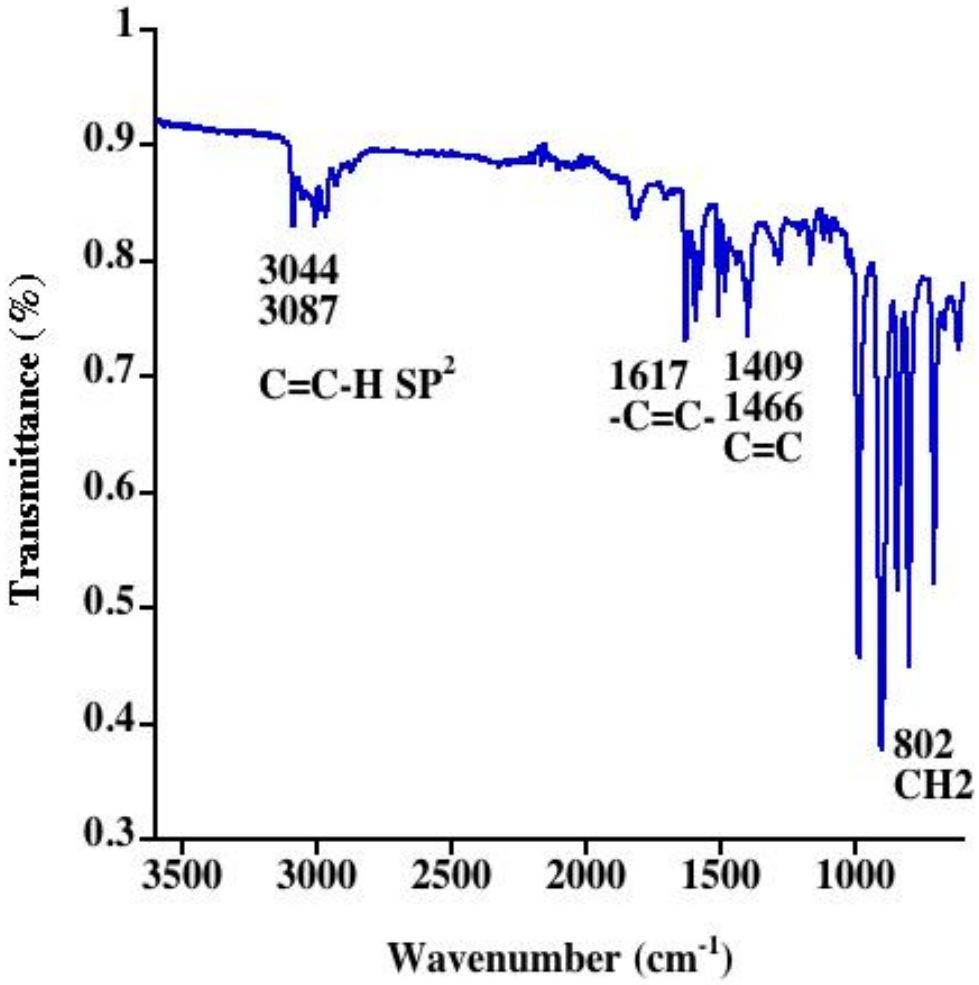

Figure 2-9. FT-IR spectrum of DVB.

2.4.2.2 Divinylthiophene

2,5 divinylthiophene, shown in the Figure 2-10, was prepared via a collaboration with Dr. Junha Jeon at University of Texas Arlington. This molecule is a sulfur-containing unsaturated five-member ring with two-fold vinyl donor. It is a yellow or orange transparent liquid. It should be

stored in an inert or vacuum dry place. Also, it should be used in 2-3 days after synthesis because it can go through self-polymerization.

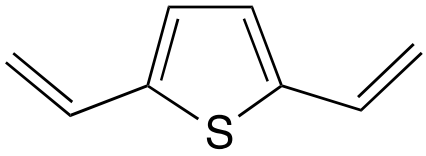

Figure 2-10. 2,5-Divinylthiophene.

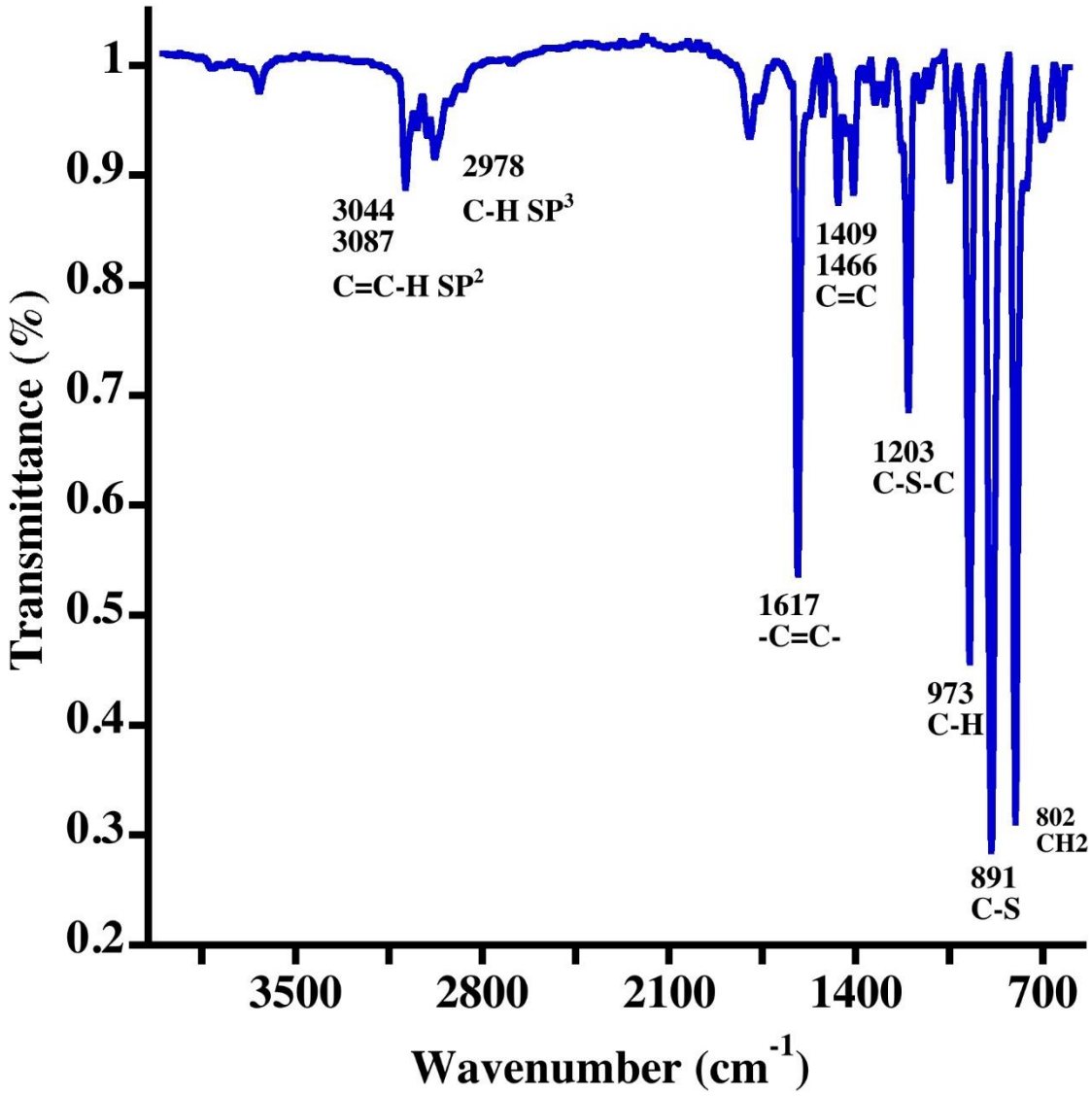

Figure 2-11. FT-IR spectrum of DVT.

2.4.3 Catalyst

1,3-divinyl-1,1,3,3-tetramethyldisiloxane, known as Karstedt's catalyst, is a powerful catalyst to conduct a hydrosilylation reaction. It was described in the Section 1.5.3 and shown in the Figure 1-8 previously. It consists of a Pt (0) organometallic compound in which the platinum atoms are

coordinated with the vinyl groups. It should be kept in an inert or vacuum dry place. It can be dissolved in most of organic non-polar solvents. It was purchased from Sigma-Aldrich in a xylene solution containing 2% of Pt.

2.5 Solvent Choice and Solvent Effects

The precursors and the synthesis conditions can introduce specific physical and chemical properties to the final SiCO ceramics by introducing specific microstructure, porosity, the content of free carbon, and specific functionality. One of the important synthesis conditions is the solvent and its interaction with the preceramic polymer.

2.5.1 Solubility Rules

The basic principle “like-dissolve-like” is a qualitive way to predict the solute and solvent interactions. For example, alcohols such as ethanol dissolve in water as they are polar molecules with ability to have hydrogen bonds with water whereas oils like vegetable oils do not dissolve in water as they are nonpolar and aprotic. However, there is a degree of solubility among alcohols in water. Ethanol is completely miscible in water whereas butanol solubility is not easy, and octanol is insoluble in water. Measuring the solubility of a substance in a solvent quantitatively is essential for industries such as paint and coating. There have been many methods to correlate a substance solubility in a solvent.

2.5.1.1 Hildebrand Solubility Parameter

A quantitative method for measuring solubility of materials in different solvents was pioneered last century by Hildebrand[120] and Scatchard,[121] clearly in a more recent text. [122] Hildebrand used the term "solubility parameter" for the first time to describe the miscibility behaviors of nonpolar regular solutions, and correlated solubility with the "cohesive properties" of the solvents. This empirical approach presumes, among other idealized assumptions, that there is no change in volume on mixing, and that the cohesive energy of the mixture is the geometric mean of that of the pure components. These and other limitations, e.g., the absence of effects of second nearest neighbors, have been discussed by Hildebrand contemporaries.[120, 123] From thermodynamics, the Gibbs free energy change on mixing, ΔG_m, is dependent on the enthalpy change, ΔH_m, and the entropy change, ΔS_m, on mixing are related by equation 2-1:

$$\Delta G_m = \Delta H_m - T\Delta S_m \qquad (2\text{-}1)$$

Mixing occurs spontaneously when the free energy change is negative. The dissolution of polymeric macromolecules s accompanied by a slight increase in entropy (almost zero change). Therefore, enthalpy becomes the only key factor in determining the sign of the Gibbs free energy change. Hildebrand et al., approximate the enthalpy of mixing by the equation 2-2, where V_{mix} is the volume of the mixture, ΔE_i^v is the energy of vaporization of species i, V_i is the molar volume, and $\emptyset_i$ is the molar volume fraction of i in the mixture:

$$\Delta H_m = V_{mix}[(\frac{\Delta E_1^v}{V_1})^{1/2} - (\frac{\Delta E_2^v}{V_2})^{1/2})]^2 \emptyset_1 \emptyset_2 \qquad (2\text{-}2)$$

The cohesive energy, E, is the energy required to break all intermolecular forces. When E divided per unit volume the value for cohesive energy density, CED, is obtained as it is described in the equation 2-3:

$$CED = \frac{E}{V} = \frac{[\Delta H_{vap} - RT]}{V} \quad (2\text{-}3)$$

Hildebrand defined the solubility parameter, δ, as the square root of cohesive energy density described in the equation 2-4:

$$\delta = (\frac{E}{V})^{\frac{1}{2}} \quad (2\text{-}4)$$

So, the equation 2-2 can be rewritten as the equation 2-5:

$$\Delta H_m = V_{mix}[(\delta_1 - \delta_2)]^2 \emptyset_1 \emptyset_2 \quad (2\text{-}5)$$

For $\Delta G_m \leq 0$ in the equation 2-1, the heat of mixing, ΔH_m , must be smaller than the entropic term, $T\Delta S_m$. Therefore, the difference in solubility parameters, $(\delta_1 - \delta_2)$, must remain small.

2.5.1.2 Hansen Solubility Parameters

As suggested, while the Hildebrand parameters provide numerical estimates of the degree of interaction between the liquid components in certain mixtures, a major shortcoming is the restriction to regular solutions, which do not include molecules with polar and hydrogen-bonding interactions. Hansen in 1967 extended the Hildebrand concept to repair this deficiency. He proposed breaking the cohesive energy into three constituent parts: dispersion (D), polar (P), and hydrogen-bonding (H) interactions.[124] This sort of decomposition of solvation interactions for mixtures has been used widely, perhaps first by spectroscopists,[125] and probably most prolifically by analytical chemists.[126] Hansen's definition is described in equation 2-6:

$$E = E_D + E_P + E_H \quad (2\text{-}6)$$

Dividing this equation by the molar volume gives the square of the total Hildebrand's solubility parameter as the sum of the squares of the Hansen components as it is written as the equation 2-7:

$$\frac{E}{V} = \frac{E_D}{V} + \frac{E_P}{V} + \frac{E_H}{V} \quad (2\text{-}7)$$

By knowing the definition of δ from the equation 2-4, the equation 2-7 can rewrite as the equation 2-8:

$$\delta^2 = {\delta_D}^2 + {\delta_P}^2 + {\delta_H}^2 \quad (2\text{-}8)$$

These three parameters can be measured experimentally such that solubility distance, R_a , can be calculated for any solute−solvent combination as it is written as the equation 2-9:

$$\left({R_a}^2\right) = 4\,(\delta_{D2} - \delta_{D1})^2 + (\delta_{P2} - \delta_{P1})^2 + (\delta_{H2} - \delta_{H1})^2 \quad (2\text{-}9)$$

To maximize solute interactions, one must choose a solvent, which minimizes this distance. The factor of "4" of the dispersion term is predicted by the Prigogine corresponding states theory of solutions[127] when the geometric mean is used to estimate the interaction in mixtures of dissimilar molecules. Also, it has been found to be convenient to plot solubility data as a sphere. Therefore, any solute has a sphere in three-dimensional Hansen space, with dispersion, polar, and hydrogen bonding forces as the three axes, in which all the good solvents for the solute exist inside the sphere while all the poor solvents are excluded from the sphere. The three component values for Hansen Solubility Parameters (HSP) are well-studied for many conventional solvents. So, each solvent is represented by a point in a Hansen three-dimensional space. The solubility of a solute in some of the solvents with known values can be measured and the solubility results can be recorded. At some point the solute will phase separate with some solvents, which defines a boundary on that line. By collecting the solubility data of various solvents, a sphere can be fit in which all the soluble solvents (points) are within the sphere while all the insoluble solvents are outside of it. The center of this sphere is then the three-dimensional solubility parameter of the solute with the radius of the sphere defined as the radius of interaction, R_0. Comparing the solubility distance, R_a, and the

radius of interaction, R_0, defines how far solute and solvent are in a solubility space. Dividing the solubility distance by the radius of interaction results the "relative energy distance" (RED), which determines the solute-solvent compatibility quantitatively in the equation 2-10:

$$RED = \frac{R_a}{R_0} \tag{2-10}$$

If the RED is 0, then the solubility parameters of the solute and the solvent are exactly matched, and there is no energy difference between two. If the RED is less than 1, then the solute and the solvent are compatible, and they interact with each other. A value at or close to 1 is a boundary condition and above 1the solute cannot be dissolved in that solvent. For the solvents with RED values between 0 and 1 higher values indicate lower affinities. Thus, if there are two solvents existing in the solute's Hansen sphere with RED values between 0 and 1 the "good" solvent will be the one that has lower value of RED whereas the "bad" solvent will be the one that has higher value of RED. While simplistic and burdened by some of the same approximations of the original analysis, this approach has provided a consistently good and practical guide for relative polymer-solvent interactions, except for pathologic cases with more exotic interactions. For example, it can be problematic with the temperature dependence of mixing, and solvent specific effects that involve solvent exclusion.

2.6 Polymer Swelling and Hansen Solubility Parameters

Polymers, that they have been vulcanized and formed a network by crosslinking, swell in contact with a given solvent. Previous studies show that it is possible to correlate different degrees of swelling in corresponding crosslinked polymer with the HSP based on total solubility of the polymer before crosslinking.[124, 128] Hence, the solvents that dissolve the polymers before

crosslinking are also those that swell the crosslinked polymers most. Likewise, larger differences in HSP between solvent and polymer led to lesser degrees of swelling.

2.6.1 Hansen Solubility Parameters of PMHS

The SiCO aerogels synthesized with the same precursors but obtained in different solvents show different porosity values.[95] This mechanism involves 3 steps:

1- Crosslinking of the monomers in solution forming oligomers.

2- Precipitation of the crosslinked polymeric nuclei.

3- Particles' aggregation and growing toward the final gel structure.

Unfortunately, no solubility parameters exist of the PMHS-DVB system in the literature. In this thesis work we investigate the Hansen solubility parameters (HSP) for polymethylhydrosiloxane (PMHS) a polymer used for the synthesis of silicon oxycarbide ceramic aerogels. For explaining the interaction strength between a solvent and a polymer HSP theory was applied in this study. This theory defines three parameters (δD, δP, δH,) providing a quantitative measure characterizing the energy density associated with these interactions described in the Section 2.5.1.2. Methyl-terminated PMHS (Mn = 1700-3200, CAS# 63148-57-2) was purchased from Sigma-Aldrich. The polymer was first immersed in 23 solvents listed in Table 2-2 in the way that 10 mL of each solvent was placed into a 20 mL vial and then 1 mL of PMHS was added to the solvent. The vials are shown in the Figure 2-12. Each mixture stirred for 7 days to eliminate any kinetic effects. Then the solubility of the polymer in each solvent was observed and recorded. The degree of solubility was estimated with a coarse "solubility-rating" in the way that rating of "Soluble" corresponded to a dissolved state and rating of "Insoluble" represented an insoluble state. HSPs of PMHS was

then determined by least-square approaches using the known HSP of solvents and the software package HSPiP (version number 4.1.03, published by Charles M. Hansen in 2016).

Figure 2-12. A collection of 23 solvents were prepared for the solubility test of PMHS. Molecular sieves were added to the vials of solvents to absorb moisture.

Solvent	δ_D ($MPa^{1/2}$)	δ_P ($MPa^{1/2}$)	δ_H ($MPa^{1/2}$)	Solubility
Acetone	15.5	10.4	7	Soluble
1-Bromopropane	16.4	7.9	4.8	Soluble
Butyric anhydride	15.8	10.3	4.5	Soluble
ϒ-Butyrolactone	18	16.6	7.4	Insoluble
Cyclohexane	17.2	1	2	Soluble
Di-n-Butyl ether	15.2	3.4	3.2	Soluble
3,4-Dichlorotoluene	19.8	9.8	2.5	Soluble
m-Dichlorobenzene	19.2	5.1	2.7	Soluble
Diethyl ether	14.5	2.9	4.6	Soluble
Dimethyl carbonate	15.5	8.6	9.7	Insoluble

1,4-Dioxane	17.5	1.8	9	Soluble
Glycerol	17.4	11.3	27.2	Insoluble
n-Hexane	14.9	0	0	Soluble
Isopentane	13.8	0	0	Soluble
Mesitylene	18	0.6	0.6	Soluble
Methyl Cyclohexane	16	9	5.1	Soluble
Pentane	114.5	0	0	Soluble
1,1,2,2-Tetrachloroethane	18.8	5.1	5.3	Soluble
Tetrachloroethylene	18.3	5.7	0	Soluble
Tetrahydrofuran	16.8	5.7	8	Soluble
Toluene	18	1.4	2	Soluble
1,1,1-Trichloroethane	16.8	4.3	2	Soluble
p-Xylene	17.8	1	3.1	Soluble

Table 2-2. Solubility of PMHS precursor in 23 solvents.

Subsequently, the data were inserted to the HSPiP program to calculate the Hansen solubility parameters for PMHS as it is shown in the Figure 2-13.

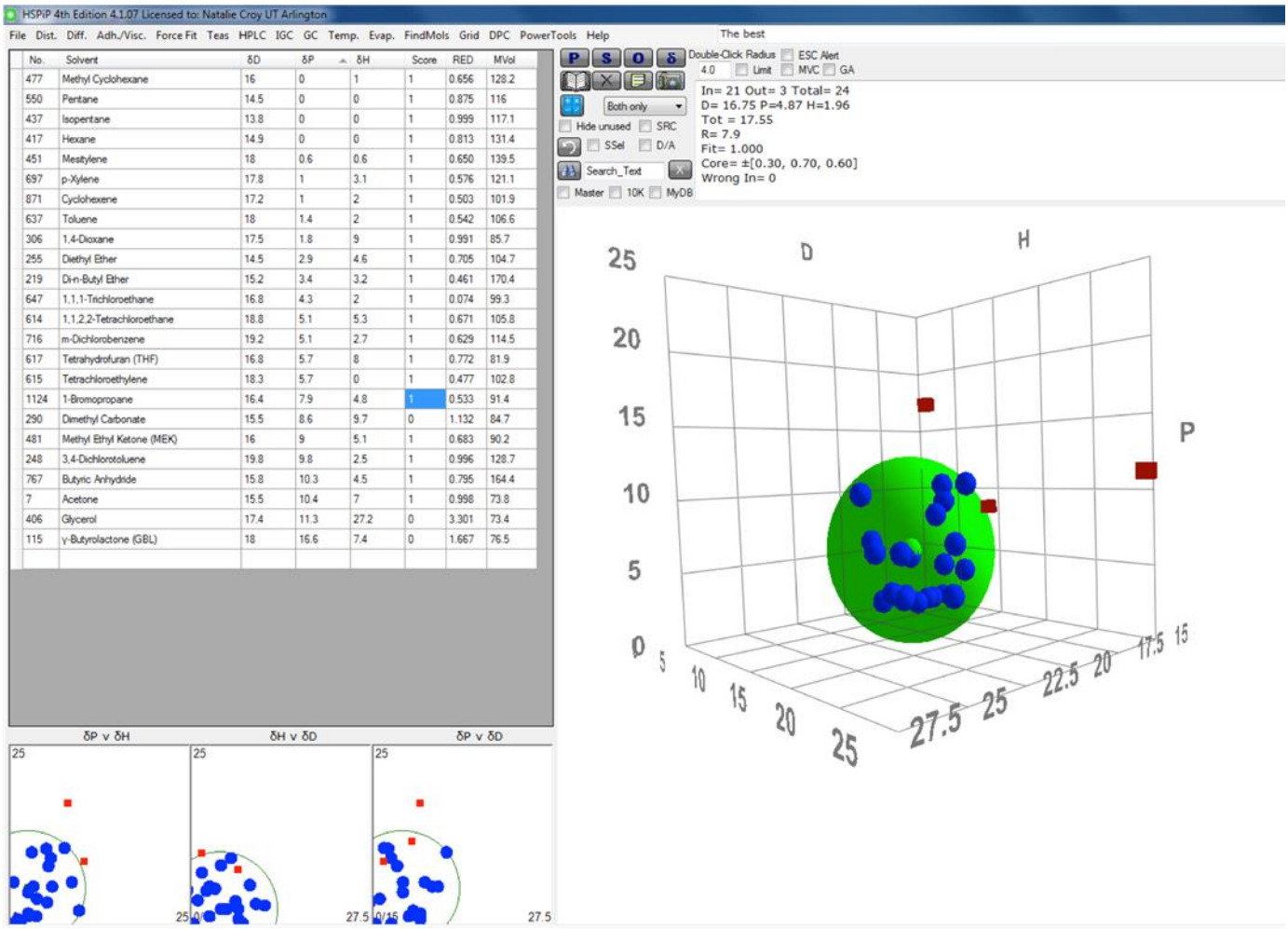

Figure 2-13. Program interface for calculation of the HSP values of the PMHS.

The program interface for the calculation of the HSP values of the PMHS precursor based on the solubility demonstrated that the HSP values are δD= 16.75, δP = 4.87, and δH = 1.96 $MPa^{1/2}$.

Polydimethylsiloxane has a similar structure to PMHS and different studies Hansen solubility parameters of polydimethylsiloxane (PDMS) have been applied to predict PMHS and solvents' interactions so far.[129-130] Comparing those values demonstrated that PDMS and PMHS have similar dispersion values whereas polar solubility parameter δP of PMHS is larger than PDMS due to lack of symmetry of two methyl groups attached to Si in the backbone of PDMS. δH value of the hydroxy terminated PDMS is also larger than δH of PMHS because of hydroxy group available in the PDMS probably contributed to the hydrogen bonding solubility parameter. The comparison of the Hansen parameters between PMHS and PDMS is listed in the Table 2-3.

Polymer	δ_D ($MPa^{1/2}$)	δ_P ($MPa^{1/2}$)	δ_H ($MPa^{1/2}$)	Terminal group
PDMS	16.86	0.12	8.60	Hydroxy
PMHS	16.75	4.87	1.96	Methyl

Table 2-3. Comparison between Hansen solubility parameters of PDMS and PMHS

2.7 Effect of Solubility/Swelling PMHS-DVB Wet Gels

We further used the HSP values of PMHS to predict swelling degree of aerogels made of PMHS and DVB using acetone and cyclohexane and compared them to the experimental data. Two mixtures were prepared with 1:2 mass ratios of PHMS and DVB. Subsequently, 85 % volume of acetone was added to the one mixture and 85 % volume of cyclohexane was added to the other one inside two separate Parr digestion vessels. After these mixtures stirred for 5 minutes, 10 µL of Karstedt's catalyst was added to each vessel. Then the vessels were located inside two separate pressure reactors to crosslink at 150 °C for 3 hours in an oven. Afterward, the wet gels were

extracted from the vessels. First, the wet gels were washed 5 times with the same solvent that they were synthesized to wash off the catalysts and unreacted materials. The diameter and height of each wet gel was measured for each wash. Next, three solvent mixtures of acetone and cyclohexane (25:75, 50:50, 75:50 volume ratio) were prepared. Each wet gel was immersed in each of these mixtures and washed until the measurement of diameter and height of each wet gel remained constant. The volume of each gel in each of these solvent mixtures was plotted and the swelling/shrinkage behavior of each gel was observed as it is illustrated in the Figure 2-14 and listed in the Table 2-4. Consequently, based on Hansen solubility parameters the swelling/shrinkage PMHS in acetone, cyclohexane and the binary solvent mixtures were calculated. This data set was compared to the volume change in the solvents.

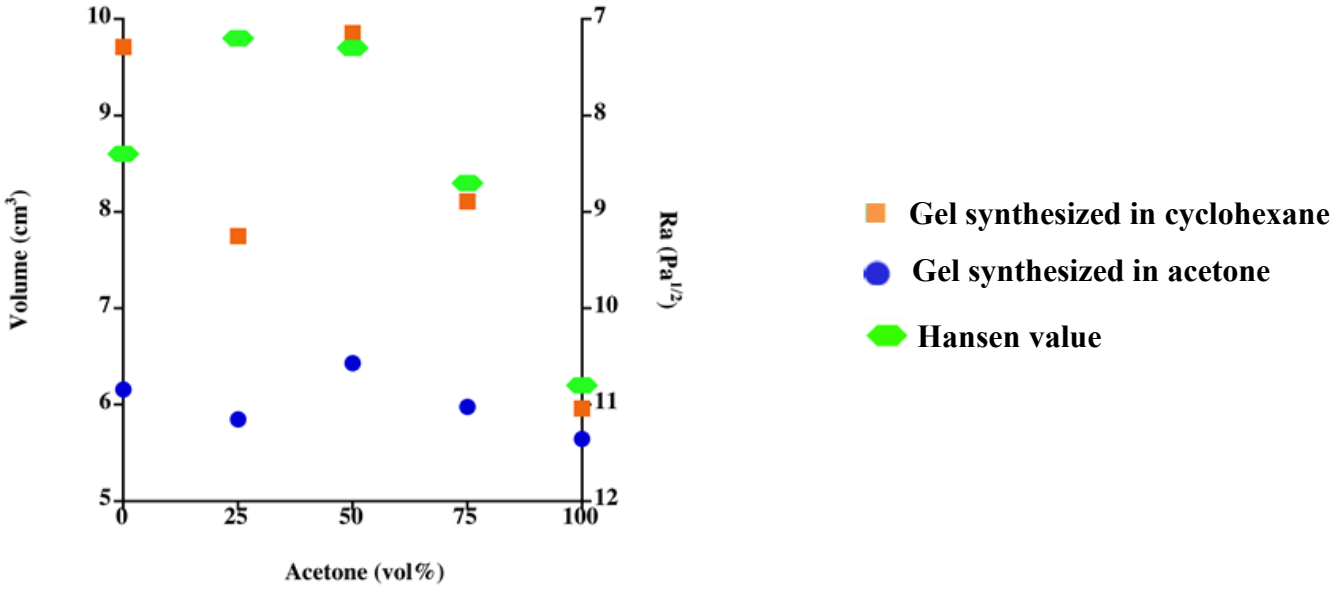

Figure 2-14. Volume change of the wet gels synthesized in cyclohexane and acetone in different volume percentage of acetone and relation of the swelling/shrinkage of the gels with Hansen solubility parameter.

Cyclohexane	16.8	0.0	0.2	8.4
Acetone: Cyclohexane (25:75)	16.5	2.6	1.9	7.2
Acetone: Cyclohexane (50:50)	16.2	5.2	3.6	7.3
Acetone: Cyclohexane (75:25)	15.8	7.8	5.3	8.7
Acetone	15.5	10.4	7.0	10.8

Table 2-4. Calculation and prediction of the swelling/shrinkage PMHS in acetone, cyclohexane and the binary solvent mixtures based on Hansen solubility.

Based on the observation the wet gel synthesized in the cyclohexane swelled more that the gel synthesized in acetone. The comparison was aligned with the experimental results. However, the wet gels behavior at 25:75 vol% ratio of acetone was not aligned Hansen values and prediction, and this could be because acetone and cyclohexane mixture behave non-ideal and form an azeotrope as well. It is worthy to mention that the swelling of the individual particles have not determined, which can be done by Dynamic Light Scattering technique (DLS) to show the consistency with the gel matrix. The study might help resolve the inconsistency in the data at low acetone concentrations.

2.8 Conclusion

The reagents, the experimental methods, and the equipment for obtaining produce porous silicon oxycarbide pre-ceramic and ceramic were described. The gels are obtained in highly diluted conditions via hydrosilylation reaction of PMHS bearing Si-H groups and cross-linking it with carbon-carbon double bonds of DVB. Polymer aerogels are obtained after solvent exchange with liquid CO_2 and subsequent supercritical drying.

Solubility of PMHS in various solvents was quantitatively investigated via Hansen Solubility Parameters rules for the first time. Also, the swelling/shrinkage of PMHS-DVB aerogel in acetone, cyclohexane and the binary solvent mixtures were predicted based on Hansen solubility parameters and compared to the experimental data. The comparison suggested that the experimental data follows HSP prediction of swelling behavior of PMHS-DVB aerogel in solvents and the solvent mixtures except at 25:75 vol% ratio of acetone. This could be due to non-ideal behavior the solvents mixture and formation of the azeotrope between cyclohexane and acetone.

CHAPTER III: DIFFERENTIAL HYSTERESIS SCANNING OF NON-TEMPLATED MONOMODAL AMORPHOUS AEROGELS

Poroshat Taheri, John C. Lang, Jeffrey Kenvin and Peter Kroll

Published in Physical Chemistry- Chemical Physics (2021)[131]

ABSTRACT

We perform Differential Hysteresis Scanning (DHS) Porosimetry of amorphous silicon oxycarbide aerogels to quantify hierarchical connectivity in these porous materials. We contrast high-resolution argon sorption scanning isotherms of samples obtained through a non-templated synthesis using different solvents, and characterize respective changes after calcination at 1000 °C. The multi-scan DHS data sets are analyzed through non-negative least-squares deconvolution using a kernel of theoretically derived isotherms for a selection of hierarchical geometries using non-local density functional theory (NL-DFT). We obtain two-dimensional contour plots that characterize mesopores according to the ratio between pore diameter and its connecting window. Combined information from DHS and complementary BET and BJH approaches reveals one system with monomodal distribution both in pore diameters and in window diameters. Hence, this

amorphous material exhibits a uniformity usually only observed for crystalline systems. We demonstrate that DHS analysis provides quantitative data analyzing the hierarchical structure of mesoporous materials and unlocks pathways towards tailored materials with control of surface heterogeneity, localization, and sequential accessibility – even for amorphous systems.

1. Introduction

Quantitative assessment of gas sorption using simple gases has matured from its beginnings in the early 1900's to become a conventional technique for investigating surface heterogeneity, structural morphology and thermodynamics of porous materials.[132-133] This technology has been applied effectively for studies of materials with both meso- (~ 2-50 nm) and micro- (< ~ 2nm) pores. Correspondences between characteristics of gas sorption isotherms and pore morphologies have been analyzed and systematized in IUPAC conventions.[23, 134] Based on phenomenological models and adsorbed volumes, surface areas can be established. On condensation of gas at higher pressures, the behavior of the adsorbed fluid provides information regarding pore volumes from which pore sizes, geometries and connectivity can be inferred. Staple methods to characterize meso-porous systems include Brunauer–Emmett–Teller (BET) analysis for calculation of specific surface area (SSA) and surface energetics,[12] and Barrett-Joyner-Halenda (BJH) analysis for determining distributions of average pore volumes and sizes.[31] Early refinements of these approaches were contributed by statistical thermodynamic interpretation of, and calorimetric data on, adsorption energetics,[133, 135-138] estimations of the adsorbed thickness of multilayer films,[139-141]

improved understanding of ordering in condensed phases,[142-143] and appreciation of the detailed structural information from observations of capillary condensation and adsorption hysteresis.[144]

More recently, with improvements in computational modeling and the convergence of results from density functional, molecular dynamics and Monte Carlo methods, statistical mechanical approaches have successfully investigated the influences of ever more complicated pore architectures, pore dimensionality, surface heterogeneity and molecular interactions in systems undergoing class 1 film growth.[145-146] Modeling of both structure and thermodynamics of porous materials of greater complexity has improved interpretations of experimental evaluations.[147-150] Non-local density functional theory (NLDFT) is an efficient statistical thermodynamic approach for analyzing the population density of a system of molecules interacting with a surface.[151-155] It has been used to describe the gradual buildup, and loss of solid-packing-like ordering, of multilayers in film formation and condensation as originally depicted in the BET model of adsorption. This method has become an efficient tool for analyzing and interpreting porous structures.[37, 150, 156] Complementary theoretical and experimental studies of well-characterized, highly ordered, templated materials, such as M41S,[157] have validated this theoretical foundation of gas sorption used for pore characterization.[158]

Cavities in a material can attain a variety of shapes and sizes, narrowly or broadly distributed, having a hierarchy of interconnectivity all influenced by the chemistry of the material and its preparation. Often contrasting and complementary structures are generated, dependent on whether the synthesis is a bottom-up arrangements of coalescing particles, i.e. the structural building blocks, or a top-down removal of fragments from an existing structure.[159] Cavities may be linked to each other creating an intrinsic network of pores. These structural features, combined

with different surface heterogeneity, can impact adsorption and desorption differently. In particular, hysteresis in gas sorption data indicates the presence of constrictions that regulate desorption from larger interconnected cavities, under control of the pore hierarchy.[159-162] There are few techniques to map the hierarchy of porous materials. X-ray tomography can be used for studying macroporous systems with a resolution of about 1 μm.[163-165] Transmission electron microscopy (TEM) is applied for ordered microporous materials such as zeolites and can reach a resolution of ~1 nm.[166-167] Early approaches of analyzing hysteresis loops observed in gas sorption focused on uniformly sized mesoporous systems.[168-171] In recent studies the Differential Hysteresis Scanning (DHS) technique was developed by one of us and applied to study pore hierarchy in crystalline faujasites.[149-150]

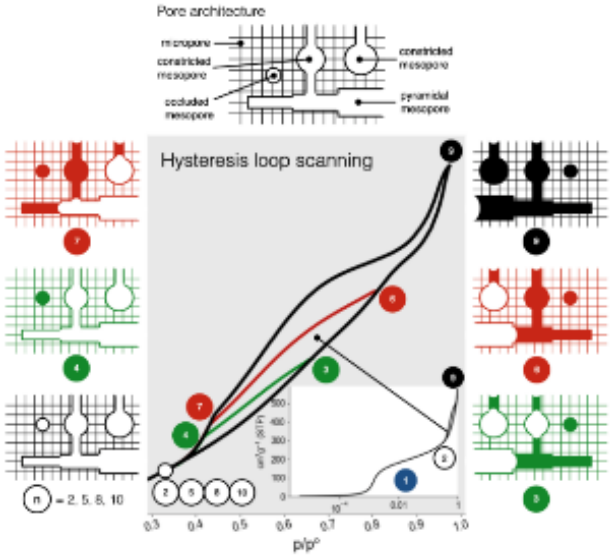

Fig. 1 Schematized sequence of filling and emptying of complex pores accompanying the sequential differential hysteresis scans (DHS).

The DHS technique is a rigorous analysis of the hysteresis loops and subloops observed when scanning the adsorption and desorption branches of an isotherm. Scanning isotherms may be obtained by several methods. The DHS technique analyses the hysteresis subloops formed by sequential increasing partial saturation of the pore network. An example of hysteresis subloops is illustrated in Fig. 1. The technique uses the difference between increasing levels of saturation from the component scans as input for the modelling. The systematic filling and emptying of the pores of the partially saturated network is suggested by the sequential numbering of the individual scans in Figure 1. The desorption branch of the isotherm is controlled by the dimension of the entrance to a pore, herein referred to as the window. The adsorption branch is influenced by the dimension of the larger cavity, referred to as the pore size. The DHS technique utilizes adsorption and desorption branches of the scans to establish the nature and relative distribution of the controlling windows and their connected pores. NLDFT models are employed to calculate the changes in pore size distributions required for modeling accurately the isotherm scans measured experimentally.

In this study we apply the DHS technique, which provides a modeling framework for analysis of different pore geometries, to address for the first time with this technique the structural heterogeneity in silicon oxycarbide disordered aerogels. With this method quantitative assessment of the distribution of pore sizes and geometries, and their morphological changes on calcination, have been determined for these heterogeneous hierarchical systems.

Silicon oxycarbide (SiCO) is a versatile material with modifiable functional properties dependent on synthesis and processing.[68, 172-173] Porous SiCO materials have been fabricated

through a variety of methods and their diverse applications explored,[68, 90] including as membranes for gas separation,[76] as macroporous hydrophobic fibers for environmental remediation,[174] and as anodes for lithium ion storage.[175] SiCO aerogels are synthesized from polymers or molecular precursors, have been processed with various heat treatments at elevated temperatures, and resulting porosities have been characterized.[112, 176-179] For further development of these porous materials in more demanding applications - e.g., for drug delivery,[180-182] separations,[76] and catalyst support[183] - knowledge and control of their pore hierarchy will be required. Here in this paper, we deliver new insight into the pore architecture of SiCO aerogels using a combination of both conventional gas sorption and Differential Hysteresis Scanning (DHS).

2. Preparation/Synthesis

2.1 Synthetic procedures

We synthesized SiCO aerogels by cross-linking polymethylhydrosiloxane (PMHS) with divinylbenzene (DVB) in excess solvent, either cyclohexane or acetone, via hydrosilylation.[177] PMHS (MW~1900, CAS: 63148-57-2), DVB (technical grade, 80%, CAS: 1321-74-0) and the Karstedt's catalyst (platinum divinylmethylsiloxane complex), ~2% in xylene (CAS: 68478-92-2) were purchased from Sigma-Aldrich, Saint Louis, MO, USA. Acetone (CAS: 67-64-1) was bought from Macron Fine Chemicals, VWR, Radnor, PA, USA, and cyclohexane (CAS: 110-82-7) was acquired from Fisher Scientific, USA. We prepared a solution of a 1:2 mixture (by mass) of PMHS and DVB in 85% (by volume) of either cyclohexane or acetone as solvents. We added 10 μL of Karstedt's catalyst to each

mixture, transferred it into a pressure reactor, and placed it in an oven at 150 °C for 6 hours, a temperature above the 1 atm boiling point of the solvent. Thereafter, the sample was gently removed from the reactor vessel and soaked repetitively for 6 hours, washing five times in the solvent used for the synthesis, adequate for removing all the catalyst and terminating the reaction.

In the next step, the sample was transferred carefully into a cylindrical CO2-reactor of in-house design. There are two glass windows at either end to permit visual inspection, useful for observing and controlling solvent exchange with liquid CO_2 and for monitoring the supercritical drying process. Each gel was washed with liquid CO_2 at 4 ˚C twice per day for a total of 10 solvent exchanges. Subsequently, the final step of the drying process was performed over a 10-hour period by slowly increasing the temperature to 45 ˚C at a pressure of 100 - 110 bar. After supercritical drying in a CO_2-reactor we recovered **p**olymeric **a**erogels (**pa**). The **p**olymeric **a**erogel (**pa**) synthesized in **c**yclohexane was labelled **pa-c** and the **p**olymeric **a**erogel (**pa**) synthesized in **a**cetone was labelled **pa-a**. Extracting the solvent in the supercritical dryer led to shrinkage of the samples. Therefore, the height and diameter of the (almost) cylindrical **pa-c** and **pa-a** aerogels were measured before and after supercritical drying using a graph paper. Bulk densities of samples were calculated using measured volume and mass of **pa-c** and **pa-a**. The linear shrinkage was 37% for **pa-c** and 18% for **pa-a** after supercritical drying. Their bulk densities were 0.7 g cm^{-3} for **pa-c** whereas 0.3 g cm^{-3} for **pa-a** respectively, a ratio comparable to the inverse of their ratio of total pore volumes.

Subsequent annealing to 1000°C in flowing nitrogen transformed these polymeric aerogels into their **c**eramic **a**erogel analogs (**ca**). The ramp from room temperature to 400 °C used a heating rate of 5 °C min^{-1}, and then temperature was kept for 2 hours at 400 °C. Thereafter, the sample was heated from 400 °C to 1000 °C with a heating rate of 5 °C min^{-1}, after which temperature was held at 1000 °C for 4 hours. The furnace was then switched off and samples allowed cooling to room temperature. The **c**eramic **a**erogel (**ca**) synthesized in **c**yclohexane was labeled **ca-c** and the **c**eramic **a**erogel (**ca**) synthesized in **a**cetone was labeled **ca-a**. We have chosen this system because, while dense SiCO ceramics synthesized from polymeric PMHS-DVB are well-known and well-characterized,[68, 86, 178] their pore morphology, and attributes controlling it, remain to be fully elucidated.[177, 184-185]

2.2 Scanning Electron Microscopy (SEM)

We characterized the pre-ceramic aerogels using Scanning Electron Microscopy (Hitachi S-4800 II FE SEM) by looking at fracture surfaces of **pa-c**, **pa-a**, **ca-c**, and **ca-a**. Due to the low electrical conductivity of the **pa-c** and **pa-a** sample, they were coated with silver (CrC-100 Sputtering System) (Plasma Sciences Inc, Ooltewah, TN). For particle size determination we used ImageJ software.[186] In the SEM image 145 pixels correspond to 1 μm. For estimating average particle size, we measured the diameters of for 25 particles with distinct boundaries in each SEM image.

2.3 Porosity

Nitrogen (at 77 K) and argon (at 87 K) sorption characteristics were measured using a Micromeritics ASAP 2020 porosimeter. We applied the Brunauer–Emmett–Teller (BET) analysis for calculating specific surface area (SSA),[12] and Barrett-Joyner-Halenda (BJH) procedure using desorption branch of the isotherms to estimate their pore size distribution (PSD).[31] The total pore volume (TPV) was taken directly from the maximum of the isotherm. BJH pore size distribution can be unreliable for pores lower than 6 nm.[187] Therefore, the pore size distribution graphs have the lower limit of 6 nm. All isotherms shown in Figures 5 and 6 are classified as Type IV (a) according to IUPAC.[18]

2.4 Differential Hysteresis Scanning (DHS)

We carried out Differential Hysteresis Scanning (DHS) measurements by high-resolution argon sorption on the pre-ceramic **pa-a** and **pa-c** as well as annealed **ca-a** and **ca-c** using Micromeritics ASAP 2020. Scanning isotherms were acquired by incrementally increasing the partial saturation of the sample followed by a high-resolution desorption (Figure 5). In total, 14 scans for each sample were collected. The pressure table for each sample was designed individually based on the maximum quantity of gas adsorbed at a P/P_0 of 0.98 so that 14 scans were adequate to cover the whole hysteresis region uniformly. A completed DHS experiment of a single sample took approximately 4 days. The distribution of pore window sizes and pore diameters as well as incremental pore volumes were calculated by the system software using non-negative least-squares (NNLS) deconvolution of the

scanning and differential isotherms based on the weightings from a kernel of model adsorption isotherms generated from the Tarazona version of the NLDFT with specific Lennard−Jones solid− fluid (sf) and fluid−fluid (ff) parameters for the sample material.[153] Here, three basic types of mesopores are considered according to the relative diameter of the window: pyramidal (d_{pore} > 2 nm, d_{win} > d_{pore}), constricted (d_{win} > 2 nm, d_{win} < d_{pore}), and occluded (d_{win} < 1 nm, d_{win} < d_{pore} /10). That the domains for the DHS contour plots may not extend to these limits reflects the size of the hysteresis loops under investigation.

3. Results and Discussion

3.1 SEM Analysis: Network's Constituent Colloidal Particles

The polymeric aerogels (Fig. 2, top) appear milky white in color while, with reduction occurring on annealing, the ceramic aerogels turn black (Fig. 2, bottom).

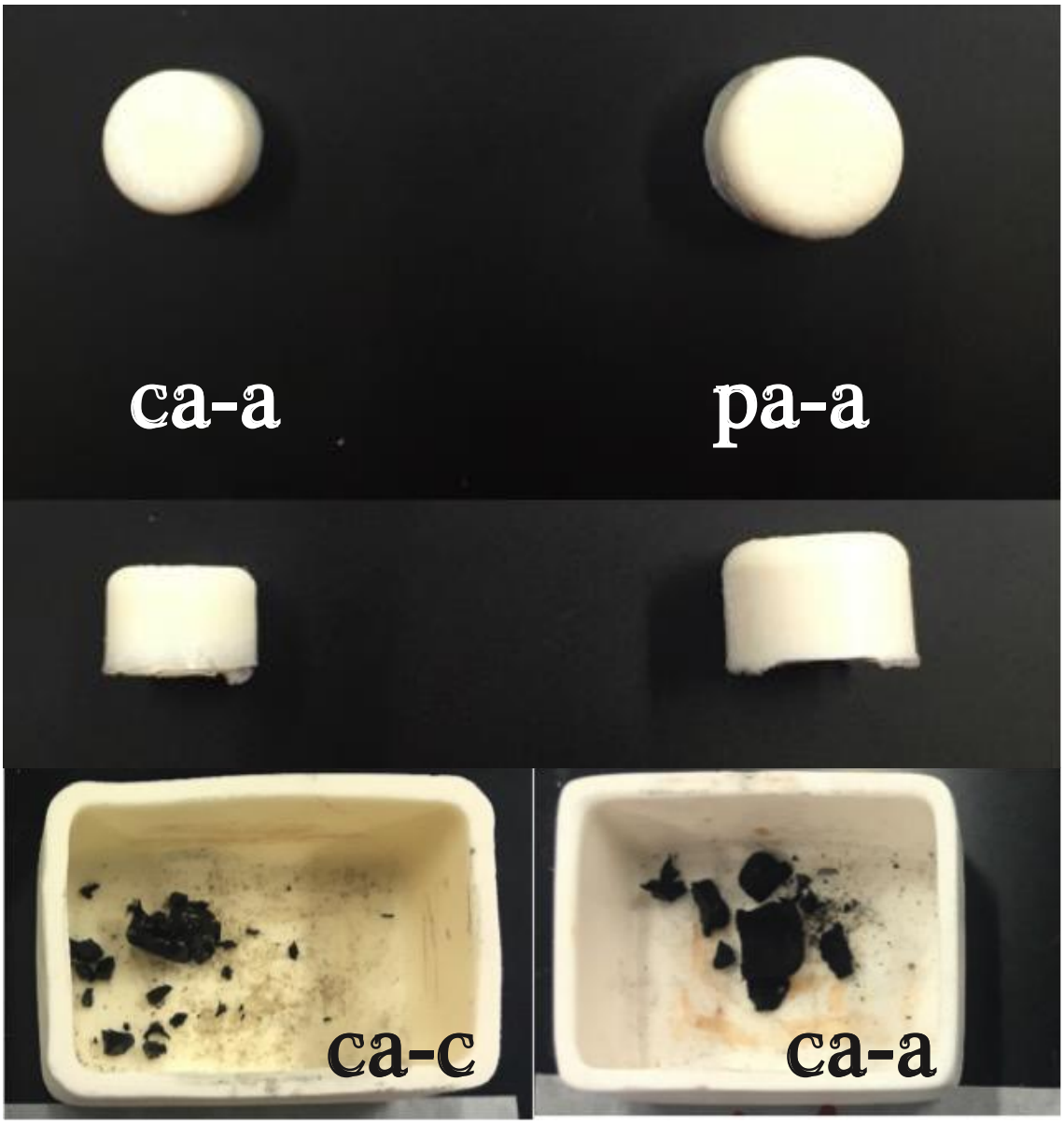

Fig. 2 Pictures of polymeric (top) and ceramic (bottom) SiCO aerogels. **pa-a** (right) and **pa-c** (left) are shown from top and side angle. **ca-a** (right) and **ca-c** (left) as received after annealing at 1000 °C in nitrogen.

The SEM micrographs in Fig. 3 show that microstructures of the polymeric aerogels consist of almost spherical colloidal particles. Particles in the annealed ceramics, **pa-c**'s, are fused closely together without significant space between the individual particles. In contrast, packing of spheres

in **pa-a** is less dense, with more open spaces and large cavities visible between individual and paired or fused spheres. We determined an average particle size of 160 ± 26 nm and 200 ± 31 nm for **pa-c** and **pa-a**, respectively. After annealing, the **ca** particles have coalesced, and while it is possible to identify large holes in the surface, it is impossible to differentiate individual particles. Note that the resolution of the electron micrographs does not allow examination of the mesoporosity in the aerogels.

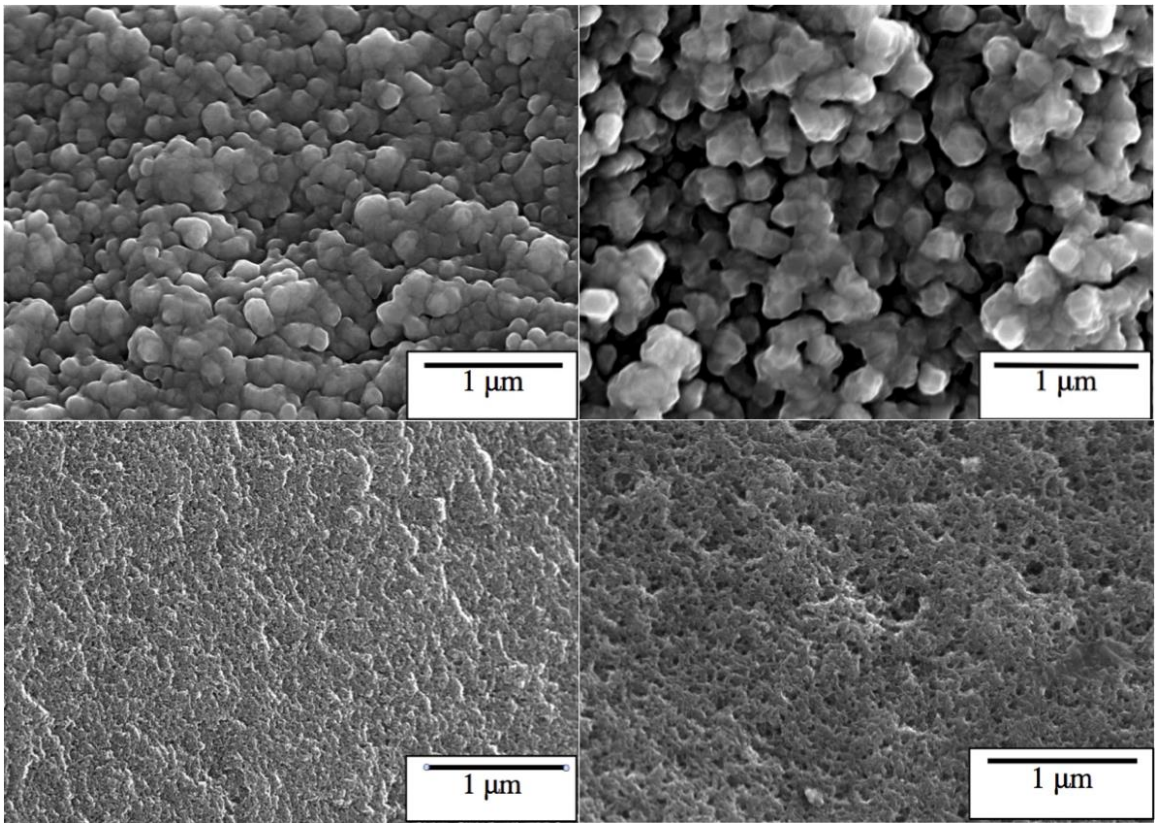

Fig. 3 SEM micrographs of pre-ceramic polymeric aerogels prepared in acetone **pa-a** (right, top), and prepared in cyclohexane **pa-c** (left, top); the annealed ceramic resulting from the aerogel prepared in acetone, **ca-a** (right, bottom), and the ceramic prepared in cyclohexane **ca-c** (left, bottom) at 30K resolution.

3.2 BET and BJH Analysis of Isotherms

Gas sorption isotherms for polymeric and ceramic aerogels obtained using nitrogen and argon are shown in Fig. 4a, eight isotherms in all. Previous porosity studies of SiCO used nitrogen as sorbent gas.[177, 185] For each of the four samples, a comparison between the Ar and N_2 sorption data is provided, illustrating the consistency between adsorbates, and thereby relating our observations to the previous work. Fig. 4b provides the Barrett-Joyner-Halenda (BJH) pore size distributions derived from the desorption branches of the isotherms,[31] the desorption illustrating the greater contrasts since differences in pore interconnectivity augments the size distinctions. We note that BJH pore size distributions can be unreliable for pores diameters smaller than 6 nm,[187] and other approaches exist to characterize smaller pores (e.g. DFT and Horvath-Kawazoe methods).[25, 153-154, 188] Pore sizes observed here for both adsorption and desorption are above this limit, however, and BJH analysis is expected to be reliable.

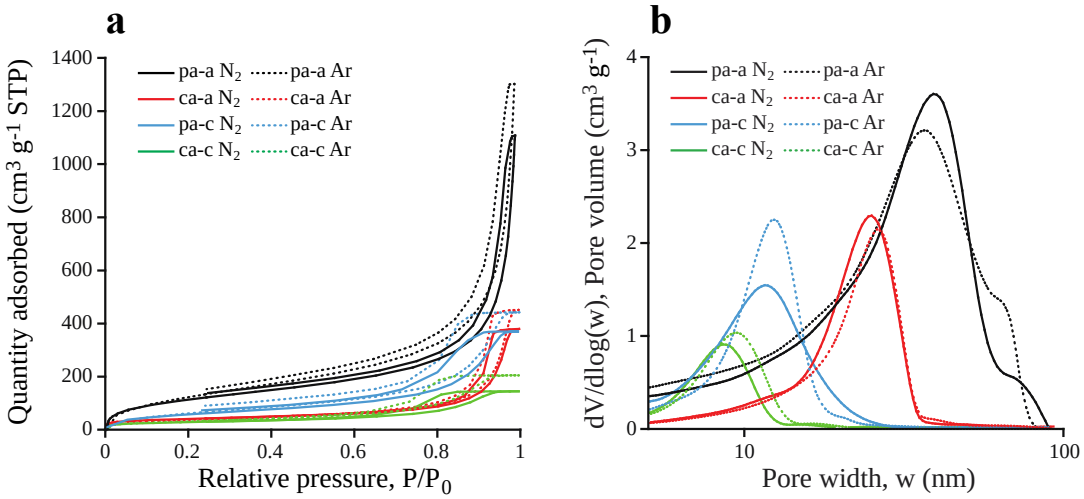

Fig. 4 Isotherms and BJH pore size distributions of **pa-c**, **pa-a**, **ca-c**, and **ca-a**. **a**: nitrogen sorption (continuous line) and argon sorption (dash line) isotherms of **pa-c**, **pa-a**, **ca-c**, and **ca-a**.

b: BJH pore size distributions of the nitrogen desorption (continuous line) and argon desorption (dash line) of the **pa-c**, **pa-a**, **ca-c**, and **ca-a**. Note, the pore width spans 6 to 100 nm, appropriate for the BJH analysis of these samples.

Total pore volumes and shapes of sorption isotherms of aerogels synthesized in cyclohexane are clearly different from those synthesized in acetone, regardless of adsorbate used or whether the sample was annealed or not. While all isotherms of Fig. 4a indicate a modest level of micropores and are characterized as Type IV(a) according to IUPAC nomenclature,[23] the broader hysteresis loop in the cyclohexane-derived aerogels differentiates them as Type H2(b), while the narrow, more vertical loop for aerogels synthesized in acetone accord most consistently with Type H1. In general, hysteresis loops of Type IV(a) are attributable to capillary condensation in the mesopore regime where the capillary window is of more variable dimension.[23] The H1-Type hysteresis can be ascribed best to materials whose porosity consists of a narrow range of mesopores where the neck of these pores is only slightly narrowed. Hysteresis of Type H2(b) appears in the isotherm of materials consisting of a greater differential in neck and pore size distributions. In applications this can result in not only a network or percolation effect, where transverse transport can be enhanced,[24] but also pore-blocking and, with processing such as annealing, cavitation or collapse.[23] We observe that isotherms of both **pa-c** and **pa-a** exhibit an open-ended hysteresis loop at about $p/p_0 \approx 0.22$. This may be attributable to micropore windows connected to mesopores, effectively producing transient pore blocking with slower diffusion kinetics, but perhaps more likely the open loop may be the consequence of the temperature- and window-dependent capillary evaporation from a receding meniscus (cf. SI).[189] Similar behavior has been observed in shale hydrocarbons,[190] which show low-pressure hysteresis (LPH).[191] The open-ended isotherms of **pa-c** and **pa-a** were observed

in a previous study from our group.[185] In contrast, both hysteresis loops of **ca-c** and **ca-a** isotherms are closed by $p/p_0 \approx 0.5$, presumably because the micropores collapsed during annealing.

Comparing the influence of solvent on the isotherms for the polymeric aerogels, we find that the total quantity of gas (either N_2 or Ar) adsorbed by **pa-a** is three times larger than by **pa-c**. This reflects, shown in Table 1, the larger total pore volume in **pa-a** (~1.8 $cm^3\ g^{-1}$) in comparison to **pa-c** (~ 0.6 $cm^3\ g^{-1}$), or alternatively the considerably lower density of **pa-a**. The changes in the BET "C" parameter support both greater amount of surface organic component in the polymeric aerogel, which apparently is not altered appreciably by the different solvents, and its loss on annealing.[192-194] The argon adsorption suggests there may be less organic lost by the aerogel prepared in acetone, surprising since its pores are larger than aerogel prepared in cyclohexane. The average SSA of **pa-a** (~ 439 m^2g^{-1}), which is attained consistently for both nitrogen and argon sorption data, is approximately twice as large as the SSA of **pa-c** (~ 218 $m^2\ g^{-1}$).

Clearly, the hysteresis distorts the pore size distribution as portrayed in Fig. 4b. For the classical model and from the experimental values in Table1, the ratios of pore volumes to pore areas, averaged over both adsorbates, would suggest the radii of the larger pores in **pa-a** could be expected to be only about 1.4 times those of **pa-c,** consistent with the area of **pa-a** being about twice that of **pa-c**. However, the ratio of the most probable pore radii indicated by the BJH analysis in Figure 3B is greater than 3. The BJH analysis of the hysteresis here overemphasizes the amount of the smaller pores in **pa-c**. So, while the trends for smaller size pores in the aerogels synthesized in cyclohexane, observed in the isotherms, are borne out, the quantitation is in question. This will be addressed further below when discussing the results of the DHS. Similar trends are observed when contrasting the data of the ceramic aerogels produced by annealing the samples from the

different solvents. The isotherms and hysteresis loops of **ca-a** and **ca-c** show consistent and proportional reductions in their properties: the amounts of adsorbed gas, pore sizes and distributions, total pore volumes and SSA's are reported in Table 1. Here, also, the ratios indicate the BJH analysis overestimates the ratio of pore radii of **ca-a** to **ca-c**, though the disparity is slightly reduced.

Sample	SSA N_2 ($m^2\,g^{-1}$)	SSA Ar ($m^2\,g^{-1}$)	BET C N_2	BET C Ar	TPV N_2 ($cm^3\,g^{-1}$)	TPV Ar ($cm^3\,g^{-1}$)	ρ (bulk) (g cm^{-3})
pa-c	219	217	47.1	29.0	0.61	0.57	0.7
ca-c	95	100	148.7	112.6	0.22	0.27	-
pa-a	414	463	47.3	28.0	1.7	1.7	0.3
ca-a	132	116	146.8	76.3	0.58	0.58	-

Table 1 BET-determined specific surface area (SSA) was computed from the adsorption at monolayer coverage, the value of Qm converted from cm^3g^{-1} at STP. The BET-determined unitless "C" parameter, computed from the isotherm transform, is a measure of adsorbate/adsorbent interaction. The total pore volume (TPV) was established from the maximum in the gas adsorption isotherm, assuming the fluid at P/P_0 of 1 is all liquid. These values for the SiCO aerogels were established from adsorption of nitrogen (at 77 K) and argon (at 87 K). The approximate bulk density in the last column is provided for comparison. Because of the fragility of **ca-a** and **ca-c**, their bulk densities were not evaluated.

3.3 Isotherm Scanning and DHS Analysis

Four sets of multiple high-resolution argon sorption isotherms are shown in Fig. 5 a-d. Each set of scans constitutes the Differential Hysteresis Scanning (DHS) experimental measurements for the sample indicated, decomposing each isotherm into fourteen component scans, the current maximum for the software. Each set serves as input for the DHS analysis, which employs a non-negative least-squares (NNLS) routine to carry out its deconvolution. The measured isotherm is effectively treated as a composite response for a collection of pores with a variety of geometries, such as suggested in Fig. 1.

The results of the DHS analysis may then be used to distinguish three core geometric classes of mesopores according to the relative dimensions of their pores and windows (bottlenecks): (i) non-restrictive pyramidal pores with a window size equivalent to or larger than the pore size ($d_{win} \geq d_{pore}$), (ii) constricted pores with a window smaller than the pore size ($d_{win} < d_{pore}$ and d_{win} is of mesopore dimension), and (iii) a third type, a special case of constricted pores, with essentially occluded pores in which a micropore window is much smaller than the pore size ($d_{win} \ll d_{pore}$, $d_{win} < 2$ nm). The relation between the diameter of the pore (d_{pore}) and diameter of its connected window (d_{win}) for the aerogels is plotted in two-dimensional (2D) contour plots in Figure 6. White lines segregate the 2D plane into regions corresponding to pyramidal, constricted, and occluded mesopores. As illustrated, sets of pores with the same ratio of pore to window diameters follow diagonals, and those sets of ratios defining the three types of regions occupy the designated areas. The region designating the pyramidal pores complies with a functional description in that, for large

pores with window diameters slightly narrower than the pores, their desorption will be little constrained by the modest narrowing.

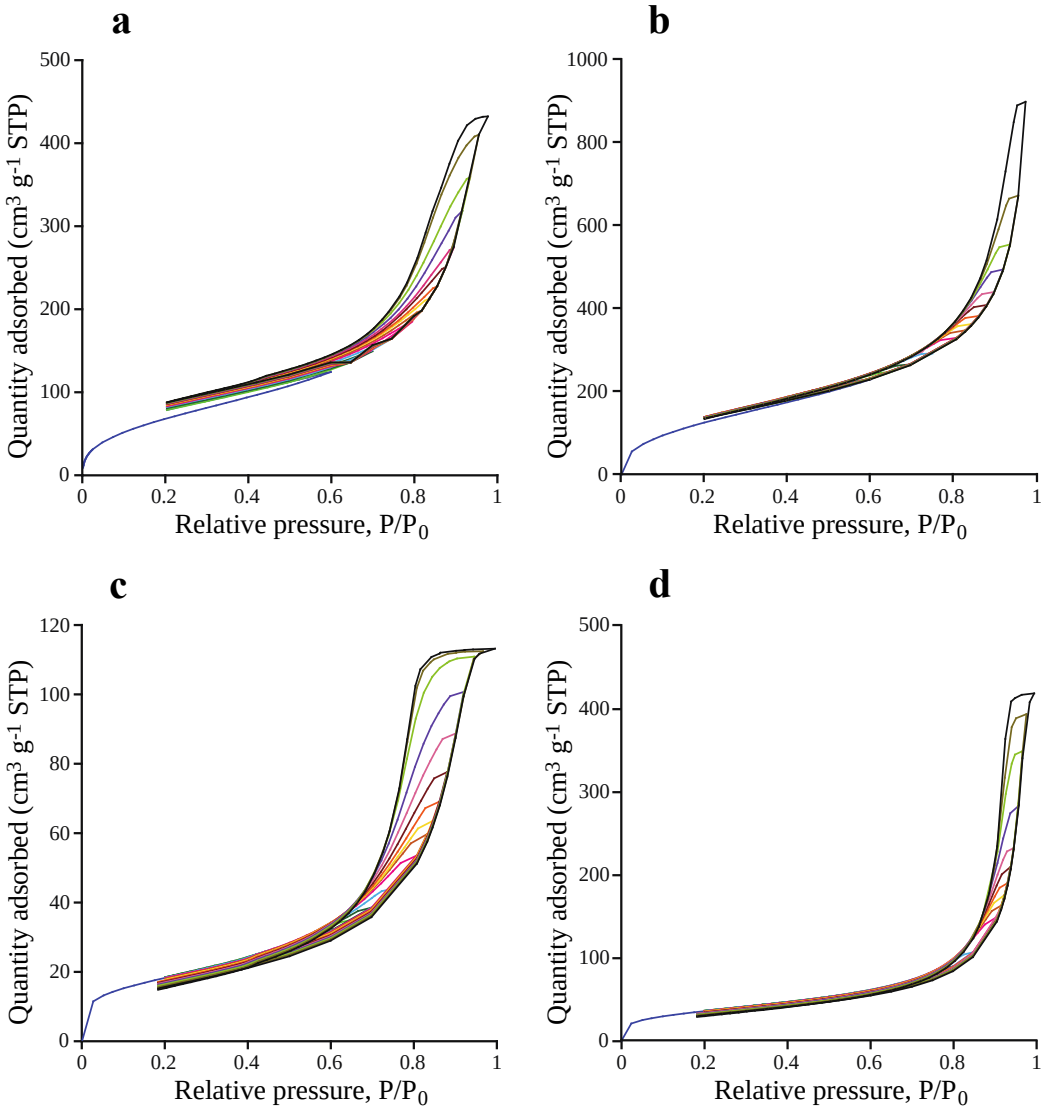

Fig. 5 DHS Ar sorption at 87 K; **a**. on **pa-c**; **b**. on **pa-a**; **c**. on **ca-c**; and **d**. on **ca-a**. The fourteen sorption scans for each sample are the input data for the corresponding DHS analysis provided in Fig. 6.

The software distinguishes three core geometric classes of mesopores according to the relative dimensions of their pores and windows (bottlenecks): (i) non-restrictive pyramidal pores with a

window size larger than the pore size ($d_{win} > d_{pore}$), (ii) constricted pores with a window smaller than the pore size ($d_{win} < d_{pore}$), and (iii) a third type, a special case of constricted pores, with essentially occluded pores in which a micropore window is much smaller than the pore size ($d_{win} \ll d_{pore}$, $d_{win} < 1$ nm). The relation between the diameter of the pore (d_{pore}) and diameter of its connected window (d_{win}) for the aerogels is plotted in two-dimensional (2D) contour plots in Figure 5. White lines segregate the 2D plane into regions corresponding to pyramidal, constricted, and occluded mesopores. As illustrated, sets of pores with the same ratio of pore to window diameters follow diagonals, and those sets of ratios defining the three types of regions occupy the designated areas. The region designating the pyramidal pores complies with a functional description in that, for large pores with window diameters slightly narrower than the pores, their desorption will be little constrained by the modest narrowing.

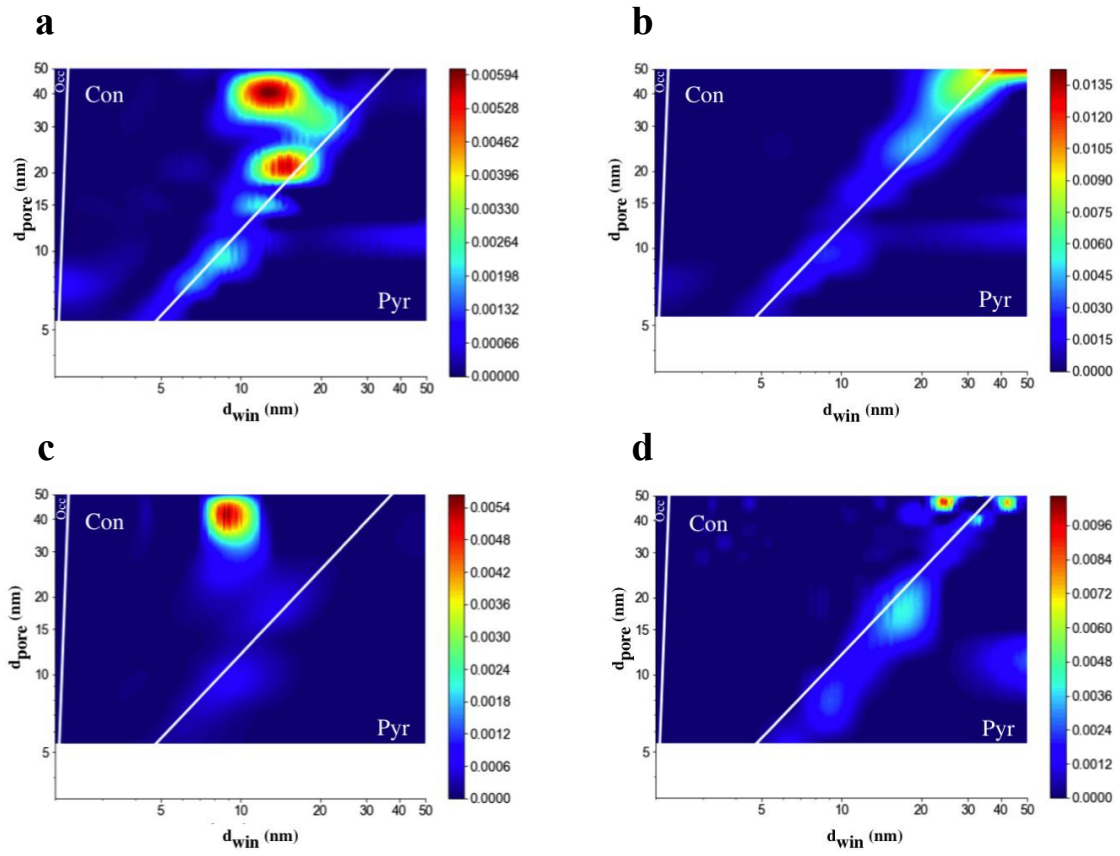

Fig. 6 Two-dimensional (2D) contour plots characterizing the relation between the diameter of the pore and that of its connected window derived via DHS from Ar sorption at 87 K. Polymeric aerogels are in the top row, **pa-c** (**a**), **pa-a** (**b**), and ceramic aerogels in the bottom row, **ca-c** (**c**) and **ca-a** (**d**). The color scale of each sample is normalized to its total mesopore volume. White lines split the 2D plane to into pyramidal (Pyr), constricted (Con), and occluded (Occ) mesopore areas.

Fig. 6 exhibits a striking difference between the relative pore and window diameters for the aerogels synthesized in cyclohexane before and after annealing, **pa-c** (Fig. 6a) and **ca-c** (Fig. 6c). Simply, before the annealing there is a bimodal distribution of pore sizes, at approximately a 2:1 ratio of pore sizes, each with approximately the same window dimension. After annealing the smaller pores have disappeared while the larger ones have remained about the same size, and the

window area contracted to just 36% of the original size. In detail, for **pa-c** prior to annealing we observe two strong maxima (indicated by red color) and three minor maxima, the latter in sum are but a small fraction of pores. One of the strong maxima is centered at a pore diameter of 41.4 nm with a pore window size of 13.2 nm, and the other, slightly less pronounced one, centered at 21.6 nm with a pore window size of 14.6 nm. Therefore, the DHS analysis reveals essentially a bimodal distribution of pore sizes. We emphasize that this bimodal distribution in pore size is not resolved in the BJH analysis of the original isotherm. Moreover, the DHS-derived pore diameters of 41.4 and 21.6 nm are appreciably larger than indicated by the peak at 12 nm found in the distribution derived from BJH analysis (see Fig. 4b). We had noted previously that quantitation of BJH pore sizes for **pa-c** is in question, as is common when hysteresis is significant — and the DHS data provides insight into this BJH overestimation of smaller pores. Analyzing the two strong maxima further, we find that the ratio of pore window diameter to pore diameter for the larger pores is 0.32, while that ratio for the smaller pores is 0.68. Hence, larger pores are considerably more restricted than smaller pores. Consequently, in Figure 5 the cohort with the larger pores is located further from the white diagonal, which represents the boundary between the constricted and pyramidal geometry.

DHS analysis of **ca-c**, the ceramic counterpart of **pa-c** annealed at 1000 °C, indicates just one strong maximum with average pore diameter of 43.2 nm and a pore window size of 9.1 nm. Thus, while the pore diameter for the larger pores changed only insignificantly, both the central window diameter and its range of diameters decreased considerably. The average window sizes were reduced from 14.6 nm to 9.1 by 30 %, the range in sizes from 5.8 nm to 3.3 nm even stronger, by 43%. The most surprising and notable change upon annealing, however, is the complete

"disappearance" of smaller pores. Because it is not clear whether these pores have collapsed completely or are just sufficiently occluded that there is effectively no adsorption, this effect is under current investigation. But clearly, the more vulnerable to collapse were those of smaller size.

The bimodal distribution itself is of interest since it has been reported to occur in analogous systems of tightly packed spheres, there for sol-gel systems. [19, 195-198] The occurrence has been attributed to intra- and inter-particulate pores. If that be the case here, it seems highly unlikely that both populations of pores should have windows of such similar size, unless they are in some way connected. Supposing that they are connected, then either the large pores or the small pores would be connected first to the window. Since, however, the small pores collapse on annealing, yet the large pores are still accessible, the only possibility is that the window is connected to the large pores first, that in turn are connected to the smaller pores. This picture is consistent with the synthetic procedure in which the particles grow, then agglomerate, with just a window opening onto the larger interparticle spaces, which in turn are connected to the intraparticle pores. As discussed further in the Supporting Information the pa-c samples before annealing appear to have a monomodal window distribution with a bimodal pore size distribution and following annealing monomodal window and pore distributions [cf. §1.3 Supporting Information].

In contrast to results obtained for the samples synthesized in cyclohexane, yet consistent with material having Type H1 isotherms that increase abruptly at high pressures, those synthesized in acetone, **pa-a** and **ca-a**, exhibit distributions skewed to large pore diameters. These sizes, anticipated from the BJH analysis in Fig. 4b, are in fact so large that the pore sizes appear to lie outside the range of the DHS analysis. There appears to be little evidence for constricted

geometries since most of the distributions lie on or near the line of equal pore and window dimensions. This is consistent with the observation of a large total pore volume, with correspondingly low density, and with the very narrow hysteresis loop. DHS analysis of **ca-a** shown in Fig. 6d does suggest, however, that annealing the sample may be generating some level of constriction.

A quantitative breakdown of the amount of the different types of pore geometries for the four materials investigated is provided in Table 2. The amount of each of these three types of pore are quantified in terms of adsorbed volume, in cm^3g^{-1} STP. The total mesopore volume of pores analyzed by the DHS composite hysteresis loop is the sum of these three types of mesopores. For each of the samples the predominant pore type is constricted. The most porous and least dense sample, **pa-a**, has the greatest volume of constricted mesopores. Approximately 56% of that volume is retained in **ca-a** obtained after annealing. The denser sample, **pa-c** produced in cyclohexane, has only 30% of the total mesopore volume of **pa-a**. This sample shows a remarkable loss in mesoporosity after annealing, with the major type of mesopore losing 92% of its volume. These quantitative evaluations reflect the observations based on the graphical analysis described above. [cf. §1.2 Supporting Information].

Sample	% Pyr	% Con	% Occ
pa-c	2.7	26.3	1.2
ca-c	0.4	2.0	0.2
pa-a	27.8	69.1	3.1
ca-a	10.7	38.4	4.7

Table 2. The percent of each pore type for all four preparations, quantified by the DHS software for each sample. The data are normalized to the total volume of porosity of **pa-a**, set to 100%. This provides an estimate of the relative amount of each type of mesopore across the set of samples. SI provides more detail.

4. Conclusions

To our knowledge, this investigation is the first application of Differential Hysteresis Scanning (DHS) porosimetry to assess pore geometry and connectivity in an amorphous aerogel. We have illustrated how DHS augments and complements the structural information from electron microscopy and more classical porosimetry, providing a fuller description of the range of prevailing structures and their hierarchical interconnections. The technology, in conjunction with other assessments, reveals the significant changes occurring in pore and surface characteristics resulting from modification of the kinetics and thermodynamics associated with the synthetic procedure and subsequent processing. Knowledge of the hierarchical structure can assist significantly in meeting the design requirements for diverse applications, notably in control of surface heterogeneity, localization, and sequential accessibility. Specifically, we have illustrated

how a simple change in solvent in the synthesis of an aerogel can result in a system with monomodal distribution both in pore diameters and in window diameters. Such uniformity is characteristic for crystalline systems, and is shown here to occur even in a non-crystalline amorphous aerogel. Materials of this kind will exhibit homogeneous conditions and confinement for molecules and should be valuable in applications ranging from catalysis to drug delivery.

Conflict of Interest

There are no conflicts to declare.

Acknowledgements

This work was supported by the National Science Foundation (NSF) through award CMMI-1634448 and through a Non-Academic Research Internship for Graduate Students (INTERN) for PT.

Supporting Information

Differential Hysteresis Scanning of Non-Templated Monomodal Amorphous Aerogels

Poroshat Taheri, John C. Lang, Jeffrey Kenvin and Peter Kroll[131]

Additional Observations

1.1 Hysteresis Loop Non-Closure

One of the features common to these unannealed SiCO materials (pa's) and their preparation, is their open-ended hysteresis loops, characterized in the Porosity portion of the Results section. There it was observed that the adsorption and desorption arms of the isotherm did not merge, even at a P/P_0 of 0.22.[144] A frequent explanation of this effect is entrapment of adsorbate in micropores or ultra-micropores.[145, 189] Here, for the four evaluations, with both nitrogen and argon as adsorbates, the t-plot assessment of microporosity showed negative intercepts and negligible microporosity. Another explanation for non-closure has been surface effects that slow the rate of adsorbate evaporation and equilibration. We explored this possibility by redetermining the nitrogen isotherm for pa-a, whose absolute difference in specific volumes was greater, using parameters that slowed the rate of data acquisition. The isotherm is shown in SI-Figure 1.

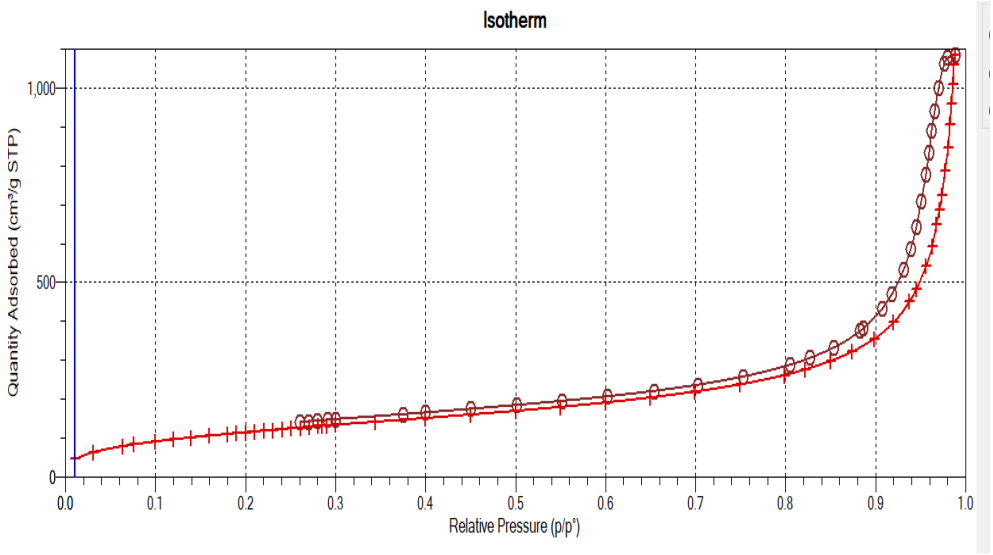

SI-Figure 1. Nitrogen **i**sotherm for **pa-a**, to be compared with the more rapidly acquired single isotherm in Figure 3A (solid line).

Both the equilibration intervals and equilibration delay times were increased significantly for this evaluation and the screen shot of these settings as specified in the ASAP 2020 system software as are shown in SI-Figure 2.

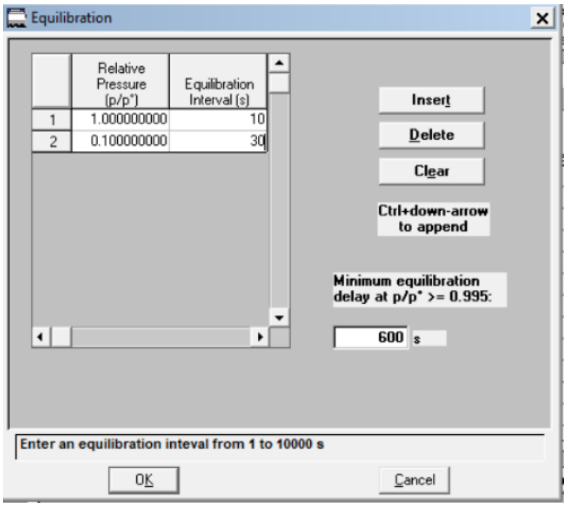

SI-Figure 2. Screen shot of the Equilibration window as it was specified under the Analysis Conditions in the ASAP 2020 software for the reanalysis of sample **pa-a**.

The isotherms shown in Fig. 3A and SI-Figure 1 are essentially indistinguishable. The non-closure was evaluated by selecting three points in the plateau regions for each isotherm, averaging the differences in specific volumes between the two arms of the isotherms, and evaluating their differences with a t-test that indicated there was only a 3% chance that the two isotherms are different.

We concluded that, at least by this measure, the kinetics of desorption were not the likely source of non-closure.

There are several other sources of non-closure, which as we indicated are common in this family of materials. From the BET C values listed in Table 1 it is readily apparent for the annealed ceramic samples, where there is complete closure, that significant increases in C have accompanied the annealing. Such transformations of surface energy could well influence the wetting behavior.[145] Abundant literature suggests this might well influence the openness between the two arms of the isotherm.[133] Additionally, it is well-known that annealing, while not melting the ceramic, can lead to "ripening" of the particles, an effect that will remove inherent roughness of the particulate aggregates. Both local energetics and wetting can be influenced, again with potential impact on the hysteresis closure.[199] Assessing surface roughness can be routinely investigated using scattering techniques,[200] and the characteristic evolution of structure accompanying sintering of porous xerogels serves as an example.[201-202]

These effects are topics of continuing research.

1.2 Relative Volumes

Simply, to distinguish the difference between the absolute shape-attributed specific volumes from the measurement from the relative values normalized with respect to the total pore **pa-a** provided in Table 2, we have included here in SI-Table 1 the Specific Volumes (in cm3 g-1 STP) reported by the DHS software, and in the last column their sum, the basis for the normalization.

SI-Table 1. Specific pore volumes attributed to the characteristic pore geometries for the four Si-CO's.

Sample	Specific Volume Pyr ($cm^3\ g^{-1}$)	Specific Volume Con ($cm^3\ g^{-1}$)	Specific Volume Occ ($cm^3\ g^{-1}$)	Sum
pa-c	0.048	0.472	0.022	0.542
ca-c	0.024	0.122	0.013	0.159
pa-a	0.274	0.682	0.031	0.987
ca-a	0.144	0.517	0.063	0.724

1.3 Pore Morphologies and Organization

In the discussion at the end of §3.3, following Figure 5, the appearance of the contour plots for sample pa-c led to the supposition that this bimodal distribution of pore geometries might be occurring through windows of the same size, and this could be interpreted to indicate both pore sizes share the same window. For clarification of the implications of this conjecture we have included a few figures to suggest constraints this might impose on the organization of the pores in the constituent particles, such as those reported in Figure 3. These organizational constraints are imposed by the observation that after annealing the larger pores are still accessible to adsorbate. The next figure, SI-Figure 3, provides colored representations of the two pore size distributions, simplified as blue for the large pores, and red for the smaller pores. The gray sheet represents the surface of the particles where the windows are located.

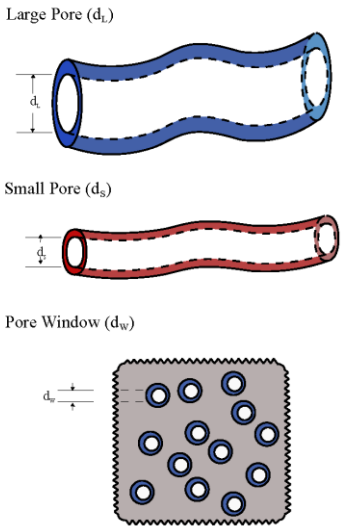

SI-Figure 3. Schematic representation of the pores comprising the bimodal distributions, with the larger blue pores having a diameter d_L, which in Figure 5 is centered at about 40 nm, and the smaller red pores having a diameter d_S, which in Figure 5 is centered at about 20 nm. In the Figure to the left the pore window with diameter designated d_W, which in Figure 5 is about 10 nm, is indicated to open onto only one size of pore.

The color coding in the second figure, SI-Figure 4, provides some suggestions of possible arrangements of the pores if the conjecture of a shared window is appropriate. In SI-Figures 4a and b there are three distinct regions: the outer surface **s**, the location of the window, a corona for the first layer, and a core. In both representations only one pore size occurs in an entire region. In 4a the corona is the large pore and the core the small pore; in 4b the sequence is reversed. In SI-Figure 4c, both large and small pores are occurring in both the corona and the core, hence the blended color. But even here there are constraints from the results following annealing and collapse of the small pores. To discuss these, one such acceptable organization is proposed in SI-Figure 4d.

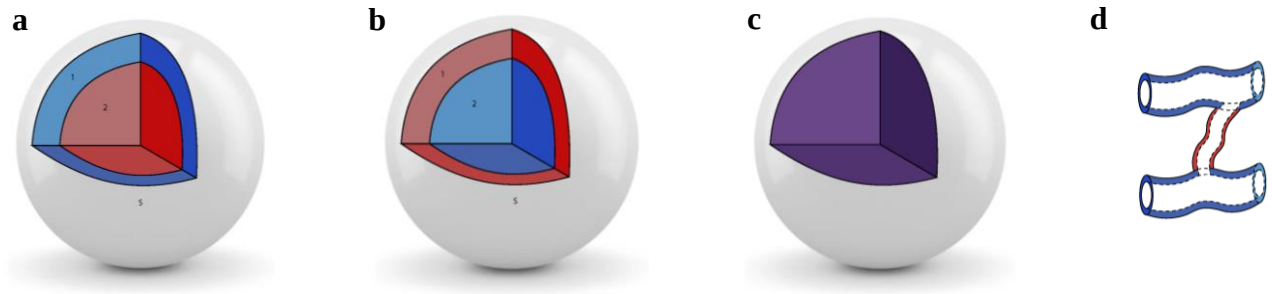

SI-Figure 4. Figures **a-c** are representations of the distinct particles shown in the SEMS of Figure 2. The "spheres" have an octant cut from the solid so that the composition of the interior can be explored. Possible arrangements are discussed in the following text. Figures **a** and **b** define three zones, s is the surface, 1 the outer region just inside the surface, and 2 the core inner

region. Figure **d**, based on the two pore types shown in SI-Figure 3, is simply suggestive of one arrangement, one with intersecting pores that would be consistent with the pattern of Figure **c**, with a uniform consistent pattern of pores throughout the interior of the particle. Here, as in SI-Figure 3, the windows are expected to be located on the surface of the particle.

Here we define these different types of configurations symbolically to facilitate discussion. Figures **a** and **b** in SI-Figure 4 are complementary, each have two **S**erial zones of segregated pores. In Figure a, the larger pores are restricted to the outer zone and the smaller, to the inner zone. This is configuration **S-1** with likelihood assigned as $\mathbf{F_1}$. In Figure b, the arrangement is reversed with the smaller pores restricted to the outer zone. This is configuration **S-2** with likelihood $\mathbf{F_2}$. Given the observation that on annealing the smaller pores are envisioned to collapse yet leave the large pores still accessible, arrangement **b** seems highly unlikely, whereas arrangement **a** seems quite acceptable, i.e., $\mathbf{F_1 >> F_2}$**.**

This brings us to arrangement c, the "homogeneous", single-zone depiction encompassing both large and small pores. Because of the number of possibilities that are consistent with such a uniformity we have summarized these in SI-Table 2.

SI-Table 2. Potential arrangements of large and small pores in the "homogeneous" region depicted in SI-Figure 4c. For the Parallel Configuration, Zones 1 and 2 correspond to their location in SI-Figures 4a and b that is as corona and core respectively, or for Figure **c** simply the sequential organization. For the Intersecting Configuration, Longitudinal and Transverse refer to paths nominally perpendicular to the surface or between two perpendicular pores , respectively. The transverse direction is suggested by the orientation of the smaller pore illustrated in SI-Figure 4d. The likelihood of these arrangements is suggested.

Configuration	Window	Zone 1	Zone 2	Likelihood
Parallel (P-1)	W_S	d_S	d_S	F_3
	W_L	d_L	d_L	
Intersecting		Longitudinal	Transverse	
I-1	W_S	d_S	d_L	F_4
I-2	W_L	d_L	d_S	F_5
I-3	W_L	d_L	d_L & d_S	F_6

From the arguments discussed above, F_2 and F_4 are highly unlikely, whereas conversely, F_1, F_5, and F_6 would appear to be more likely. While the parallel configuration is possible, such segregation during synthesis seems improbable. The ranking appears to be F_2 & $F_4 < F_3 < F_1 < F_5 < F_6$. The latter two are ranked simply based on the expectation that some of the intersecting crosslinks need not be exclusively the small pores.

By enumerating the network connectivity[195] taken to only a single tier of hierarchy for a simple bimodal distribution of pore sizes it is also clear why there might be little expected change in pore volume for the distribution of the larger pores. First, as suggested in Figure SI-4d, let there be just two types of pores, those connected to the surface ($\mathbf{P_s}$) and those interconnecting two pores ($\mathbf{P_c}$). For those connected to the surface, there are two options based on size, $\mathbf{P_s(L)}$ and $\mathbf{P_s(S)}$. For

the connections, there are three options, **P_s(L)**, **P_s(S)** and **P_s(O)**, where the latter indicates no interconnection. From assessing the assortment of **Ps** pairs and the variety of **Pc** interconnections, there are only nine sets of these primary pore types. Neglecting the differences in pore areas and volumes of these different types of pores, there are twenty-four appearances of pore locations. However, only one of the twelve affecting the large pores would reduce adsorption resulting from complete occlusion and collapse of the small pores.

CHAPTER IV: NOVEL SULFUR-CONTAINING CROSS-LININKG AGENT FOR SI-BASED PRECERAMIC POLYMERS

Poroshat Taheri, Bokka Apparoa, Parham Asgari, Junha Jeon, John C. Lang, Renzo Campostrini, Gian Domenico Sorarù and Peter Kroll

Published in: Macromolecular Chemistry and Physics (2020)[203]

Novel sulfur-containing cross-linking agent for Si-based preceramic polymers

Keywords: aerogel, hydrosilylation, sulfur, crosslinking agent

Abstract

Cross-linking polymethylhydrosiloxane (PMHS) with divinylthiophene (DVT) via hydrosilylation in highly dilute conditions and subsequent supercritical drying in CO_2 yields a polymeric aerogel containing aromatic sulfur integrally and uniformly distributed throughout the monolith. Fourier-

Transform Infrared (FT-IR) spectroscopy indicates almost complete consumption of vinyl groups and Si-H bonds in the product. Both FT-IR and Raman spectroscopic analyses support loss of conjugation of vinyl groups with the retained double bonds of the thiophene ring. Scanning Electron Microscopy (SEM) indicates a condensed colloidal structure with characteristic particulate diameters of about 165 nm. SEM coupled with Energy Dispersive X-Ray Spectroscopy (EDS) elemental mapping indicates that sulfur is distributed homogeneously in the polymeric aerogel. Porosimetry of the mesoporous aerogel indicates the effective average pore diameters are about 12 nm. Thermogravimetric Analysis (TGA) establishes greater thermal stability of the PMHS-DVT product than pure unreacted component. TGA coupled with Mass Spectrometric (TG-MS) identification of the volatiles released during pyrolysis has been used to characterize chemical processes occurring during calcination. The analysis suggests the identity of the bonds cleaved in the release of sulfur from the cross-linked polymer. Sulfur is driven from the system as thiophene and its derivatives. Recorded mass spectra support the hypothesis that cross-linking DVT bridges between PMHS chains in the polymeric aerogel, and that this results in a more thermally stable monolith.

Introduction

Catalytic hydrosilylation is one of the most important, efficient, and well-established reactions leading to organosilanes through addition of a Si-H bond across unsaturated bonds.[204-209] It is one of several approaches pursued in the polymer-to-ceramic conversion, for example, to cross-link and transform polysiloxanes into silicon oxycarbide (SiCO) ceramics[106, 210-213] Depending on processing, different morphologies of the ceramic, e.g., bulk,[214-215] foams,[216] and aerogels[213] can

be obtained. In particular, silicon oxycarbide aerogels are synthesized by a three-step sequence involving formation of a colloidal suspension, precipitation of the particles to form a colloidal gel, and super-critical drying (SCD).[217-218] Aerogels display many interesting properties including low bulk density (0.003–0.8 g/cm^3)[219] and high porosity with void fractions ranging from 80–99.8%, [53] all of which have made them appealing for applications.[68, 220-221]

Polymethylhydrosiloxane (PMHS, **1**) is a commercially available and inexpensive precursor that can be used in ceramic synthesis[117] (Scheme 1). Crosslinking to form a three-dimensional network prior to pyrolysis is requisite for stabilizing polymer-derived ceramics (PDCs). One approach is to transform Si-H moieties into Si-OH's that can undergo condensation concomitant with formation of a three-dimensional network.[117] In this study, a hydrosilylative cross-link method exploiting PMHS and olefins was used.[214, 222] While a variety of vinyl containing cross-linkers have been exploited previously, for example, divinylbenzene (DVB),[213-214] 2,4,6,8-tetravinylcyclotetrasiloxane (TMTV),[213] 1,3,5,7-tetramethyl-1,3,5,7-tetravinylcycletetrasiloxane (D4Vi),[210-211, 223] and vinyl terminated polydimethylsiloxane (PDMS),[86] the application of a sulfur-containing, two-fold vinyl donor, divinylthiophene, (DVT) (**2**) has not been investigated. In this report, we describe synthesis of the new polymeric PMHS-DVT (**3**) aerogel through cross-linking of PMHS (**1**) with divinylthiophene (DVT) (**2**) and subsequent supercritical drying, and its response to pyrolysis.

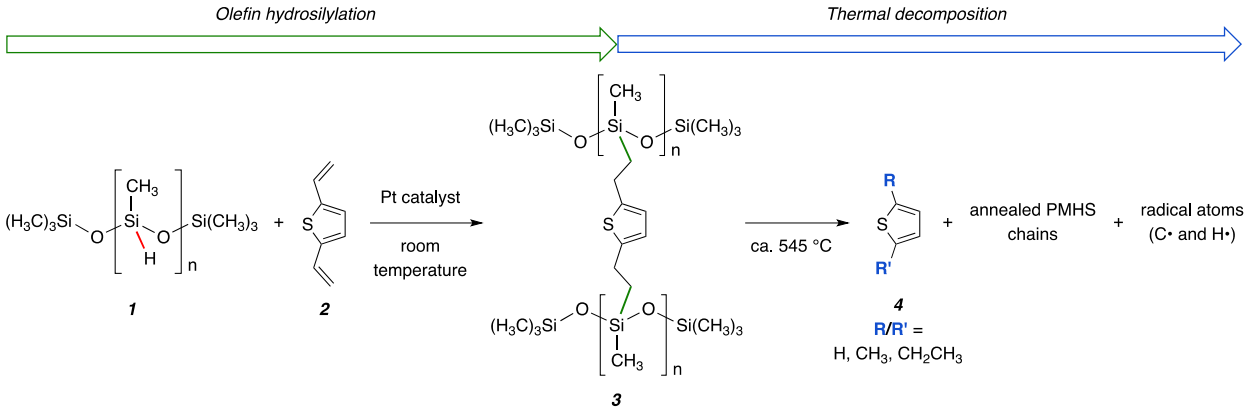

Scheme 1. Proposed hydrosilylation reaction between PMHS (**1**) and DVT (**2**) forming cross-linked PMHS-DVT (**3**) at room temperature. At higher temperatures (here depicted for 545 °C, see text), thermal decomposition occurs yielding multiple derived thiophene compounds (see Table 1).

Experimental Section

Synthesis of 2,5-divinylthiophene:[224] A flame-dried 100 mL round-bottom flask equipped with a stir bar was charged with 2,5-dibromothiophene (12 mmol, 2.9 g), palladium(II) chloride (0.16 mmol, 28 mg), potassium vinyltrifluoroborate (9.6 mmol, 1.3 g), and triphenylphosphine (.48 mmol, 126 mg). After the flask was purged with nitrogen for 30 min, dry, distilled tetrahydrofuran (36 mL, 0.3 M) was added to the mixture via a 50 mL glass syringe, and was stirred for 30 min. Cesium carbonate (60 mmol, 19.5 g) was added to the mixture and the flask was sealed with a septum. Degassed DI water (2.4 mL) was added to the mixture, and the reaction mixture was warmed to 85 °C (bath temperature) for 24 h. The progress of the reaction was monitored by GC-MS spectrometry. The reaction mixture was diluted with dichloromethane and rinsed with water. The organic phase was evaporated and concentrated under reduced pressure, and the divinyl thiophene purified with medium pressure liquid chromatography (MPLC). The MPLC was run

using hand-packed columns of silica gel (20−45 μm, spherical, 70 Å pore size), an HPLC pump, a differential refractive index detector, and a mobile phase of hexanes. The purification yielded divinylthiophene at a 60% yield (0.98 g).

Preparation of the aerogel: Polymethylhydrosiloxane (MW~1900, CAS: 63148-57-2) was purchased from Sigma-Aldrich and used as received. We prepared a mixture of PMHS and DVT adding 0.25 g PMHS and 0.5 g DVT in 90 vol% of acetone (Macron Fine Chemicals (CAS: 67-64-1)). These parameters yield approximately a 1:2 ratio of Si–H groups and vinyl (Vy) moieties. After stirring for 5 min, we added 10 μL of Karstedt's catalyst[225] (platinum divinylmethylsiloxane complex, ~2% in xylene (CAS: 68478-92-2); Sigma Aldrich) to the solution. The solution was stirred at room temperature for 2 days, after which its viscosity had changed noticeably, indicating that the solution was close to its gelation point. The stirrer was removed, and the solution was left standing. On the third day, the solution had transformed completely into a yellow transparent wet gel (Figure 1, left). The wet gel was washed with acetone 5 times. Subsequently, the gel was transferred into a home-built CO_2-reactor and washed 10 times with liquid CO_2. In every wash, the chamber was filled with fresh CO_2 and left standing for 6 hours for solvents to exchange. Finally, supercritical CO_2 was removed on lowering the pressure, leaving a dried aerogel (Figure 1, right). The mass of the wet gel was 2.14 g from which 0.23 g of dried aerogel was isolated. The aerogel was transferred to a sealed vial, which was stored in a vacuum desiccator.

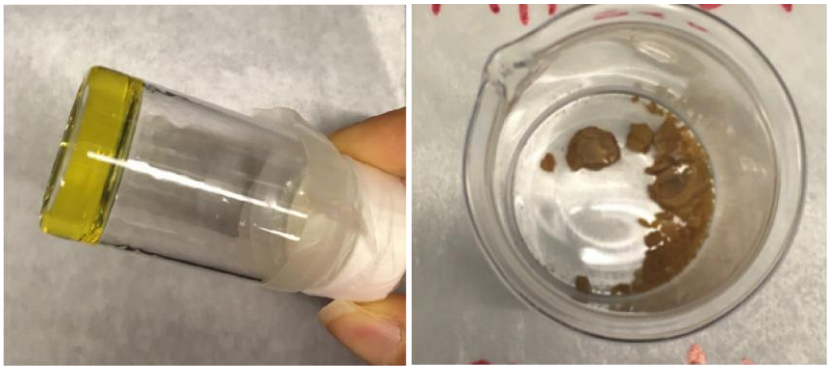

Figure 1. PMHS-DVT yellow wet gel obtained after 3 days, shown as a band at the bottom of the inverted vial (left) and the dark brown, fragile polymeric aerogel particles obtained after supercritical removal of CO_2 (right).

FT-IR spectroscopy: The FTIR measurements were made on a Bruker Alpha FTIR Spectrometer, using an Eco-Attenuated Total Reflection (ATR) cell equipped with a high refractive index Ge crystal, cleaned with acetone between runs. We investigated about 2-3 mg of DVT, 2-3 mg of PMHS-DVT product, and 1-2 drops of PMHS, serially. To obtain the spectra at a resolution of 4 cm^{-1}, 32 scans were taken with the interferometer mirror speed of 2.8 mm/s, and a room temperature stabilized detector (DLATGS) covering mid-infrared regions in the range of 650 – 4000 cm-1 were used. OPUS software (Bruker Inc.) was used for processing the experimental spectra.

Raman spectroscopy: About 0.5 g of DVT was placed inside the Thermo Fisher Scientific DXR Raman microscope. We selected 780 nm laser source with the laser power set at 10 mW on the sample. The reported accumulated spectra were obtained from 20 serial acquisitions, with a time of 10 seconds per acquisition. Raman spectra were collected over a spectral range of 50–3500

cm^{-1}. We used OMNIC 8 software (Thermo Fisher Scientific Inc.) for processing the experimental Raman spectrum of DVT.

Thermogravimetric analysis: A first TGA was carried out on a Shimadzu TGA-51 Thermogravimetric Analyzer. 3 mg of DVT, 7.5 mg of pure and uncross-linked PMHS, and 7 mg of polymeric PMHS-DVT aerogel, separately, were heated at 5 °C/ min from room temperature to 900 °C in a platinum pan under nitrogen atmosphere.

Combined Thermogravimetric & MS analysis: Additional Thermogravimetric (TGA) and Differential Thermal Analyses (DTA) were performed on a *LabSys Setaram* thermobalance, operating in the range 20-1000 °C. Measurements were carried out following purging the thermobalance furnace with He (99.999% purity) at a constant flow of 120 $cm^3 \cdot min^{-1}$, measured at 20 °C and 0.1 MPa by means of a *Matheson* mass flow controller. We poured 15.4 mg of course powders into an alumina crucible (volume 0.1 cm^3) and used a standard amount of α-Al_2O_3 (21.8 mg) as a reference. For this thermal analysis we applied a more rapid heating rate of 10 °C/min. The volatiles were analyzed using a VG TRIO-1 quadrupole mass spectrometer detector (QMD). The furnace of the thermobalance was connected with the ionization chamber of the mass-spectrometer through a customized transfer line made with an empty and deactivated-silica capillary-column (0.32 mm internal diameter, 13.5 m length) enveloped in a thermostatic jacket heated at 140 °C. During the thermal analyses, an appropriate fraction of the purging He flux, sampled the headspace a few millimeters above the sample-crucible, was continuously withdrawn and analyzed. Electron impact mass spectra (70 eV) of positively charged fragment ions were recorded with frequency of 1 scan s^{-1} in the 5–400 Da range (ionization chamber temperature 180

°C). MS data provided both the total ion current (TIC) and the single contributions of any *m/z* ion current (IC) as a function of time. Since temperature increased linearly with time, this analysis provided the mass spectra as a function of temperature. H_2 evolution was not recorded by MS due to the low sensitivity for *m/z* below 4.

SEM characterization: We selected a single piece of the aerogel, about 1 mm in each dimension, and mounted it on carbon tape adherent to an aluminum sample holder. Due to the low electrical conductivity of the sample, we coated it with silver (CrC-100 Sputtering System) (Plasma Sciences Inc, Ooltewah, TN). Microstructures and surface morphologies were examined in a scanning electron microscope (SEM) (Hitachi S-4800 II FE SEM) with an electron beam voltage of 20 kV and current of 15 μA. We used the ImageJ[226] software to screen samples and measured 40 individual particles in SEM micrographs.

EDS characterization: Elemental analysis of PMHS-DVT aerogel was performed by Energy Dispersive Spectroscopy in conjunction with Scanning Electron Microscope (Hitachi S-3000N Variable Pressure SEM). The sample was ground with mortar and pestle to a fine powder that was placed on the sample holder without coating. Elemental mapping at the microstructural level was performed at 1000 magnitude and 20.0 kV acceleration voltage and 15 □A emission current. EDS compositional mapping was performed within 60 min with the image resolution of 512 pixels by 384 pixels and map resolution of 256 pixels by 192 pixels and map pixel size of 0.26 μm.

Porosity: Nitrogen adsorption-desorption isotherms were measured at the boiling point of nitrogen, approximately 77 K, using a Micromeritics ASAP 2020 porosimeter. The sample of PMHS-DVT aerogel (Figure 1) was placed into a sample tube and degassed at 90 °C for 24 hours.

Nitrogen specific surface area was derived from a BET (Brunauer, Emmet, and Teller)[12] analysis of adsorption in the linear p/p^0 range of about 0.05-0.30. The specific surface area, pore volume, and pore size distributions of the aerogel were determined using Barrett-Joyner-Halenda (BJH)[31] analysis of the desorption branch of the isotherm in the p/p^0 range from about 0.95 to 0.25.

Results and Discussion

FT-IR and Raman Spectroscopy

Figure 2 shows FT-IR vibrational spectra of reactants, PMHS and DVT, and of the polymeric aerogel received after supercritical drying. PMHS displays characteristic Si-H (2162 cm^{-1}) and Si-CH_3 (1259 cm^{-1}) stretching vibrations.[227] DVT shows strong peaks at 3044 and 3087 cm^{-1} that are characteristic for C-H vibrations of conjugated, (sp^2-like) C atoms, i.e., as conjugated vinyl groups of slightly diminished frequencies.[228] NMR data can be found in the BioRad database, [229] but we did not find precedence of FT-IR of DVT in the literature. However, reported FT-IR spectra of thiophene or polythiophene show that the thiophene ring's characteristic absorption peaks such as bending vibration of in-plane C=C-H exist in both DVT and PMHS-DVT at 1409 and 1466 cm^{-1} peaks[230].

Comparing the FT-IR spectra of reactants with that of the product we notice major changes. First, the C-H vibrational characteristics for vinyl groups[228] (wave numbers above 3000 cm^{-1}) vanished, while those bands just below 3000 cm^{-1}, as typical for aliphatic C-H vibration, remained. Second, the strong Si-H peak (2157 cm^{-1}) almost completely disappeared. These two observations provide major support for the successful olefin hydrosilylation reaction of **1** with **2**, in which the Si-H functional group reacts with the C=C bond. The residual, small yet noticeable, Si-H peak

indicates a minor amount of unreacted Si-H moieties in the product. Third, two peaks located at 1409 and 1475 cm^{-1} in the spectrum of DVT represent C=C-H ["sp^2-like"] in-plane bending modes of double bonds of both vinyl groups and the thiophene ring.[230] The FT-IR spectrum of the PMHS-DVT aerogel product, on the other side, exhibits only a single peak at 1466 cm^{-1} representing these C=C-H in-plane bending modes. This mode also appears at 1469 cm^{-1} in the Raman spectrum[231] and implies that the cross-linking was accompanied by the loss of the vinyl groups of **2**, and only double bonds related to the thiophene ring retained their active C=C-H in-plane bending modes. These are slightly shifted towards higher frequencies due to the loss of conjugation (blue shift effect[228]).

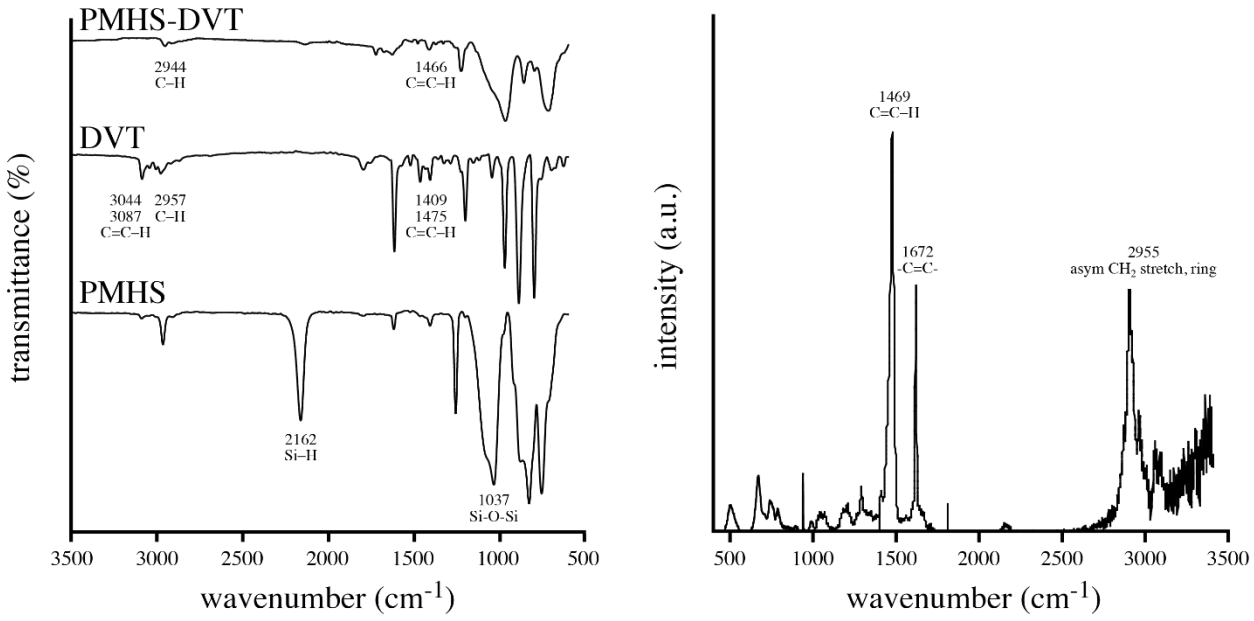

Figure 2. FT-IR spectra of PMHS, DVT, and PMHS-DVT (left) and Raman spectrum of PMHS-DVT (right). [Be nice to have the Raman of thiophene & DVT … there should be a diagnostic sulfur shifted peak around 400-500 cm^{-1}.]

Scanning Electron Microscopy / Energy Dispersive X-Ray Spectroscopy

We further characterized the dried polymeric aerogel using Scanning Electron Microscopy (SEM) combined with Energy Dispersive X-Ray Spectroscopy (EDS). Electron micrographs at different magnification are shown in Figure 3. The aerogel microstructure can be described as a loose agglomeration of spheroidal nanoparticles whose average size is 165 ± 22 nm.

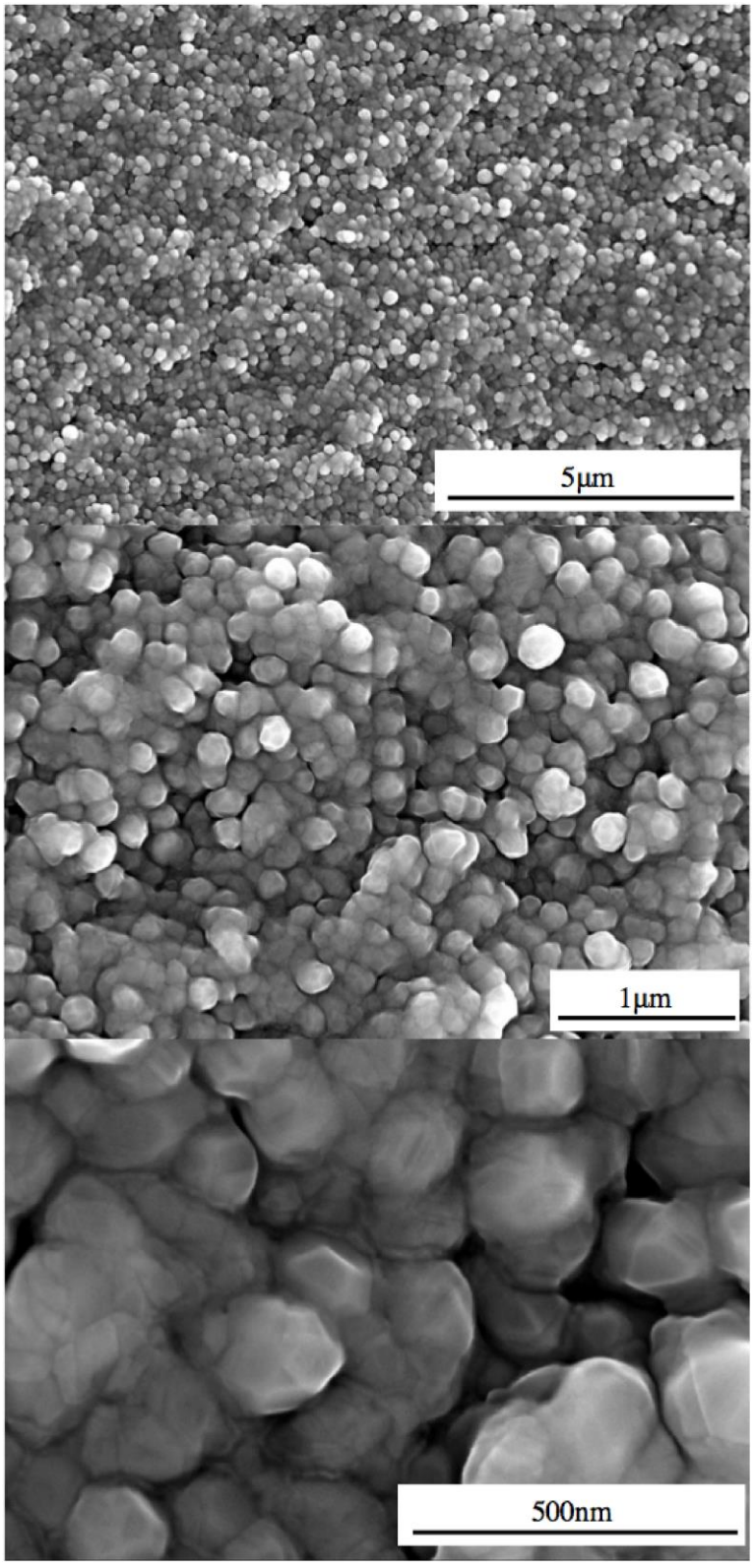
5µm
1µm
500nm

Figure 3. SEM micrographs of polymeric PMHS-DVT aerogel at different resolutions.

Elemental analysis performed using EDS is shown in Figure 4. The result confirms the presence of sulfur in the product. The semi-quantitative analysis of EDS has some limitations for light elements (Z<11) located in complex matrices where correction factors must be applied.[232] Taking these factors into account, we obtain a value of 1.8:1 for the atomic ratio of Si to S. For an ideal PMHS-DVT (**3**) polymer, when each DVT bridges between two Si (double-anchored), the nominal value is 2:1. A lower ratio may occur, if some DVT units are only single-anchored to Si. Figure 5 shows elemental mapping analysis within the EDS. Within the resolution of the method (pixel size of 0.26 μm) we find no clustering of sulfur, but uniform distribution of sulfur throughout the sample.

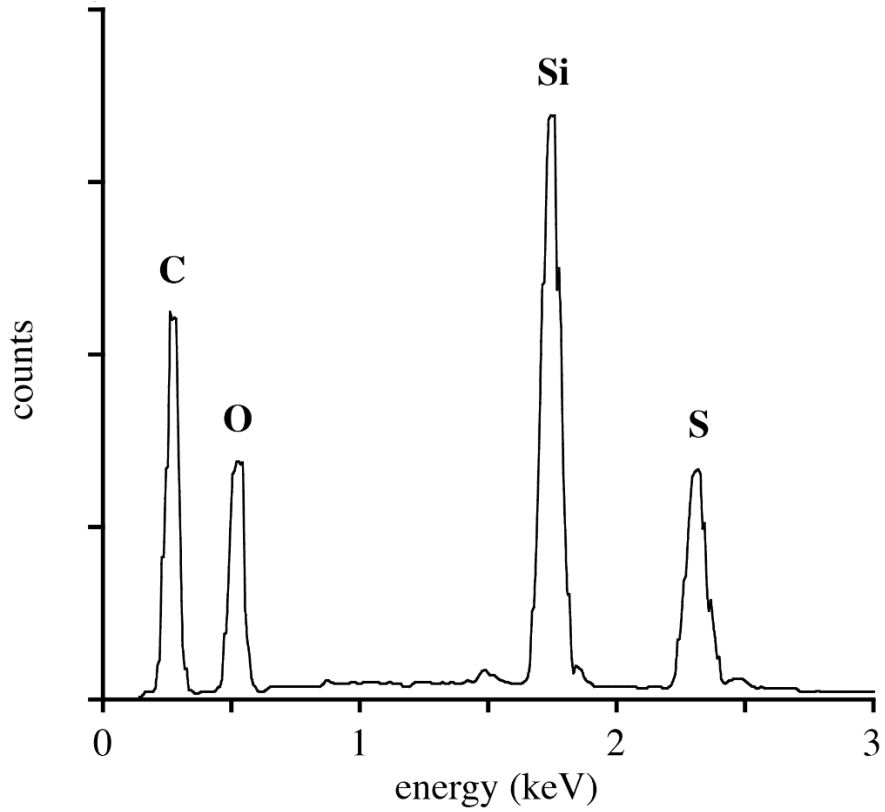

Figure 4. EDS analysis of polymeric PMHS-DVT aerogel.

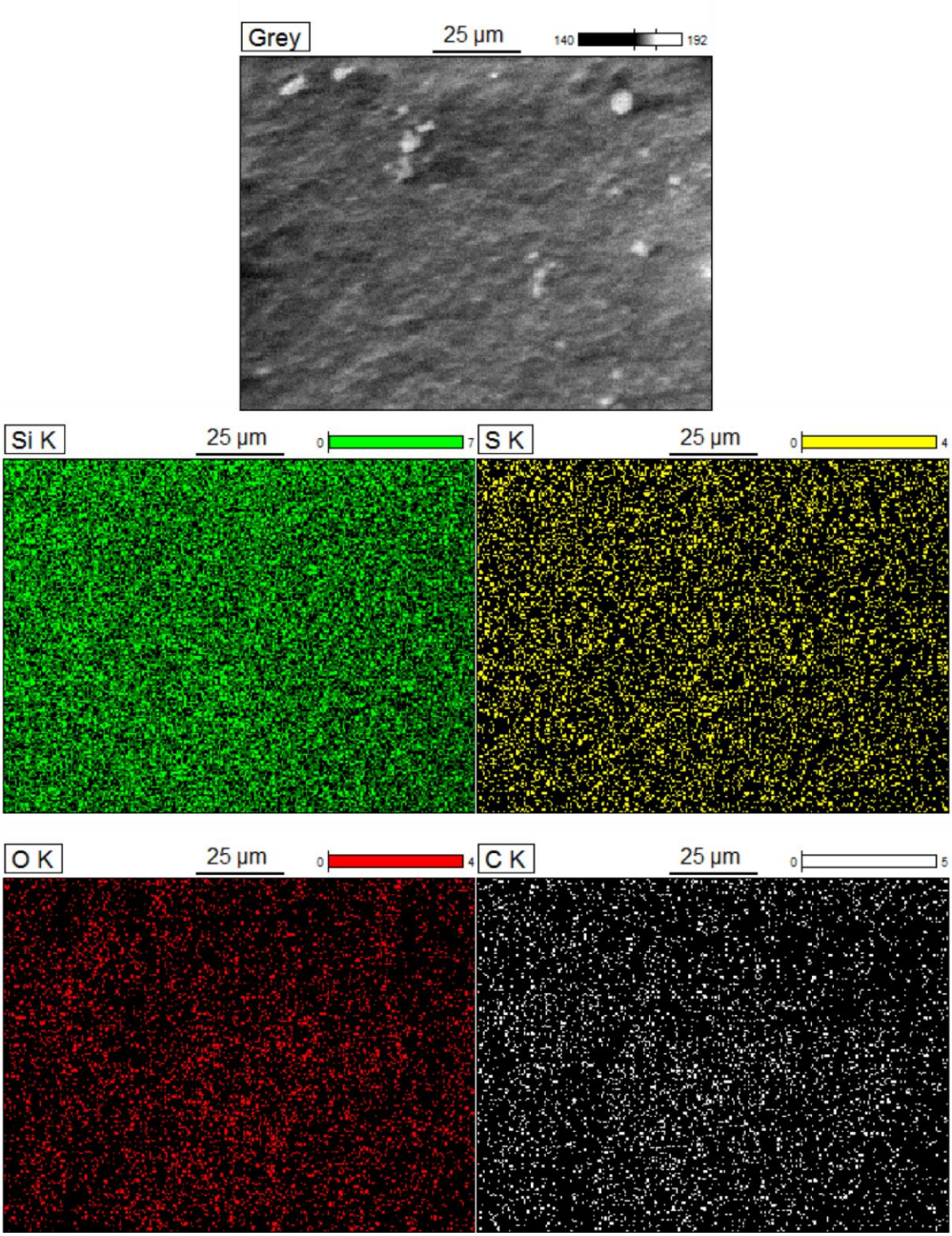
Grey
25 µm
140
192
Si K
25 µm
0
7
S K
25 µm
0
4
O K
25 µm
0
4
C K
25 µm
0
5

Figure 5. EDS compositional mapping of polymeric PMHS-DVT aerogel. The individual pixels correspond to areas with a width of 0.26 μm length.

Porosity Analysis

The nitrogen adsorption-desorption isotherm at 77 K of the polymeric PMHS-DVT aerogel is shown in Figure 6 (left). The shape of the isotherm corresponds to a Type V of the IUPAC classification,[18] consistent with relatively weak adsorbent-adsorbate interactions and the initial clustering of adsorbed molecules with one another at nucleation sites on the surface of a nonporous or macroporous solid. These sites gradually thicken until a multilayer film of liquid forms, filling the relatively few small pores. As p/p^o increases above 0.3 the larger pores with greater polydispersity fill until the entire surface is covered with a liquid layer as p/p^o approaches 1. In contrast, many other polysiloxane aerogels display isotherms of Type IV,[176, 213, 233-234] with greater adsorption to the solid and smaller pores.

The desorption arm of the hysteresis curve shown in Figure 6 corresponds to the generic type H2b shape,[18] characteristic of pores having a distribution of sizes and geometries (e.g., small necks and wide bodies with substantial variation of diameters, such as those observed in silica gels and modelled mathematically[18]). Observed pore-sizes, deduced from the desorption branch of the isotherm, range between 5 and 25 nm with a maximum at 15 nm (Figure 6). The BET specific surface area (SSA) of the product is 43 m^2/g, and corresponds with the predominance of mesopores, 2-50 nm in diameter, and low porosity. This is significantly smaller than SSA's found of other polymeric siloxane aerogels, for which values between 100 and 1000 m^2/g are reported,

and depends on nanoparticle size, packing, and pore characteristics, such as size and density. [213, 220, 235]. The total pore volume (TPV) is only 0.23 cm^3/g, and the average pore diameter is 12 nm.

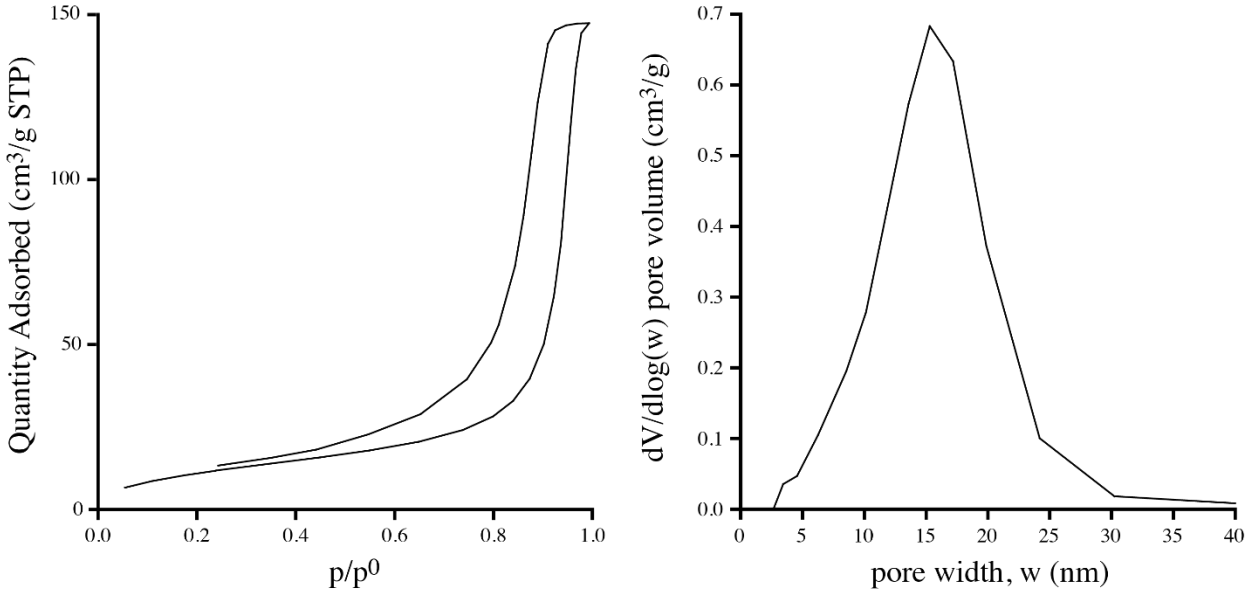

Figure 6. Nitrogen sorption isotherms (left) and pore size distribution (right) of PMHS-DVT following supercritical drying.

Thermogravimetric Analysis

The initial TG characterization of the polymeric PMHS-DVT aerogel is shown in Figure 7. For comparison, we have included TG results for both reactants, PMHS and DVT, obtained through similar experiments. The cross-linked polymeric aerogel underwent a total mass loss of only 34% after heating to 900 °C. This is less than either pure PMHS (40.5%) or pure DVT (91.2%). Assuming a simple mixture of unreacted PMHS and DVT in mass ratio 1:2, a mass loss of about 74% might be expected for a simple mixture of unreacted components. Derivatives of the mass loss curves are included in Figure 7. For the polymeric aerogel, the derivative indicates a range of

high mass loss from 380 °C to 520 °C with a maximum at 450 °C. This behavior is characteristic for PMHS cross-linked with either tetramethyl-tetravinyl-cyclotetrasiloxane (TMTV) or 1,3,5-triallyl-1,3,5-triazine-2,4,6 (1*H*,3*H*,5*H*)-trione (TTT). [176, 236] In comparison to the derivatives of mass loss for pure DVT and PMHS with maxima at 404 °C and 402 °C, respectively, the polymeric PMHS-DVT aerogel shows greater thermal stability with mass loss shifted by 50 °C towards higher temperatures. This indicated the thermal stability of the PMHS-DVT aerogel is enhanced by its cross-linking network.

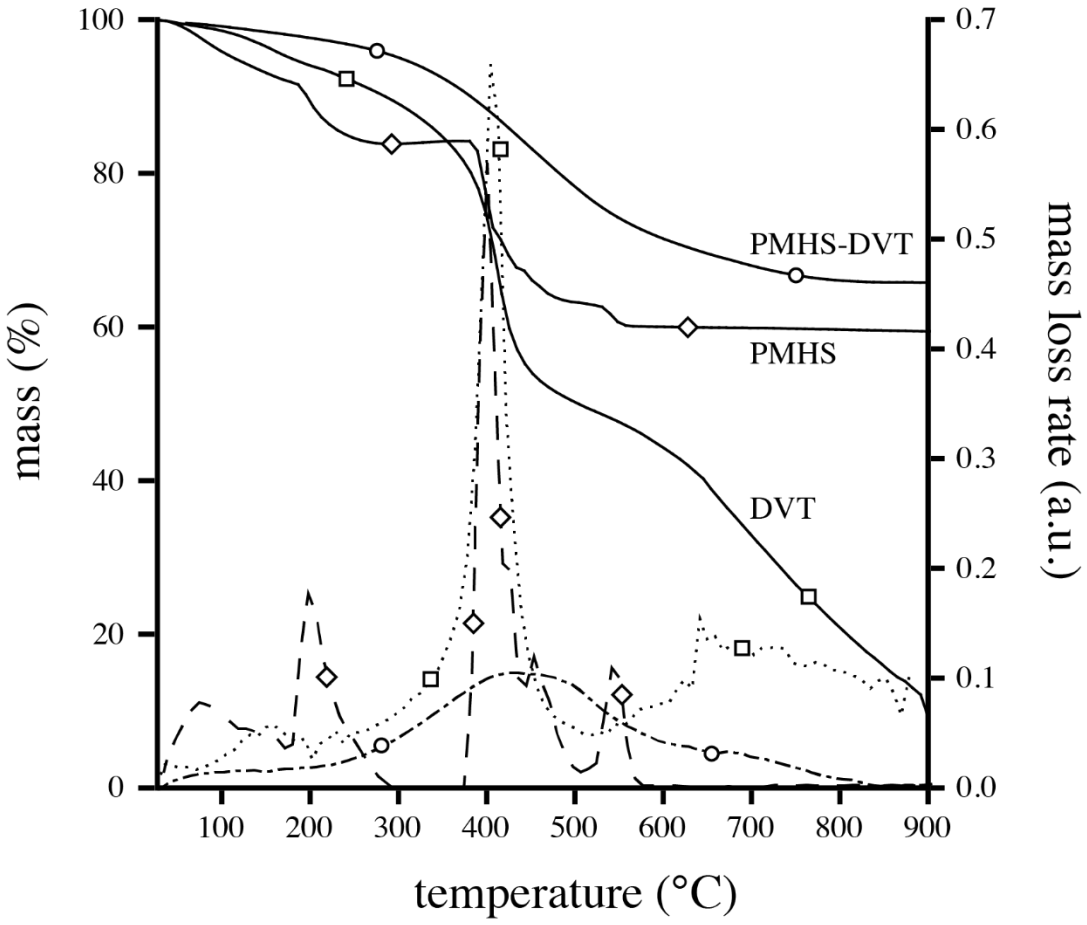

Figure 7. TGA analysis of reactants (DVT, PMHS and polymeric PMHS-DVT aerogel product from the room temperature to 900 °C using a heating rate of 5 °C/min. Solid lines are for the TG signal (left ordinate) of pure DVT (indicated by square symbol), pure PMHS (diamond), and

polymeric PMHS-DVT aerogel (circle). The derivatives (right ordinate) of each TG curve are shown as well for pure DVT (dotted line; square symbol), pure PMHS (dashed line; diamond), and polymeric PMHS-DVT aerogel (dashed-dotted; circle).

Thermogravimetric Analysis coupled with Mass Spectroscopy of evolved gases (TG-MS)

In a second thermogravimetric analysis, we recorded TG together with simultaneous Mass Spectrometry (TG-MS) to analyze the evolved gas-phase during the polymer-to-ceramic transformation of the polymeric PHMS-DVT aerogel in detail. TG and its derivative, DTG, signals as well as Total Ion Current (TIC) are shown in Figure 8. The TG curve shows a total weight loss of 37% (room temperature up to 1000 °C), which agrees with the earlier analysis obtained using different TG equipment. The progressive and continuous mass loss is largest between 300 and 700 °C, with the DTG signal showing two pronounced minima at 417 and 487 °C. This is not inconsistent with the initial TG experiment, given that in this study we used a higher heating rate, 10 °C/min versus 5 °C/min used previously. The TIC signal indicates four overlapping thermal-decomposition events centered at 157, 396, 545, and 697 °C.

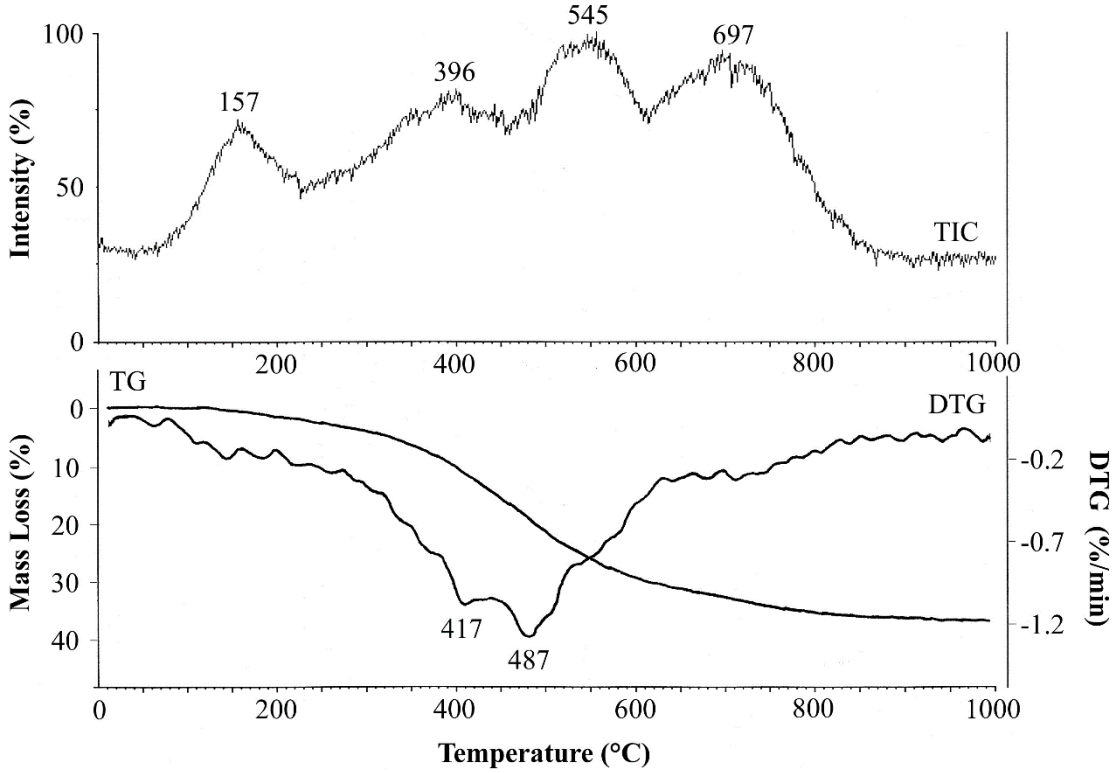

Figure 8. Total Ion Current (TIC) as a function of pyrolysis temperature (top) and TG/DTG curves recorded during pyrolysis of the PMHS/DVT aerogel (bottom).

The first thermogravimetric event occurs in the temperature range between 80 and 230 °C and can be attributed to an evolution of H_2O and, to lesser amount, organic compounds with low molecular mass. The release of water is readily monitored by the curve of its molecular ion current (IC *m/z*=18) (see graph for *m/z*=18 in Figure 9, lowest frame on the left, and lowest curve on the right). Appearance of loosely bound water, evolving with peak at 157 °C, is likely a consequence of preparation and handling of the polymeric aerogel. Si–H moieties present in the PMHS polymer

can undergo oxidation with atmospheric moisture in the presence of metal catalyst to afford silanol (Si-OH).[237] Such silanol groups will condense in the early stages of annealing and release H_2O. Probably, the small organic counterpart is introduced in the system through the Pt catalyst solution.

Skipping the second and third thermogravimetric events for a moment, we found that the fourth and last thermogravimetric events, approximately in a range of 610 to 840 °C, originated from the release of methane only (see graph for *m/z*=16 in Figure 9, right). Indeed, in this temperature range, Si–CH_3 and any residual Si–H moieties can react to yield new Si–CH_2–Si bridges and gaseous CH_4 and H_2..[238-241] As stated in the method section, H_2 evolution is not monitored by the MS due to the low sensitivity of our equipment for *m/z* signals below 4.

The second decomposition step is associated to the broad peak in the TIC between 230 °C and 450 °C range with a maximum at 396 °C. The mass spectrum recorded at 396 °C reveals a vast array of *m/z* signals up to 98 Da, with more intense signals (in decreasing order) at 28, 18, 15, 16, 44, 45, 27, 43, 29, 39, 75, and 97 Da (Figure S2). A more detailed characterization will require additional gas-chromatographic separation of the gaseous mixture.[238] We infer, however, that the most abundant gaseous species are methyl units and lower molecular weight hydrocarbons derived from thermal decomposition of the cross-linking agent DVT rather than from the methyl siloxane (PMHS) counterpart. For one, it is well known that Si–O siloxane networks are quite stable at those temperatures.[238, 242] Secondly, species such as silane or methyl-derived silanes with *m/z* =46, 60, 74, 88 yield pronounced signals at *m/z* = 31, 45, 73 and 73, respectively. This was characterized previously through the isotopic tail of Si-atoms.[238] Since those were not present in the recorded MS spectra at the temperature, we can exclude that Si-based species evolved at this stage. The very small amounts for fragments at and above 75 Da could be thiophene-derived.

The third decomposition event, which is the most intense one in the TIC plot, occurred between 450 and 610 °C. An extensive analysis is provided in the Supporting Information. The mass spectra recoded in this interval are, once again, very complex and exhibit numerous signals (see Figure S2, Supporting Information). At 545 °C, the most intense signals in the range below 80 Da indicate release of methane (*m/z*=16,15,14) and ethene (*m/z*=28,27,26). These stand out above a sequence of peaks already present in the second TIC event between 350 and 450 °C, albeit these appear here with lower intensity. A group of signals with mass up to 140 Da and high intensity complements this MS spectra (Figure 9). This part of the mass spectrum is the object of the following discussion.

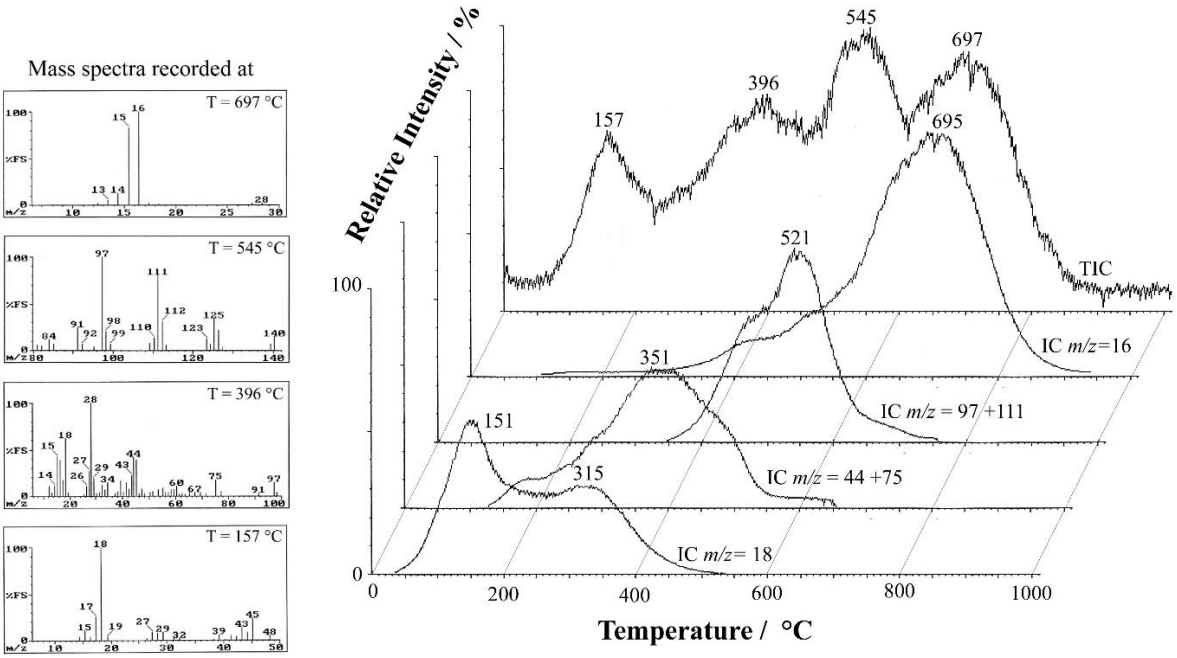

Figure 9. Left: Mass spectra recorded during TG-MS analysis of the PHMS/DVT aerogel at selected temperatures. Right: Total Ion Current and Ion Current curves of representative ions used to monitor the release of water (*m/z*=18), unidentified low molecular weight organic fragments (*m/z*=44 and *m/z*=75), double anchored thiophene species (*m/z*=97 and *m/z*=111), and methane (*m/z*=16).

During polymerization, the cross-linking agent DVT anchors to siloxane chains by reaction of its vinyl groups, as shown in Scheme 1. The hydrosilylation reaction between PMHS and DVT yields formation of ethylene bridges. Decomposition of these bridges occurs during the third thermal event and involves any one of the three single bonds: Si–CH_2–CH_2–C(thiophene). Depending on where the scission happens, different species will evolve. A mass spectrum recorded at 545 °C is shown in Figure 9. We identified several thiophene-derived species by considering signals attributed to molecular ions and their related ionic fragments, and corresponding chemical species. These are listed in Table 1. Note that the table contains fragmentation products arising from DVT doubly anchored with PMHS as well as DVT with a single anchor to PMHS. The relative intensities of the fragments allow us to estimate the proportion of these doubly bonding modes of DVT relative to siloxane. We found that more than 80% of the initial DVT molecules are doubly anchored to siloxane chains acting as cross-linker within the polymeric aerogel. Only a minor fraction of the DVT is singly bonded. In the latter case, molecules evolving during the thermal decomposition still bear the vinyl group. Among the molecular fragments we also observed significant amounts of methane and ethene together with minor ethane in mass spectra taken at 545 °C. Development of these light hydrocarbons predominantly emerges from decomposition of ethylene bridges between PMHS and DVT. Further details of the analysis are given in the Supporting Information.

Table 1. Compounds identified in the mass spectra recorded at 545 °C during TG-MS analysis arising from the thermal decomposition of the DVT molecule double- or single-anchored to the PMHS chains.

compound	molecular weight	most intense ion (full-scale) in its pure mass spectra	relative abundance in recorded mass spectra, %	CAS number of species***
species arising from DVT double-anchored with			87 *	
2,5-diethyl thiophene	140	125	16 *	5069-23-8
2-ethyl-5-methyl	126	111	31 *	40323-88-4
2,5-dimethyl	112	111	17 *	638-02-8
2-methyl thiophene	98	97	17 *	554-14-3
thiophene	84	84	6 *	110-02-1
species arising from DVT single-anchored with			13 *	
2-ethyl-5-vinyl	138	123	1 *	
2-methyl-5-vinyl	124	123	7 *	
2- vinyl thiophene			5 *	1918-82-7
species arising from C atoms evolving from partial decomposition of PMHS-DVT ethylene bridges				
methane	16	16	60 **	74-82-8
ethene	28	28	27 **	74-85-1
ethane	30	28	13 **	74-84-0

* relative % value calculated only among different thiophene-derived species

** relative % value calculated only among different light hydrocarbons

******* species with mass spectra of pure substance available in the literature[243]

Conclusion

We have demonstrated synthesis of a novel polysiloxane aerogel through hydrosilylation of PMHS and DVT under highly diluted conditions. To the best of our knowledge, this is the first time that a sulfur containing heterocycle is used to cross-link polysiloxanes and to prepare polymeric siloxane-based aerogels. In this reaction, divinylthiophene reacts with polymethylhydrosiloxane to yield a cross-linked polymer. Crosslinking is supported by disappearance of FT-IR bands characteristic of vinyl groups and through fragmentation adducts observed by TB-MS. Under highly dilute conditions the hydrosilylation reaction provided a wet gel, which was dried in supercritical CO2 leading to a polymeric aerogel. The microstructure of the product shows coalesced nanoparticles with diameters of about 165 nm, with sulfur being distributed homogeneously in the aerogel. Nitrogen isotherms show substantial hysteresis between absorption and desorption branches, and porosimetry yields a pore size distribution between 5 and 25 nm with a maximum at 12 nm. Thermogravimetric Analysis of the aerogel indicates its thermal stability is higher than any of its pure constituents, and comparable to other, non-sulfur bearing, linkers. Gas phase analysis by TG-MS of the volatiles released during annealing suggests the doubly anchored DVT bridges between PMHS chains dominate the singly attached adduct. Sulfur ultimately disappears during annealing as the thiophene derivatives are released from the degrading aerogel. We believe this new DVT-PMHS compound may be useful for preparation of novel sulfur-containing polymer-derived aerogels (PDC-aerogels), with an array of possible applications.

Acknowledgements

This work was supported by the National Science Foundation (NSF) through award CMMI-1634448. JJ thanks UT Arlington Interdisciplinary Research Program. The NSF (CHE-0234811 and CHE-0840509) is acknowledged for partial funding of the purchases of the NMR spectrometers used in this work.

Supporting Information

Novel sulfur-containing cross-linking agent for Si-based preceramic polymers

Poroshat Taheri, Apparao Bokka, Parham Asgari, Junha Jeon, John C. Lang, Renzo Campostrini, Gian Domenico Sorarù and Peter Kroll[203]

Thermogravimetric Analysis coupled with Mass Spectroscopy of evolved gases (TG-MS)

First thermal-degradation-event

As shown in Figure 9 (in main body of the paper), water is released following a bimodal trend with maxima centered at 151 and 315 °C respectively, as has been observed in titanium-oxide or silicon-oxide matrices obtained via sol-gel synthesis.[241, 244-247] It is well known that the relative increase in activation energy of similar processes can be inferred from the dependence of their conversions on temperature. In our TG-MS measurements we usually refer to the top-peak temperature of the TIC-curve, or better the IC-curve of suitable *m/z* ions, in order to obtain the relative activation energies referred to a specific thermal event. For the methyl-derived silica gel studies, by assessing the shift of the of top-peak temperature of the *m/z*=18 IC curves the inferred activation energy value indicate that in the first event (which falls in the range of 100-150 °C) is more probably attributed to the release of water molecule chemically absorbed on the inorganic matrix ($E_{act.en.} \approx$

15-20 kJ/mol): ≡Si–O–H···OH_2 → ≡Si–O–H + $H_2O_{(g)}$. The later events instead belong to a temperature range of 200-350 °C, which is consistent with the course of a solid-state chemical-reaction ($E_{act.en.}$ ≈ 60-70 kJ/mol), such as the condensation of vicinal silanol groups along the siloxane chains:[241] ≡Si–O–H··+ H–O–Si≡ → ≡Si–O–Si≡ + $H_2O_{(g)}$.

Fourth thermal-degradation-event

In our previous study on a silica matrix obtained from methyl derived silicon alkoxides, we usually observed methane release in a temperature interval around the 700 °C for the incipient evolution. Small amounts, of methyl-silanes and light methyl siloxane oligomers also have been observed. All these species arise from the restructuring of the siloxane chains by bond exchange between Si–O and Si–CH_3 bonds.[238, 240] In the present case with the DVT cross-linked polymeric aerogel, no further restructuring of its siloxane chains appear to occur following elimination of the DVT-counterparts, in contrast with the final release around the 695 °C of the silylated methyl groups observed previously. Indeed, at this stage only the gas-phase evolution of CH_4, H_2 are detected, while in the residual solid a partial introduction of C-atoms (forming a new SiOC structure) or a segregated free C-phase may occur.

Third thermal degradation event; i.e.: decomposition and fragmentation pathways of DVT cross-linker.

In the absence of TG-GC-MS analysis that could provide chromatographic separation of the different molecular species concurrently evolved in the gas phase at 545 °C from the thermal

decomposition of the cross-linking agent, the attempt to identify these compounds relies on the mass spectral evidence and its interpretation, which is based on our understanding of the origin of the ion fragments generated by the electron impact ionization. As described in Scheme 1 (main body), we hypothesized that DVT reacts with the PMHS polymer to form a diethylene bridge. In the temperature range of the third thermal decomposition event, the intrinsic stability of the thiophene aromatic-ring conserves its integrity, while the site of degradation focuses on the cleavage of the single-bonds of the ethylene bridge. Taking this into account, we considered the variety of compounds that may arise from different locations of ethylene bond cleavage. We searched for mass spectra of these species in the available data bases in order to understand their primary and sequential fragmentation pathways. For each species, the relative intensity of their molecular ions and of their main fragment ions were calculated. Scheme 2 summarizes these pathways for the most important ions and ion fragments generated by the ionization of these thiophene-derived species.

Scheme 2. Fragmentation pathways of the primary thiophene derived molecular species generated at 545 °C whose ionization products were detected in the mass spectra. For each species their molecular ion [MI] and their main intense fragment ions [FI] are reported followed by their *m/z* value and relative intensity.

#1. 2,5-diethyl thiophene

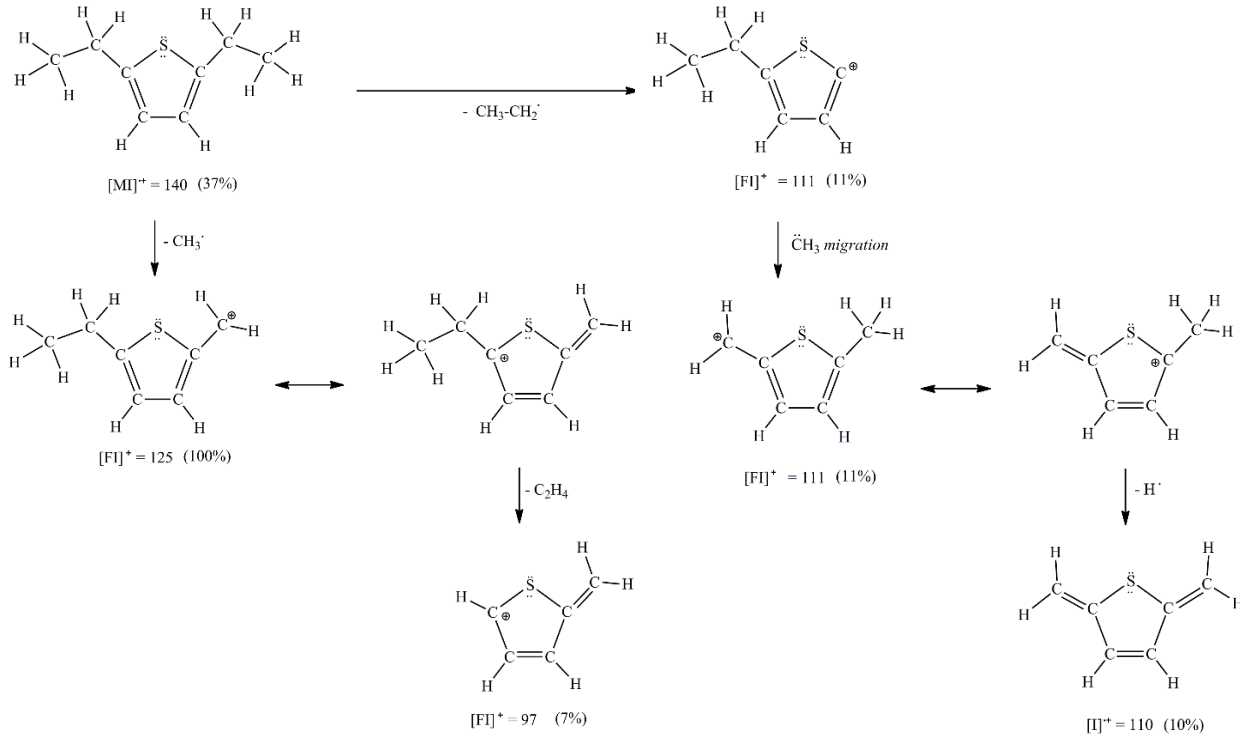

#2. 2-ethyl-5-methyl thiophene

#3. 2,5-dimethyl thiophene

#4. 2-methyl thiophene

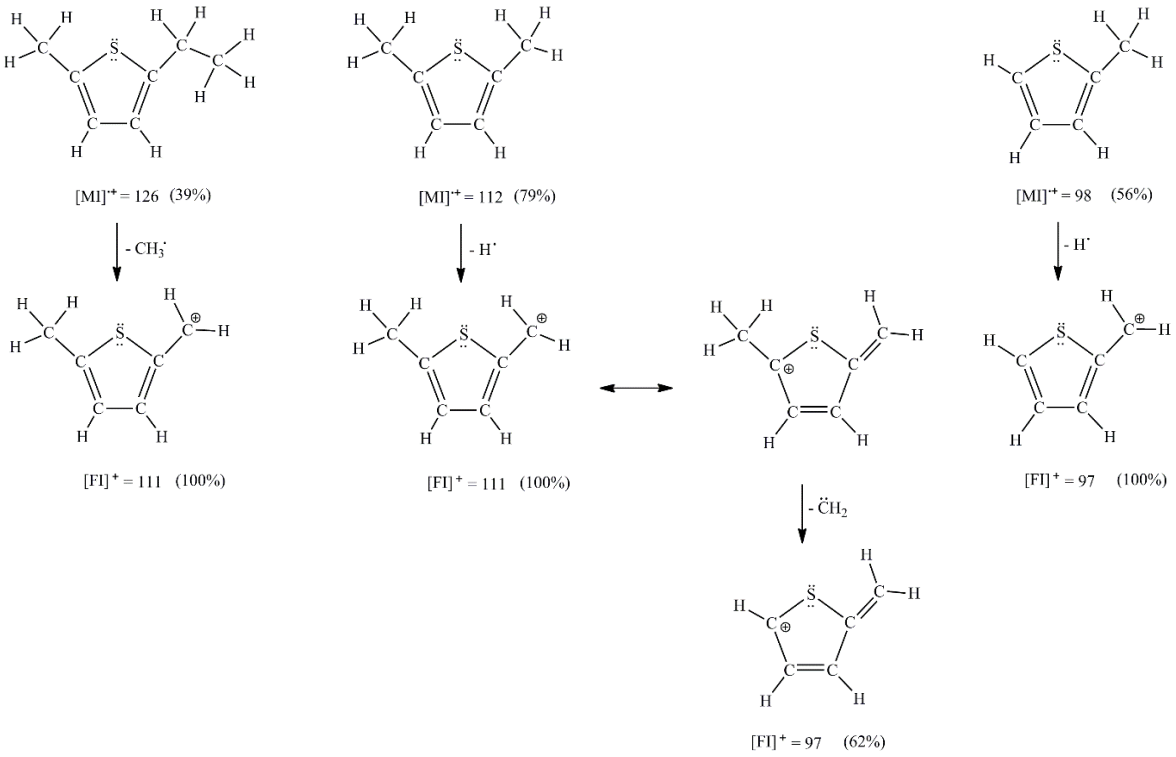

#5. 2-ethenyl thiophene (or 2-vinyl thiophene)

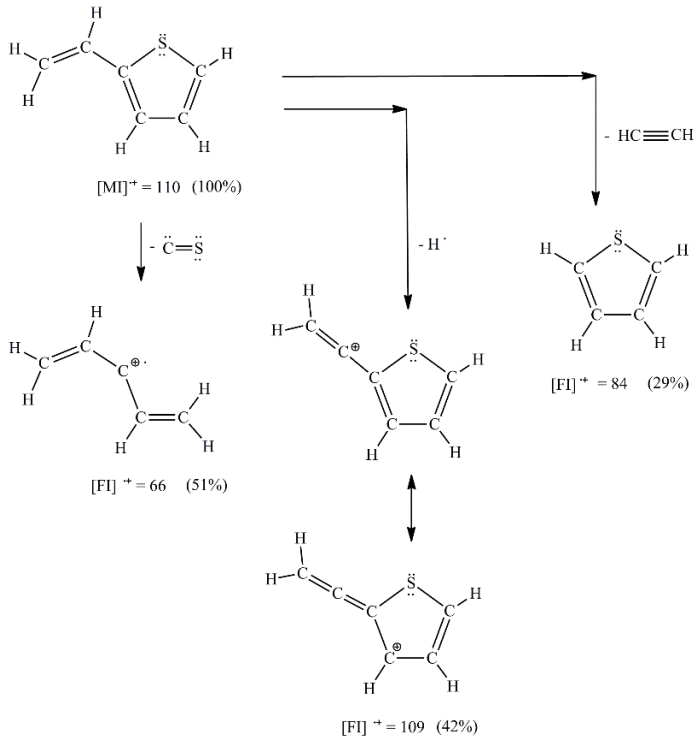

#6. Thiophene

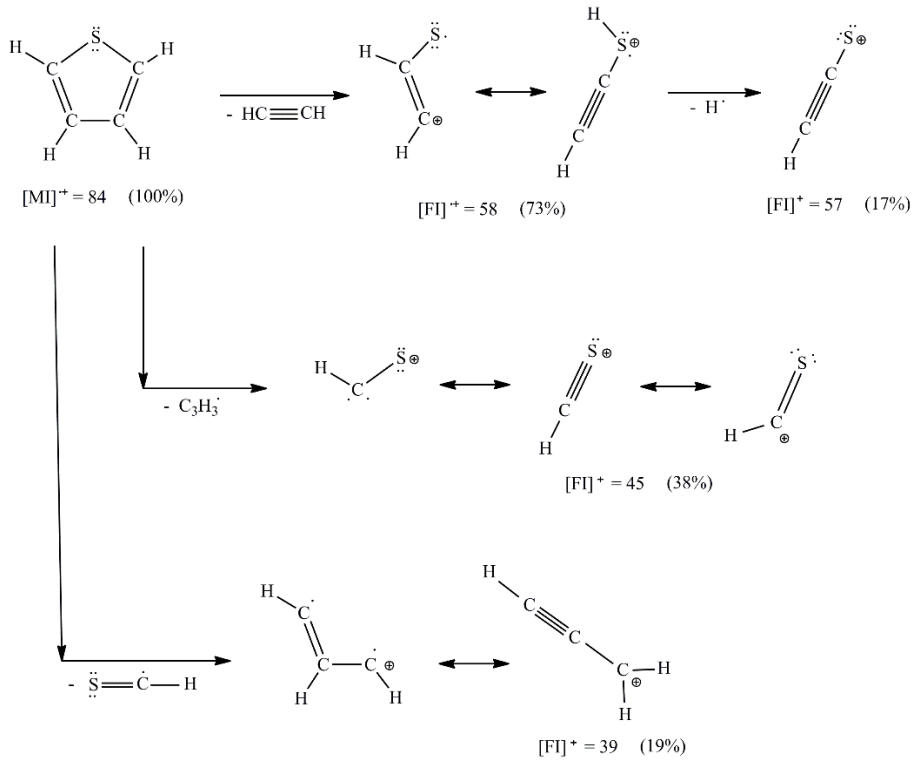

Through comparison of the mass spectra of these molecular ions and understanding of their relative stability, the following simple considerations can be drawn about the fragmentation pathways for the parent species.

• Saturated alkyl radicals bonded to the thiophene ring became less stable with increased C-C chain length.

• The electron impact leads to the preferential cleavage of the C-C bond between the first and second C-atoms of the alkyl chain, yielding to the formation of a fragment ion with a methylene carbocation group, where the positive charge can be distributed inside the entire aromatic ring by mesomeric effect (as described by four limit resonance formulas).

• In thiophene compounds bearing only a single alkyl group (in C2 position, e.g., **#4** and **#5**) this fragment-ion became the most stable and intense one (the full-scale ion in the mass spectra), followed by the molecular ions with a relative intensity usually lower than 35 %. These are the only two significant ions present in the mass spectra of these molecules.

• Only for the 2-methyl thiophene, **#4**, is there cleavage of the usually stronger H–C bond in the methyl group, instead of the C–C in longer alkyl chains. This leads to a higher presence of the molecule ion (*m/z*=98), which reaches 56% intensity of the full-scale methylene-thiophene cation (*m/z*=97).

A different fragmentation pattern is shown for 2-ethenyl-thiophene, **#5**, where the double bond of the vinyl group is in resonance with the aromatic ring. In this case the molecular ion becomes the most stable and intense ion in the mass spectra (at full-scale). The second most intense ion is formed by the loss of a neutral CS molecule from the molecular ions. The third most intense ion is due to the loss of an H-atom from the molecular one, probably that bonded to the first carbon atom of the vinyl group, where the formation of a positive charge could lead to the formation of a new double bond with the C(2) of the thiophene ring. This fact also permits the delocalization of the positive charge inside the aromatic ring. The least abundant ion is generated by the release, again from the molecular ion, of a neutral ethene molecule of from the vinyl group.

The mass spectra of 2,5-dimethyl-thiophene, **#3**, mimics the behavior of the 2-methyl-thiophene, **#4**. The full-scale ion corresponds to the loss of a H-atom from one of the methyl group leading to an initial methylene carbon-cation (of *m/z*=111). When this positive charge is delocalized (by resonance effect) inside the aromatic ring up to the carbon atom bearing the second methyl group, by an H-atom transfer from this methyl group to the charged one a neutral methylene

release could yield the third more intense ion (*m/*z=97) present in the mass spectra of this compound.

A similar pathway is also observed for 2,5-diethyl-thiophene, **#1**. As discussed before, the easier cleavage of the C–C bond inside the ethyl group (instead of the C–H) leads to greater abundance of the methylene carbocation (*m/z*=125). This fact leads to the lower intensity shown by the molecular parent (*m/z*=140). When the positive charge is considered to reach the symmetric carbon that bears the second ethyl group a release of a neutral ethene molecule (by an 1,3 H transfer from the last methyl carbon to the C-ion of the ring) a new secondary ion (*m/*z=97) could be formed although in low intensity. In this chemical species a new different fragmentation pathway is observed. Probably due to the less stable presence of the longer alkyl group the direct release of the entire ethyl group is observed with the formation of a positive charge on the carbon of the ring (*m/*z=111). Due to the free rotation of the single C–C bonds on the remaining ethyl group, present in the symmetric position in the ring, the methyl transfer from the ethyl group to the starting carbon-ion is reasonably hypothesized, so a new structural isomer is formed. Now this new methylene carbocation can delocalize its charge by resonance inside the entire aromatic ring, conferring a quite a good stability to this ion. Moreover, when this positive charge is considered again reaching the carbon atom bearing the transferred methyl group a further release of a hydrogen atom from this methyl group can lead to the formation of a second methylene group bonded to the ring, yielding a molecular radical-ion characterized by three alternate double bonds with an even mass value (*m/*z=110). Moreover, this secondary ion shows an intensity close to the one of its precursors. Indeed, in all these other alkyl-derived thiophene-species the direct cleavage of the alkyl group from the C-atom of the ring in not significantly observed.

The mass spectra of 2-ethyl-5-methyl-thiophene, **#2,** is attributable to the parent ion and only one derived ionic specie. The full-scale ion arises from the cleavage of the C–C bond inside the ethyl group; the loss of the methyl group leads to a methylene cation which charge can be distributed inside the aromatic ring yielding the ion at *m/*z=111. The molecular ion (*m/*z=126) is the only other significant ion, with an intensity of 39%.

We were unable to record mass spectra of the other two hypothesized species: 2-ethenyl-5-ethyl-thiophene (*m/*z=138) and 2-ethenyl-5-methyl-thiophene (*m/*z=124). For these two species, we assumed that the ionization pattern consists in the presence of their molecular ion and the common fragmentation ion (of *m/*z=123) arising respectively from the loss of the methyl in the ethyl group or of an H-atom in the methyl group. This assumption was made considering the intrinsic behavior shown in the mass spectra of the three species methyl-ethyl, **#2**, and ethenyl-thiophene, **#5**.

In order to identify the thiophene-derived species released during the third thermal event and those detected in the mass spectra recorded at 545°C the adopted criterion and the relative data processing is summarized in the following points.

• The mass spectra recorded at the maximum of the third TIC peak (at 545 °C) were carefully analyzed by measuring the relative heights of all the detected *m/z* signals.

• The presence of the molecular ion of each of these hypothesizes thiophene-compounds was searched among the signals recorded in the 545 °C mass spectra starting, one after the other, from the specie with the highest molecular mass.

• When the presence of a thiophene-derived specie was revealed, finding its molecular ion, taking into account the relative intensities of all its fragment-ions (as firstly calculated in the mass spectra

of its pure substance) the contribution of all its ions were subtracted from the heights of these *m/z* signals in the 545 °C mass spectra. So, the presence of each compound was deleted from those of the other (remaining) species.

• An acceptable qualitative description of the total picture of evolved thiophene-derived species was obtained when the higher molecular weight portion of the-processed 545 °C mass spectra was reset based on the analysis of the *m/z* signals in the 84-140 range.

An estimate of the relative percentage presence of the thiophene-derived species was then calculated as described below.

• For each species from the measured height of the m/z signal corresponding to its molecular ion the corresponding height of its full-scale ion was calculated (knowing the relative intensities of the ions inside the mass spectra of the pure substance).

• From the sum of all the full-scale ions of all the identified species their relative percentage presence, in the evolve mixture, were deduced. Indeed, in this approach it was assumed that all the species are ionized, by electron impact, with the same efficiency. This last assumption is, at least in part, justified by the high value of the electron impact energy (70 eV) used in recording the TG-MS analysis.

Table 1 (main body) summarizes the detected and identified thiophene-derived molecules. It also estimates the relative percentage present. These species were subdivided into two groups. The first, the species still bearing a vinyl group, is considered arising from DVT molecules that were only mono anchored to the PMHS siloxane chains. All the others bearing one or two saturated alkyl radicals (ethyl or methyl groups) together with the thiophene, are considered arising from DVT molecules that were double anchored to the siloxane chains. These last, that behaved as

concrete cross-linker inside the polymer aerogels, have been detected in a higher presence (around 87 %). The consistency of this thermal-decomposition interpretation is also supported by the relevant presence of the kind and amounts of CH_4, $CH_2{=}CH_2$ and $CH_3{-}CH_3$ also detected in the 545 °C mass spectra.

As briefly described in the previous text, during the thermal release of DVT counterparts from the siloxane chains, depending on which of the ethylene bonds is broken and how many C-atoms remain effectively attached to the thiophene-ring in the released compounds, the remaining C-atoms of the bridge are available to yield simple light-weight hydrocarbons. In fact, these "*available-C-atoms*" could easily react with the hydrogen radicals, also produced at this stage of the thermal decomposition.[238]

Similar to what has been described for the qualitative and semi-quantitative determination of the derived thiophene species, the mass spectra of these three hydrocarbons and their corresponding signals present in the 545 °C mass spectra were processed in an analogous manner. The relative percentages of these hydrocarbons also are reported in Table1. By comparing the heights of the full-scale ions of these light-hydrocarbons and those of the derived thiophene species, which molecular structure allowed the release of C-atoms prone to form hydrocarbons, a coherent correlation was found. At this temperature (545 °C), the 94 % of these "*free-available*" C-atoms seems to be employed in the formation of the detected light-hydrocarbons (in particular yielding the 60 % of methane, the 27 % of ethene and the 13 % of ethane, respectively) and only about 4 % would be available to yield a segregated graphite-phase.

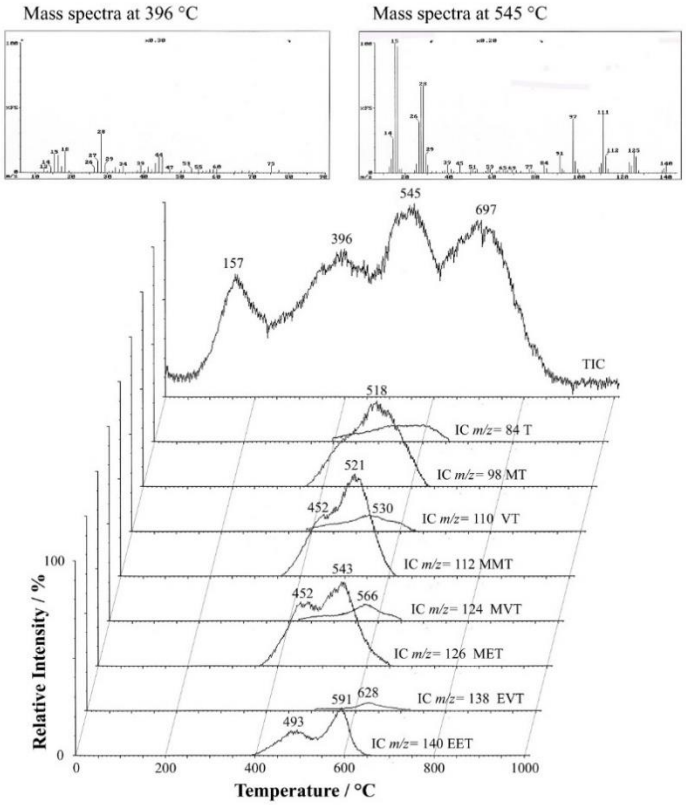

Figure S2. Top: Mass spectra recorded during TG-MS analysis of the PHMS/DVT aerogel at 396°C ($5 < m/z < 90$) and at 545°C ($5 < m/z < 140$). Bottom: TIC together with IC curves of released species arising from thermal decomposition of the thiophene cross-linking agent recorded during pyrolysis of the PHMS/DVT aerogel.

CHAPTER V: CONCLUSION

5.1 Effect of Solvents on Porosity of Aerogels

Using the synthesis solvent as a pore generating factor for modifying and controlling the porosity of silica aerogels is well documented in the literature.[248-250] There are also studies on the solvent effect on the pore structure of polymeric aerogels such as polyimide aerogels[251-252] or cellulose aerogels.[253]

In the chapter II the of solubility/swelling of the polymeric SiCO wet gels in different solvents and solvents' mixtures were discussed. The observations could be almost rationalized and predicted via HSP theory. Consequently, in the chapter III the effect of the solvent choice of the porous structure SiCO aerogels after the drying process was investigated.

5.1.1 Effect of Good and Bad Solvents of Porosity of SiCO Aerogels

Studies of the SiCO aerogels suggest that selected solvents have an important role on their pore structure at both polymeric and ceramic stages. Soraru *et al.* studied polymeric and ceramic SiCO aerogels synthesized by using the same precursors but in different solvents.[112] They used these different porous structures generated by the solvents' choice to measure the lithium charge/discharge capacity in each aerogel for Li ion storage applications.[112] Their study demonstrated that the selected synthesis solvents, acetone and cyclohexane, influence the

morphology of the final polymeric and ceramic aerogels. Kroll *et al.* also investigated the impact of solvents on the microstructure of SiCO aerogels made by the same PMHS-DVB precursor selecting more choices of synthesis solvent as it is shown in Figure 3-1.[96] The study showed that the interaction between the solvents and the precursor polymer is major factors governing pore formation of these PMHS-DVB polymer aerogels. Therefore, different pore size distributions were resulted from the porous structures generated with different synthesis solvents as it is shown in the Figure 3-2. Also, these interactions can be rationalized by using Hansen's approach to solubility of PMHS-DVB polymeric gel in the selected solvents.

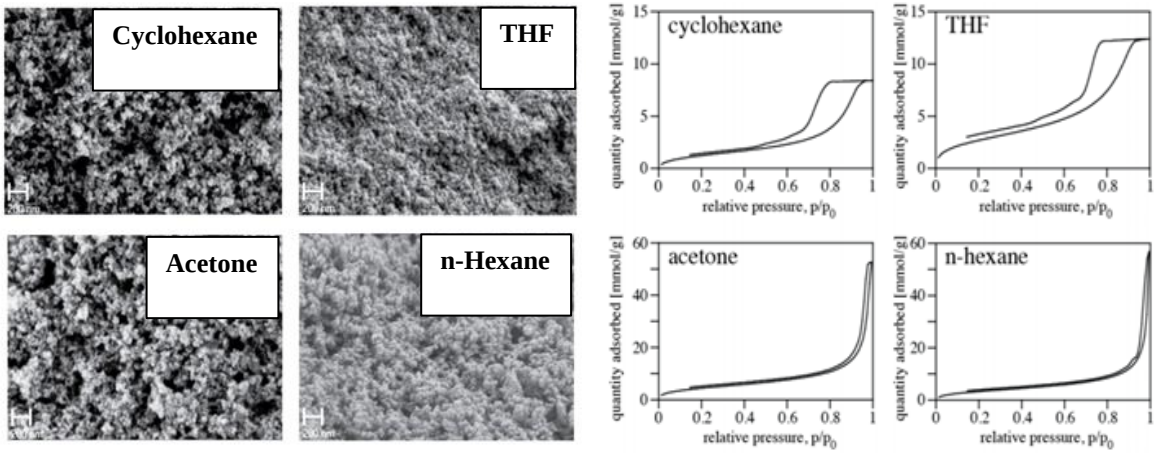

Figure 5-1. Microstructures of PMHS-DVB polymeric aerogels in various solvents. Adopted from Aguirre-Medel *et al.* 2018[96]

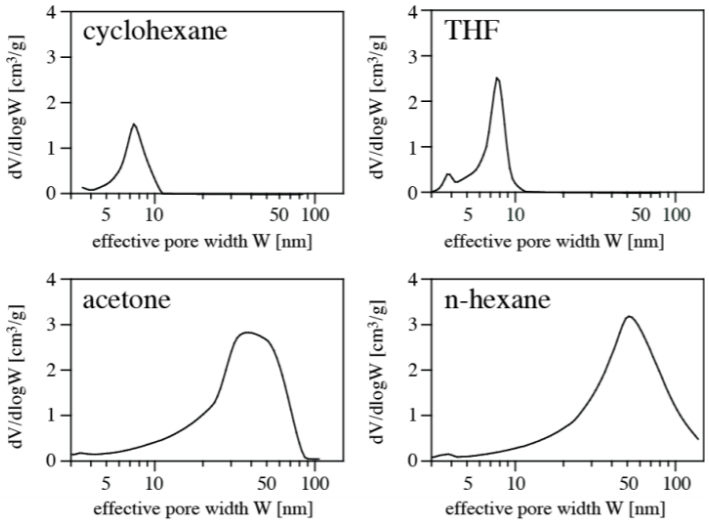

Figure 5-2. BJH pore size distribution of PMHS-DVB polymeric aerogels in various solvents. Adopted from Aguirre-Medel *et al.* 2018[96]

The isotherms of PMHS-DVB aerogels synthesized in cyclohexane, THF, acetone, and n-Hexane can be categorized Type IV based on the IUPAC isotherm categorization described in the Section 1.3.2. However, these aerogels hysteresis types (also, the IUPAC hysteresis categorization is described in the Section 1.3.2) were different from each other. The hysteresis type of aerogels synthesized in cyclohexane and THF is categorized as H2b hysteresis whereas, the hysteresis type of PMHS-DVB aerogels synthesized in acetone and n-Hexane is categorized as H1. Also, BJH pore size distribution of PMHS-DVB aerogels synthesized in cyclohexane and THF have smaller range between 1-10 nm with their peaks around 8 nm, whereas BJH pore size distribution of PMHS-DVB aerogels synthesized in acetone and n-Hexane have broader range between 1-100 nm with their peaks located at bigger size mesopores around 50 nm (Figure 3-2). It is worthy to

mention that cyclohexane and THF exhibited linear shrinkage of over 30%, while samples synthesized in acetone and n-hexane contract only about 25%.[96]

Species	δ_D ($MPa^{1/2}$)	δ_P ($MPa^{1/2}$)	δ_H ($MPa^{1/2}$)	RED
PMHS	16.75	4.87	1.96	0
Cyclohexane	17.2	1	2	0.503
THF	16.8	5.7	8	0.772
Acetone	15.5	10.4	7	0.998
n-Hexane	14.9	0	0	0.813

Table 5-1. Hansen parameters of PMHS and the chosen solvents and their "relative energy distance" (RED) to PMHS.

Comparing HSP of the polymer and the selected solvents (Table 5-1) demonstrates that cyclohexane and THF are "good" solvents and acetone,

and n-hexane are "bad" solvents for PMHS polymer.

Figure 5-3 provides a model for pore formation with swelled polymers. It is assumed that the size of precipitating microgel particles, which is known as "radius of gyration", depends only on the polymer itself and is independent of the solvent used. So, the characteristic size of the microgel particles is the same no matter whether acetone, cyclohexane, n-hexane, or THF as solvent. Since a good solvent causes a high degree of swelling, the volume content of a "good" solvent, or in another word the better swelling agent, within a gel particle is larger than that of a "bad" solvent. If the solvent is removed, the microgel particles will shrink, and the higher the

degree of swelling is expected to cause the higher the shrinkage of the particles. Since the wet gel is formed by coalesced colloidal particles, the smallest particles, which originated from the better swelling agent, build up the structure with smallest average pore diameter. This conclusion agrees with the observed BJH pore size distribution of the studied aerogels.[96]

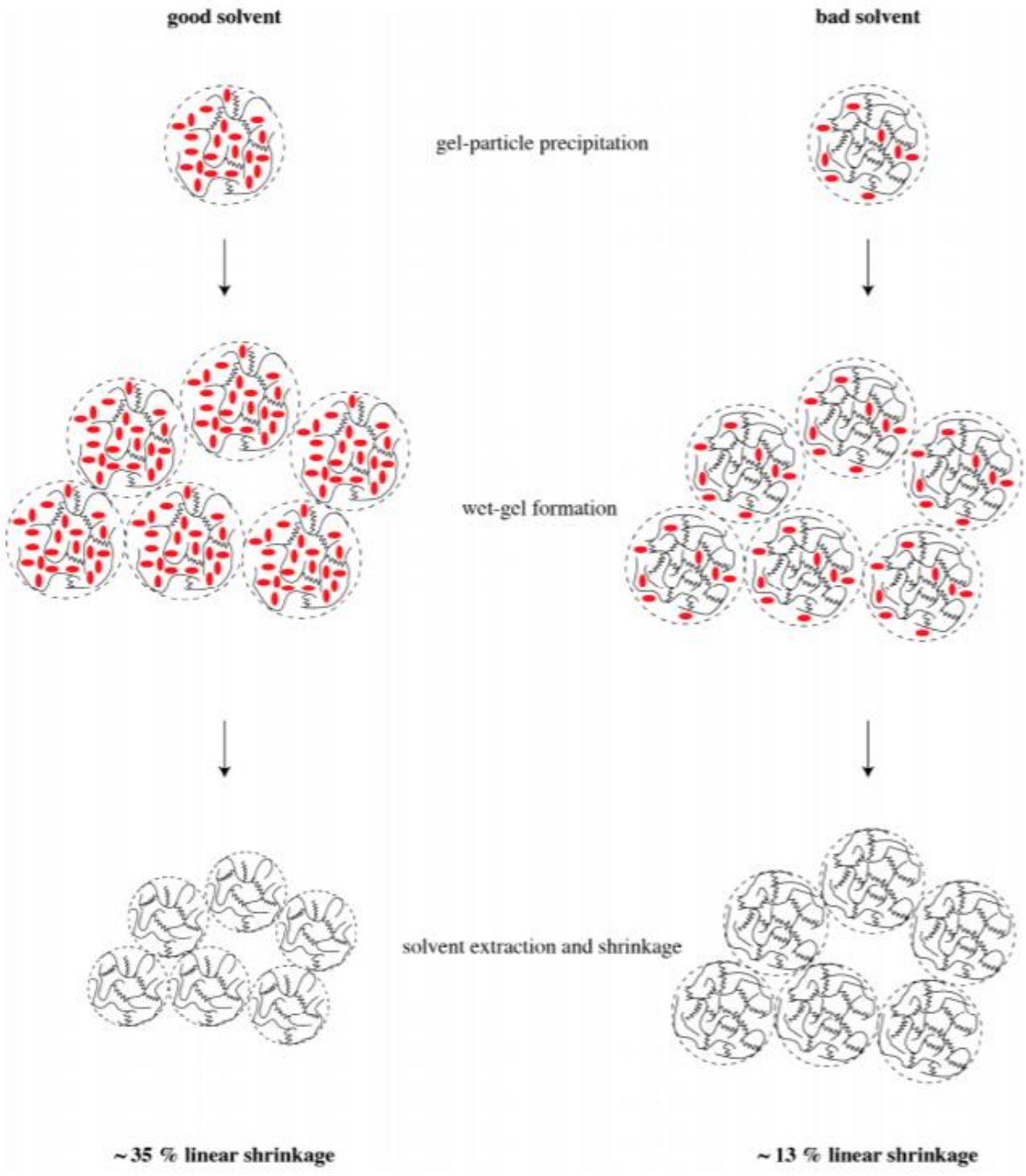

Figure 3-3. Illustration of colloidal particle formation, which they are the building blocks of final aerogel. Solvent molecules are shown in red; polymer strands are shown as black lines. Adopted from Aguirre-Medel *et al.* 2018[96]

5.1.2 Pore Morphology of SiCO Aerogels

As it was mentioned in the previous chapter all PMHS-DVB isotherms show hysteresis. All types of hysteresis were also described in the Section 1.3.3. PMHS-DVB aerogels synthesized in cyclohexane and THF is categorized as Type H2b hysteresis whereas, the hysteresis of PMHS-DVB aerogels synthesized in acetone and n-Hexane is categorized as Type H1.[96] As it was described in the Section 1.3.3, H1 type hysteresis attributes to narrow range of uniform mesopores and mostly cylindrical shape or networks of ink-bottle pores where the width of the neck (or window) size distribution is like the width of the pore size distribution. The Type H2(b) loop is also associated with large differential in neck and pore size distribution, which their connection to each other forms the geometry of bottle neck shape pores.[21] Different types of hysteresis and the geometries attributed to these types are illustrated in Figure 5-4.

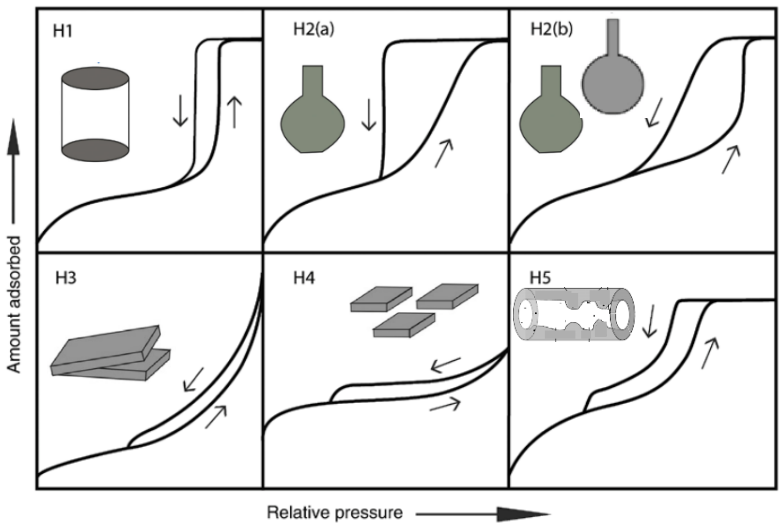

Figure 5-4. Different types of hysteresis based on IUPAC categorization. Adopted from Thommes *et al.* 2015[21]

Therefore, it can be concluded that good solvents for PMHS-DVB aerogels generate bottle neck shape pores with large differential in and pore size distribution whereas bad solvents mostly cylindrical shape pores qualitatively. However, there no study in the literature demonstrating a quantitative analysis on the geometry and hierarchical structure of pores on SiCO at its polymeric or ceramic stages.

5.2 Investigation of the Hierarchy of Porous Materials

There are few techniques to study the hierarchy of porous materials. X-ray tomography can be used for studying macroporous systems with a resolution of about 1 μm.[163-165] Transmission electron microscopy (TEM) is applied for ordered microporous materials such as zeolites and can reach a resolution of ~1 nm.[166-167] Early approaches of analyzing hysteresis loops observed in gas sorption focused on uniformly sized mesoporous systems.[168-171]

5.2.1 Differential Hysteresis Scanning Technique

Improvements in computational modeling have enabled scientists to study complex porous structures applying density functional, molecular dynamics and Monte Carlo methods, and statistical mechanical approaches. The influences of ever more complicated pore architectures, pore dimensionality, surface heterogeneity, and molecular interactions in different porous systems have facilitated by using the computational modeling techniques.[145-146] Modeling of both structure and thermodynamics of porous materials with complex architectures has improved interpretations

of experimental evaluations.[147-150] Non-local density functional theory (NLDFT) is an efficient statistical mechanic approach for analyzing the population density of a system of molecules interacting with pore walls.[151-155] Therefore, the adsorbent molecules behaviors such as the gradual buildup, and loss of solid-packing-like ordering, of multilayers in film formation, and condensation can be described by using these models. This approach has become an efficient tool for analyzing and interpreting porous structures.[37, 150, 156] Complementary theoretical and experimental studies of well-characterized, highly ordered, templated materials, such as M41S,[157] have validated this theoretical foundation of gas sorption used for pore characterization.[158]

In recent studies, the Differential Hysteresis Scanning (DHS) technique, which is coupled with an advanced modeling framework based on NLDFT, was developed by Kenvin *et al.*[254] and applied to study pore hierarchy in crystalline faujasites.[149-150] In this method the hysteresis of a Ar or N_2 isotherm is scanned completely. The scanning isotherm is acquired by partial saturation of the pore structure followed by a high-resolution desorption measurement, successively increasing/decreasing the pore saturation in a known amount of $\frac{p}{p_0}$ increment/decrement in each step. The incremental change in pore volume is subsequently calculated in stepwise cycles of partial saturation and complete emptying across the entire region of hysteretic part of in the isotherm in the way that the end of each adsorption branch outlines the largest diameter of saturated mesopores. This method Determines and categorizes pores based on their connectivity. The connectivity types are defined according to the relative diameter of the window to the diameter of mesopore body; pyramidal (pyr, $d_{meso} > 2$ nm, $d_{win} > d_{meso}$), constricted (con, $d_{win} > 2$ nm, $d_{win} < d_{meso}$), and occluded (occ, $d_{win} < 1$ nm, $d_{win} << d_{meso}$) mesopores. Different pore types and sizes manifest different subloop shapes shown in the Figure 5-5. NLDFT models for different pore types

based of their connectivity have been generated. They are then fitted and applied to the data resulted from the scanned subloops to extract the size distribution of saturated mesopores. The results then are shown in a 2D contour plot of the mesopore diameter with respect to the window size (Figure 5-13). As it was discussed this method was applied to study the porous structure of PMHS-DVB aerogels synthesized in acetone and cyclohexane in the chapter III.

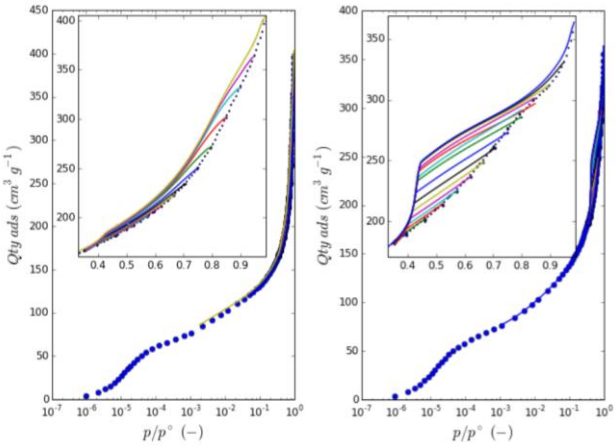

Figure 5-5. Different pore types and sizes manifest different subloop shapes in the DHS method. The pyramidal connectivity type of pores in hierarchically organized zeolite (HOZ) manifests subloop shapes of the scanned isotherm at the left. The occluded/constricted connectivity type of pores in Zeolite Socony Mobil-5 (ZSM-5) manifests subloop shapes of the scanned isotherm at the right.[255-256]

5.3 Future Investigation

As it was stated in the section 5.1.1 of this chapter the PMHS-DVB aerogels synthesized in THF and n-Hexane were also prepared in our group by Aguirre-Medel et al. Their pore morphologies will be studied by DHS technique as well. Our current BJH data provides only a view into pore window sizes, while DHS can reveal in addition the diameter of pores behind the window (not

captured by BJH). Thus, while BJH delivers a one-dimensional "projection" of window sizes, DHS provides a two-dimensional image of pore geometry distributions and clarifies distortions BJH can generate when there are pores of different sizes and connectivity.

Other porous systems (including common porous materials used frequently in industry such as SBA-15) can be also investigated by DHS. For applications, different pore hierarchies have their own advantages. Tailoring accessibility to a porous host is key in materials' applications such as catalysts carriers[254, 257] and drug delivery agents[181].

References

1. Klobes, P., Porosity and Specific Surface Area Measurements for Solid Materials. Meyer, K.; Munro, R. G., Eds. U.S. Dept. of Commerce, Technology Administration, National Institute of Standards and Technology: Gaithersburg, Md., 2006.
2. Ishizaki, K. z., *Porous Materials : Process Technology and Applications*; Kluwer Academic Publishers: Dordrecht ;, 1998.
3. Borns, D. J., Oil and Gas Industry Applications of Gas Flow in Porous Media. In *Gas Transport in Porous Media*, Ho, C. K.; Webb, S. W., Eds. Springer Netherlands: Dordrecht, 2006; pp 407-418.
4. Anovitz, L. M.; Cole, D. R., Characterization and Analysis of Porosity and Pore Structures. *Reviews in Mineralogy and Geochemistry* **2015**, *80*, 61-164.
5. Rouquerol, J.; Avnir, D.; Everett, D. H.; Fairbridge, C.; Haynes, M.; Pernicone, N.; Ramsay, J. D. F.; Sing, K. S. W.; Unger, K. K., Guidelines for the Characterization of Porous Solids. In *Studies in Surface Science and Catalysis*, Rouquerol, J.; Rodríguez-Reinoso, F.; Sing, K. S. W.; Unger, K. K., Eds. Elsevier: 1994; Vol. 87, pp 1-9.
6. Everett, D. H., Thermodynamics of Multiphase Fluids in Porous Media. *Journal of Colloid and Interface Science* **1975**, *52*, 189-198.
7. Martínez, C.; Corma, A., Zeolites. In *Comprehensive Inorganic Chemistry Ii (Second Edition)*, Reedijk, J.; Poeppelmeier, K., Eds. Elsevier: Amsterdam, 2013; pp 103-131.
8. Stock, N.; Biswas, S., Synthesis of Metal-Organic Frameworks (Mofs): Routes to Various Mof Topologies, Morphologies, and Composites. *Chemical Reviews* **2012**, *112*, 933-969.
9. Zhao, W.; Xia, L.; Liu, X., Covalent Organic Frameworks (Cofs): Perspectives of Industrialization. *CrystEngComm* **2018**, *20*, 1613-1634.
10. Rouquerol, J.; Fairbridge, C.; Everett, D.; Haynes, J.; Pernicone, N.; Ramsay, J.; Sing, K.; Unger, K., Recommendations for the Characterization of Porous Solids. *Pure and Applied Chemistry* **1994**, *66*, 1739.
11. Rouquerol, J., et al., The Characterization of Macroporous Solids: An Overview of the Methodology. *Microporous and Mesoporous Materials* **2012**, *154*, 2-6.
12. Brunauer, S.; Emmett, P. H.; Teller, E., Adsorption of Gases in Multimolecular Layers. *Journal of the American Chemical Society* **1938**, *60*, 309-319.
13. Lippens, B. C.; de Boer, J. H., Studies on Pore Systems in Catalysts: V. The T Method. *Journal of Catalysis* **1965**, *4*, 319-323.
14. Carrott, P. J. M.; Roberts, R. A.; Sing, K. S. W., Adsorption of Neopentane by Nonporous Carbons and Silicas. *Langmuir* **1988**, *4*, 740-743.
15. Carrott, P. J. M.; Sing, K. S. W., Multilayer Adsorption of Nitrogen and Alkanes by Non-Porous Carbons and Silicas. *Pure and Applied Chemistry* **1989**, *61*, 1835-1840.
16. Sing, K., Reporting Physisorption Data for Gas/Solid Systems with Special Reference to the Determination of Surface Area and Porosity. *Pure and Applied Chemistry - PURE APPL CHEM* **1982**, *54*, 2201-2218.
17. Matthias, T.; Katsumi, K.; Alexander, V. N.; James, P. O.; Francisco, R.-R.; Jean, R.; Kenneth, S. W. S., Physisorption of Gases, with Special Reference to the Evaluation of Surface Area and Pore Size Distribution (Iupac Technical Report). *Pure and Applied Chemistry* **2015**, *87*, 1051-1069.
18. Thommes, M.; Kaneko, K.; Neimark Alexander, V.; Olivier James, P.; Rodriguez-Reinoso, F.; Rouquerol, J.; Sing Kenneth, S. W., Physisorption of Gases, with Special Reference to the Evaluation of

Surface Area and Pore Size Distribution (Iupac Technical Report). *Pure and Applied Chemistry* **2015**, *87*, 1052-1069.
19. Thommes, M.; Smarsly, B.; Groenewolt, M.; Ravikovitch, P. I.; Neimark, A. V., Adsorption Hysteresis of Nitrogen and Argon in Pore Networks and Characterization of Novel Micro-and Mesoporous Silicas. *Langmuir* **2006**, *22*, 756-764.
20. Rouquerol, F.; Rouquerol, J.; Sing, K., Chapter 1 - Introduction. In *Adsorption by Powders and Porous Solids*, Rouquerol, F.; Rouquerol, J.; Sing, K., Eds. Academic Press: London, 1999; pp 1-26.
21. Thommes, M.; Cychosz, K. A., Physical Adsorption Characterization of Nanoporous Materials: Progress and Challenges. *Adsorption* **2014**, *20*, 233-250.
22. Landers, J.; Gor, G. Y.; Neimark, A. V., Density Functional Theory Methods for Characterization of Porous Materials. *Colloids and Surfaces A: Physicochemical and Engineering Aspects* **2013**, *437*, 3-32.
23. Thommes, M.; Kaneko, K.; Neimark Alexander, V.; Olivier James, P.; Rodriguez-Reinoso, F.; Rouquerol, J.; Sing Kenneth, S. W., Physisorption of Gases, with Special Reference to the Evaluation of Surface Area and Pore Size Distribution (Iupac Technical Report). In *Pure Appl. Chem.*, 2015; Vol. 87, p 1051.
24. Xiong, Q.; Baychev, T. G.; Jivkov, A. P., Review of Pore Network Modelling of Porous Media: Experimental Characterisations, Network Constructions and Applications to Reactive Transport. *J. Contam. Hydrol.* **2016**, *192*, 101-117.
25. Horvath, G.; Kawazoe, K., Method for the Calculation of Effective Pore Size Distribution in Molecular Sieve Carbon. *J. Chem. Eng. Jpn.* **1983**, *16*, 470-475.
26. Saito, A.; Foley, H. C., Curvature and Parametric Sensitivity in Models for Adsorption in Micropores. *AIChE Journal* **1991**, *37*, 429-436.
27. Cheng, L. S.; Ralph T, Y., Improved Horvath—Kawazoe Equations Including Spherical Pore Models for Calculating Micropore Size Distribution. *Chemical Engineering Science* **1994**, *49*, 2599-2609.
28. Rouquerol, F.; Rouquerol, J.; Sing, K., Chapter 8 - Assessment of Microporosity. In *Adsorption by Powders and Porous Solids*, Rouquerol, F.; Rouquerol, J.; Sing, K., Eds. Academic Press: London, 1999; pp 219-236.
29. López-Ramón, M. V.; Jagiełło, J.; Bandosz, T. J.; Seaton, N. A., Determination of the Pore Size Distribution and Network Connectivity in Microporous Solids by Adsorption Measurements and Monte Carlo Simulation. *Langmuir* **1997**, *13*, 4435-4445.
30. Thomson, W., Lx. On the Equilibrium of Vapour at a Curved Surface of Liquid. *The London, Edinburgh, and Dublin Philosophical Magazine and Journal of Science* **1871**, *42*, 448-452.
31. Barrett, E. P.; Joyner, L. G.; Halenda, P. P., The Determination of Pore Volume and Area Distributions in Porous Substances. I. Computations from Nitrogen Isotherms. *Journal of the American Chemical Society* **1951**, *73*, 373-380.
32. de Boer, J. H.; Linsen, B. G.; Osinga, T. J., Studies on Pore Systems in Catalysts: Vi. The Universal T Curve. *Journal of Catalysis* **1965**, *4*, 643-648.
33. Kruk, M.; Jaroniec, M.; Sayari, A., Adsorption Study of Surface and Structural Properties of Mcm-41 Materials of Different Pore Sizes. *The Journal of Physical Chemistry B* **1997**, *101*, 583-589.
34. Miyahara, M.; Kanda, H.; Yoshioka, T.; Okazaki, M., Modeling Capillary Condensation in Cylindrical Nanopores: A Molecular Dynamics Study. *Langmuir* **2000**, *16*, 4293-4299.
35. Casanova, F.; Chiang, C. E.; Li, C.-P.; Roshchin, I. V.; Ruminski, A. M.; Sailor, M. J.; Schuller, I. K., Gas Adsorption and Capillary Condensation in Nanoporous Alumina Films. *Nanotechnology* **2008**, *19*, 315709.

36. Lowell, S.; Shields, J. E.; Thomas, M. A.; Thommes, M., *Characterization of Porous Solids and Powders: Surface Area, Pore Size and Density*; Kluwer Academy 2004.
37. Monson, P. A., Understanding Adsorption/Desorption Hysteresis for Fluids in Mesoporous Materials Using Simple Molecular Models and Classical Density Functional Theory. *Microporous Mesoporous Mater.* **2012**, *160*, 47-66.
38. León y León, C. A., New Perspectives in Mercury Porosimetry. *Advances in Colloid and Interface Science* **1998**, *76-77*, 341-372.
39. Alemán, J. V., et al., Definitions of Terms Relating to the Structure and Processing of Sols, Gels, Networks, and Inorganic-Organic Hybrid Materials (Iupac Recommendations 2007). *Pure and Applied Chemistry* **2007**, *79*, 1801-1829.
40. Pajonk, G. M.; Repellin-Lacroix, M.; Abouarnadasse, S.; Chaouki, J.; Klavana, D., From Sol-Gel to Aerogels and Cryogels. *Journal of Non-Crystalline Solids* **1990**, *121*, 66-67.
41. Dixit, C. K.; Bhakta, S.; Kumar, A.; Suib, S. L.; Rusling, J. F., Fast Nucleation for Silica Nanoparticle Synthesis Using a Sol–Gel Method. *Nanoscale* **2016**, *8*, 19662-19667.
42. Thanh, N. T. K.; Maclean, N.; Mahiddine, S., Mechanisms of Nucleation and Growth of Nanoparticles in Solution. *Chemical Reviews* **2014**, *114*, 7610-7630.
43. Hector, A. L., Materials Synthesis Using Oxide Free Sol–Gel Systems. *Chemical Society Reviews* **2007**, *36*, 1745-1753.
44. Brinker, C. J.; Scherer, G. W., Chapter 2 - Hydrolysis and Condensation I: Nonsilicates. In *Sol-Gel Science*, Brinker, C. J.; Scherer, G. W., Eds. Academic Press: San Diego, 1990; pp 20-95.
45. Baumann, T. F.; Gash, A. E.; Satcher, J. H., A Robust Approach to Inorganic Aerogels: The Use of Epoxides in Sol–Gel Synthesis. In *Aerogels Handbook*, Aegerter, M. A.; Leventis, N.; Koebel, M. M., Eds. Springer New York: New York, NY, 2011; pp 155-170.
46. Gash, A. E.; Tillotson, T. M.; Satcher, J. H.; Poco, J. F.; Hrubesh, L. W.; Simpson, R. L., Use of Epoxides in the Sol−Gel Synthesis of Porous Iron(Iii) Oxide Monoliths from Fe(Iii) Salts. *Chemistry of Materials* **2001**, *13*, 999-1007.
47. Marciniec, B., *Hydrosilylation : A Comprehensive Review on Recent Advances*; Springer, 2010.
48. Sakaki, S.; Mizoe, N.; Sugimoto, M.; Musashi, Y., Pt-Catalyzed Hydrosilylation of Ethylene. A Theoretical Study of the Reaction Mechanism. *Coordination Chemistry Reviews* **1999**, *190-192*, 933-960.
49. Chen, J.-T., *Platinum: Organometallic ChemistryBased in Part on the Article Platinum: Organometallic Chemistry by Charles M. Lukehart* 2006.
50. Lewis, L.; Stein, J.; Gao, Y.; Colborn, R.; Hutchins, G., Platinum Catalysts Used in the Silicones Industry: Their Synthesis and Activity in Hydrosilylation. *Platinum Met Rev* **1997**, *41*.
51. Grachev, M. A.; Annenkov, V. V.; Likhoshway, Y. V., Silicon Nanotechnologies of Pigmented Heterokonts. *BioEssays* **2008**, *30*, 328-337.
52. Smith, D. M.; Stein, D.; Anderson, J. M.; Ackerman, W., Preparation of Low-Density Xerogels at Ambient Pressure. *Journal of Non-Crystalline Solids* **1995**, *186*, 104-112.
53. Hüsing, N.; Schubert, U., Aerogels—Airy Materials: Chemistry, Structure, and Properties. *Angewandte Chemie International Edition* **1998**, *37*, 22-45.
54. Prakash, S. S.; Brinker, C. J.; Hurd, A. J.; Rao, S. M., Silica Aerogel Films Prepared at Ambient Pressure by Using Surface Derivatization to Induce Reversible Drying Shrinkage. *Nature* **1995**, *374*, 439-443.
55. Kistler, S. S., Coherent Expanded-Aerogels. *The Journal of Physical Chemistry* **1932**, *36*, 52-64.

56. Leventis, N.; Sadekar, A.; Chandrasekaran, N.; Sotiriou-Leventis, C., Click Synthesis of Monolithic Silicon Carbide Aerogels from Polyacrylonitrile-Coated 3d Silica Networks. *Chemistry of Materials* **2010**, *22*, 2790-2803.
57. Witkowski, A.; Majkut, M.; Rulik, S., Analysis of Pipeline Transportation Systems for Carbon Dioxide Sequestration. *Archives of Thermodynamics* **2014**, 117-140.
58. Haranath, D.; Rao, A. V.; Wagh, P. B., Influence of Dccas on Optical Transmittance and Porosity Properties of Tmos Silica Aerogels. *Journal of Porous Materials* **1999**, *6*, 55-62.
59. Hench, L. L., Use of Drying Control Chemical Additives (Dccas) in Producing Gel Monoliths. In *Glass … Current Issues*, Wright, A. F.; Dupuy, J., Eds. Springer Netherlands: Dordrecht, 1985; pp 259-262.
60. Rolison, D. R.; Dunn, B., Electrically Conductive Oxide Aerogels: New Materials in Electrochemistry. *Journal of Materials Chemistry* **2001**, *11*, 963-980.
61. Nayak, A. K.; Das, B., 1 - Introduction to Polymeric Gels. In *Polymeric Gels*, Pal, K.; Banerjee, I., Eds. Woodhead Publishing: 2018; pp 3-27.
62. Pons, A.; Casas, L.; Estop, E.; Molins, E.; Harris, K. D. M.; Xu, M., A New Route to Aerogels: Monolithic Silica Cryogels. *Journal of Non-Crystalline Solids* **2012**, *358*, 461-469.
63. Ainger, F. W. a. H., J. M., *The Preparation of Phosphorus-Nitrogen Compounds as Non-Porous Solids*; Academic Press, New York 1960, p 168-82.
64. Popper, P. G. C. a. P., *Inorganic Polymers and Ceramics''*; Academic Press, New York, 1965.
65. Verbeek, W. Production of Shaped Articles of Homogeneous Mixtures of Silicon Carbide and Nitride. U.S. Patent No. 3853567, 1973, 1973.
66. Yajima, S.; Hayashi, J.; Omori, M.; Okamura, K., Development of a Silicon Carbide Fibre with High Tensile Strength. *Nature* **1976**, *261*, 683-685.
67. Fritz, G.; Raabe, B., Bildung Siliciumorganischer Verbindungen. V. Die Thermische Zersetzung Von Si(Ch3)4 Und Si(C2h5)4. *Zeitschrift für anorganische und allgemeine Chemie* **1956**, *286*, 149-167.
68. Colombo, P.; Mera, G.; Riedel, R.; Sorarù, G. D., Polymer-Derived Ceramics: 40 Years of Research and Innovation in Advanced Ceramics. *Journal of the American Ceramic Society* **2010**, *93*, 1805-1837.
69. Ionescu, E., Riedel, R., Polymer Processing of Ceramics. In *Ceramics and Composites Processing Methods*, pp 235-270.
70. Scheffler, M.; Colombo, P., *Cellular Ceramics: Structure, Manufacturing, Properties and Applications*; Wiley, 2006.
71. Vakifahmetoglu, C.; Zeydanli, D.; Colombo, P., Porous Polymer Derived Ceramics. *Materials Science and Engineering: R: Reports* **2016**, *106*, 1-30.
72. Colombo, P., Engineering Porosity in Polymer-Derived Ceramics. *Journal of The European Ceramic Society - J EUR CERAM SOC* **2008**, *28*, 1389-1395.
73. Buckley, J. D.; Strouhal, G.; Gangler, J. J., Early Development of Ceramic Fiber Insulation for the Space Shuttle. *BULL.-AM. CERAM. SOC* **1981**.
74. P.N, S.; Kirubanandam, S.; Av, J.; N, V.; Kannan, R., Corrosion of Ceramic Materials. CRC Press: 2018; pp 223–250.
75. Alvin, M. A.; Lippert, T. E.; Lane, J. E. In *Assessment of Porous Ceramic Materials for Hot Gas Filtration Applications*, American Ceramic Society Bulletin, 1991.
76. Prasad, R. M.; Jüttke, Y.; Richter, H.; Voigt, I.; Riedel, R.; Gurlo, A., Mechanism of Gas Separation through Amorphous Silicon Oxycarbide Membranes *Advanced Engineering Materials* **2016**, *18*, 721-727.
77. Konegger, T.; Patidar, R.; Bordia, R. K., A Novel Processing Approach for Free-Standing Porous Non-Oxide Ceramic Supports from Polycarbosilane and Polysilazane Precursors. *Journal of the European Ceramic Society* **2015**, *35*, 2679-2683.

78. Tamayo, A.; Mazo, M. A.; Ruiz-Caro, R.; Martín-Illana, A.; Bedoya, L. M.; Veiga-Ochoa, M. D.; Rubio, J., Mesoporous Silicon Oxycarbide Materials for Controlled Drug Delivery Systems. *Chemical Engineering Journal* **2015**, *280*, 165-174.
79. Arango-Ospina, M.; Xie, F.; Gonzalo-Juan, I.; Riedel, R.; Ionescu, E.; Boccaccini, A. R., Review: Silicon Oxycarbide Based Materials for Biomedical Applications. *Applied Materials Today* **2020**, *18*, 100482.
80. Feng, N.; Feng, Y.; Wei, Y.; Zhou, X., Preparation and Electrochemical Performance of a Porous Polymer-Derived Silicon Carbonitride Anode by Hydrofluoric Acid Etching for Lithium Ion Batteries. *RSC Advances* **2014**, *4*, 23694-23702.
81. Greil, P., Polymer Derived Engineering Ceramics. *Advanced Engineering Materials* **2000**, *2*, 339-348.
82. Lu, K.; Erb, D.; Liu, M., Thermal Stability and Electrical Conductivity of Carbon-Enriched Silicon Oxycarbide. *Journal of Materials Chemistry C* **2016**, *4*, 1829-1837.
83. Roth, F.; Schmerbauch, C.; Ionescu, E.; Nicoloso, N.; Guillon, O.; Riedel, R., High-Temperature Piezoresistive C / Sioc Sensors. *J. Sens. Sens. Syst.* **2015**, *4*, 133-136.
84. Sorarù, G. D.; Pederiva, L.; Latournerie, J.; Raj, R., Pyrolysis Kinetics for the Conversion of a Polymer into an Amorphous Silicon Oxycarbide Ceramic. *Journal of the American Ceramic Society* **2002**, *85*, 2181-2187.
85. Hourlier, D.; Venkatachalam, S.; Ammar, M.-R.; Blum, Y., Pyrolytic Conversion of Organopolysiloxanes. *Journal of Analytical and Applied Pyrolysis* **2017**, *123*, 296-306.
86. Blum, Y.; Sorarù, G. D.; Ramaswamy, A. P.; Hui, D.; Carturan, S. M., Controlled Mesoporosity in Sioc Via Chemically Bonded Polymeric "Spacers". *Journal of the American Ceramic Society* **2013**, *96*, 2785-2792.
87. Bréquel, H., et al., Systematic Structural Characterization of the High-Temperature Behavior of Nearly Stoichiometric Silicon Oxycarbide Glasses. *Chemistry of Materials* **2004**, *16*, 2585-2598.
88. Kleebe, H.-J.; Turquat, C.; Sorarù, G. D., Phase Separation in an Sico Glass Studied by Transmission Electron Microscopy and Electron Energy-Loss Spectroscopy. *Journal of the American Ceramic Society* **2001**, *84*, 1073-1080.
89. A. Karakuscu, R. G., L. Pavesi, G. D. Soraru, Synthesis and Optical Properties of Sicnc/Sio2 Nanocomposite Thin Films. In *Nanostructured Materials and Nanotechnology Ii: Ceramic Engineering and Science Proceedings, Volume 29, Issue 8*, Singh, S. M. M., Ed. The American Ceramic Society: Daytona Beach, FL, 2008; Vol. 29, pp 85-91.
90. Lu, K., Porous and High Surface Area Silicon Oxycarbide-Based Materials—a Review. *Materials Science and Engineering: R: Reports* **2015**, *97*, 23-49.
91. Saha, A.; Raj, R., Crystallization Maps for Sico Amorphous Ceramics. *Journal of the American Ceramic Society* **2007**, *90*, 578-583.
92. Brequel, H.; Parmentier, J.; Sorar, G. D.; Schiffini, L.; Enzo, S., Study of the Phase Separation in Amorphous Silicon Oxycarbide Glasses under Heat Treatment. *Nanostructured Materials* **1999**, *11*, 721-731.
93. Kroll, P., Modeling the 'Free Carbon' Phase in Amorphous Silicon Oxycarbide. *Journal of Non-Crystalline Solids* **2005**, *351*, 1121-1126.
94. Ponomarev, I.; van Duin, A. C. T.; Kroll, P., Reactive Force Field for Simulations of the Pyrolysis of Polysiloxanes into Silicon Oxycarbide Ceramics. *The Journal of Physical Chemistry C* **2019**, *123*, 16804-16812.

95. Soraru, G.; Dalcanale, F.; Campostrini, a.; Gaston, A.; Blum, Y.; Carturan, S.; Parakkulam Ramaswamy, A., Novel Polysiloxane and Polycarbosilane Aerogels Via Hydrosilylation of Preceramic Polymers. *J. Mater. Chem.* **2012**, *22*.
96. Aguirre, S.; Jana, P.; Kroll, P.; Soraru, G., Towards Porous Silicon Oxycarbide Materials: Effects of Solvents on Microstructural Features of Poly(Methylhydrosiloxane)/Divynilbenzene Aerogels. *Materials* **2018**, *11*, 2589.
97. Colombo, P.; Bernardo, E., Macro- and Micro-Cellular Porous Ceramics from Preceramic Polymers. *Composites Science and Technology* **2003**, *63*, 2353-2359.
98. Lu, P.; Huang, Q.; Mukherjee, A.; Hsieh, Y.-L., Sico-Doped Carbon Fibers with Unique Dual Superhydrophilicity/Superoleophilicity and Ductile and Capacitance Properties. *ACS Applied Materials & Interfaces* **2010**, *2*, 3738-3744.
99. Narisawa, M.; Sumimoto, R.-I.; Kita, K.-I.; Kado, H.; Mabuchi, H.; Kim, Y.-W., Melt Spinning and Metal Chloride Vapor Curing Process on Polymethylsilsesquioxane as Si□O□C Fiber Precursor. *Journal of Applied Polymer Science* **2009**, *114*, 2600-2607.
100. Vakifahmetoglu, C.; Zeydanli, D.; Innocentini, M. D. d. M.; Ribeiro, F. d. S.; Lasso, P. R. O.; Soraru, G. D., Gradient-Hierarchic-Aligned Porosity Sioc Ceramics. *Scientific Reports* **2017**, *7*, 41049.
101. Zeschky, J.; Höfner, T.; Arnold, C.; Weißmann, R.; Bahloul-Hourlier, D.; Scheffler, M.; Greil, P., Polysilsesquioxane Derived Ceramic Foams with Gradient Porosity. *Acta Materialia* **2005**, *53*, 927-937.
102. Vakifahmetoglu, C.; Colombo, P., A Direct Method for the Fabrication of Macro-Porous Sioc Ceramics from Preceramic Polymers. *Advanced Engineering Materials* **2008**, *10*, 256-259.
103. Yan, X.; Su, D.; Han, S., Phase Separation Induced Macroporous Sioc Ceramics Derived from Polysiloxane. *Journal of the European Ceramic Society* **2015**, *35*, 443-450.
104. Peña-Alonso, R.; Sorarù, G. D.; Raj, R., Preparation of Ultrathin-Walled Carbon-Based Nanoporous Structures by Etching Pseudo-Amorphous Silicon Oxycarbide Ceramics. *Journal of the American Ceramic Society* **2006**, *89*, 2473-2480.
105. Sorarù, G. D.; Modena, S.; Guadagnino, E.; Colombo, P.; Egan, J.; Pantano, C., Chemical Durability of Silicon Oxycarbide Glasses. *Journal of the American Ceramic Society* **2002**, *85*, 1529-1536.
106. Dibandjo, P.; Diré, S.; Babonneau, F.; Soraru, G. D., Influence of the Polymer Architecture on the High Temperature Behavior of Sico Glasses: A Comparison between Linear- and Cyclic-Derived Precursors. *Journal of Non-Crystalline Solids* **2010**, *356*, 132-140.
107. Biasetto, L.; Peña-Alonso, R.; Sorarù, G. D.; Colombo, P., Etching of Sioc Ceramic Foams. *Advances in Applied Ceramics* **2008**, *107*, 106-110.
108. Sorarù, G. D.; Pena-Alonso, R.; Leoni, M., C-Rich Micro/Mesoporous Si(B)Oc: In Situ Diffraction Analysis of the Hf Etching Process. *Microporous and Mesoporous Materials* **2013**, *172*, 125-130.
109. Singh, A.; Pantano, C., The Role of Si-H Functionality in Oxycarbide Glass Synthesis. *MRS Proceedings* **2011**, *271*.
110. http://www.aerogel.com/.
111. Sorarù, G. D. https://webapps.unitn.it/du/en/Persona/PER0003532/Curriculum.
112. Vallachira Warriam Sasikumar, P.; Zera, E.; Graczyk-Zajac, M.; Riedel, R.; Soraru, G. D., Structural Design of Polymer-Derived Sioc Ceramic Aerogels for High-Rate Li Ion Storage Applications. *Journal of the American Ceramic Society* **2016**, *99*, 2977-2983.
113. Sorarù, G. D.; Kundanati, L.; Santhosh, B.; Pugno, N., Influence of Free Carbon on the Young's Modulus and Hardness of Polymer-Derived Silicon Oxycarbide Glasses. *Journal of the American Ceramic Society* **2019**, *102*, 907-913.
114. Polymethylhydrosiloxane. In *Encyclopedia of Reagents for Organic Synthesis*.

115. Polymethylhydrosiloxane. https://www.sigmaaldrich.com/catalog/product/aldrich/176206?lang=en&region=US.
116. Polymethylhydrosiloxane.
117. Lu, S.; Melo, M. M.; Zhao, J.; Pearce, E. M.; Kwei, T. K., Organic-Inorganic Polymeric Hybrids Involving Novel Poly(Hydroxymethylsiloxane). *Macromolecules* **1995**, *28*, 4908-4913.
118. Blum, Y. D. Hydrdosloxanes as Precursors to Ceramic Products 09/21/1993, 1992.
119. Blum, Y. D.; MacQueen, D. B.; Kleebe, H.-J., Synthesis and Characterization of Carbon-Enriched Silicon Oxycarbides. *Journal of the European Ceramic Society* **2005**, *25*, 143-149.
120. Hildebrand, J. H., Solubility. Iii. Relative Values of Internal Pressures and Their Practical Application. *J. Am. Chem. Soc.* **1919**, *41*, 1067-1080.
121. Scatchard, G., Equilibria in Non-Electrolyte Solutions in Relation to the Vapor Pressures and Densities of the Components. *Chem. Rev.* **1931**, *8*, 321-333.
122. Hildebrand, J. H.; Prausnitz, J. M.; Scott, R. L., *Regular and Related Solutions: The Solubility of Gases, Liquids, and Solids*; Van Nostrand Reinhold Company, 1970.
123. Guggenheim, E. A., *Mixtures: The Theory of the Equilibrium Properties of Some Simple Classes of Mixtures, Solutions and Alloys*; Clarendon Press, 1952.
124. Hansen, C. M. The Three Dimensional Solubility Parameter and Solvent Diffusion Coefficient : Their Importance in Surface Coating Formulation. Danish Technical Press, Copenhagen, 1967.
125. Buckingham, A., Chemical Shifts in the Nuclear Magnetic Resonance Spectra of Molecules Containing Polar Groups. *Can. J. Chem.* **1960**, *38*, 300-307.
126. Lang, J. C.; Armstrong, D. W., Chiral Surfaces: The Many Faces of Chiral Recognition. *Current Opinion in Colloid & Interface Science* **2017**, *32*, 94-107.
127. Fuchs, O. In *The Molecular Theory of Solutions. Von 1. Prigogine, A. Bellemans Und V. Mathot. North-Holland Publishing Company, Amsterdam 1957. 1. Aufl., Xx, 448 S., 120 Abb., Geb. Hfl. 48*, 1958.
128. Nielsen, T. B.; Hansen, C. M., Elastomer Swelling and Hansen Solubility Parameters. *Polymer Testing* **2005**, *24*, 1054-1061.
129. Aguirre, S.; Jana, P.; Kroll, P.; Soraru, G., *Towards Porous Silicon Oxycarbide Materials: Effects of Solvents on Microstructural Features of Poly(Methylhydrosiloxane)/Divynilbenzene Aerogels*, 2018; Vol. 11, p 2589.
130. Su, X.; Shi, B.; Wang, L., Investigation on Three-Dimensional Solubility Parameters for Explanation and Prediction of Swelling Degree of Polydimethylsiloxane Pervaporation Membranes. *Journal of Macromolecular Science, Part B* **2015**, *54*, 1248-1258.
131. Taheri, P.; Lang, J. C.; Kenvin, J.; Kroll, P., Differential Hysteresis Scanning of Non-Templated Monomodal Amorphous Aerogels. *Physical Chemistry Chemical Physics* **2021**, *23*, 5422-5430.
132. McBain, J. W., Xcix. The Mechanism of the Adsorption ("Sorption") of Hydrogen by Carbon. *London, Edinburgh, and Dublin Philosophical Magazine and Journal of Science* **1909**, *18*, 916-935.
133. Gregg, S.; Sing, K., *Adsorption, Surface Area and Porosity. Academic Press, London*, 1982.
134. Sing, K. S. W., Reporting Physisorption Data for Gas/Solid Systems with Special Reference to the Determination of Surface Area and Porosity (Recommendations 1984). In *Pure Appl. Chem.*, 1985; Vol. 57, p 603.
135. Fowler, S. R. H.; Guggenheim, E. A., *Statistical Thermodynamics. A Version of Statistical Mechanics [by Rh Fowler] for Students of Physics and Chemistry*; Cambridge, 1939, p Chapter X.
136. Hill, T. L., Statistical Mechanics of Multimolecular Adsorption. I. *J. Chem. Phys.* **1946**, *14*, 263-267.

137. Hill, T. L., Extension of Fowler's Treatment of Surface Tension to Physical Adsorption. *J. Chem. Phys.* **1949**, *17*, 668-669.
138. Ross, S.; Olivier, J., *On Physical Adsorption, Willey and Sons*; Interscience Division of John Wiley & Sons: New York, 1964.
139. Frenkel, J., *Kinetic Theory of Liquids*; Oxford University Press, 1946.
140. Halsey, G., Physical Adsorption on Non-Uniform Surfaces. *Journal of Chemical Physics* **1948**, *16*, 931-937.
141. Pierce, C., The Frenkel-Halsey-Hill Adsorption Isotherm and Capillary Condensation. *Journal of Physical Chemistry* **1960**, *64*, 1184-1187.
142. Harkins, W. D.; Jura, G., Surfaces of Solids. Xiii. A Vapor Adsorption Method for the Determination of the Area of a Solid without the Assumption of a Molecular Area, and the Areas Occupied by Nitrogen and Other Molecules on the Surface of a Solid. *J. Am. Chem. Soc.* **1944**, *66*, 1366-1373.
143. Kruk, M.; Jaroniec, M.; Sayari, A., Application of Large Pore Mcm-41 Molecular Sieves to Improve Pore Size Analysis Using Nitrogen Adsorption Measurements. *Langmuir* **1997**, *13*, 6267-6273.
144. Everett, D., Adsorption Hysteresis,. In *The Solid-Gas Interface*, Flood, E., Ed. Marcel Dekker, Inc.: New York, 1967; Vol. 2, pp 1055-1113.
145. Gelb, L. D.; Gubbins, K.; Radhakrishnan, R.; Sliwinska-Bartkowiak, M., Phase Separation in Confined Systems. *Rep. Prog. Phys.* **1999**, *62*, 1573.
146. Dash, J., Transitions from Monolayers to Bulk Matter. *Le Journal de Physique Colloques* **1977**, *38*, C4-201-C4-206.
147. Kenvin, J.; Jagiello, J.; Mitchell, S.; Pérez-Ramírez, J., Unified Method for the Total Pore Volume and Pore Size Distribution of Hierarchical Zeolites from Argon Adsorption and Mercury Intrusion. *Langmuir* **2015**, *31*, 1242-1247.
148. Thommes, M., Physical Adsorption Characterization of Nanoporous Materials. *Chem. Ing. Tech.* **2010**, *82*, 1059-1073.
149. Kenvin, J.; Mitchell, S.; Sterling, M.; Warringham, R.; Keller, T. C.; Crivelli, P.; Jagiello, J.; Pérez-Ramírez, J., Quantifying the Complex Pore Architecture of Hierarchical Faujasite Zeolites and the Impact on Diffusion. *Adv. Funct. Mater.* **2016**, *26*, 5621-5630.
150. Warringham, R.; Mitchell, S.; Murty, R.; Schäublin, R.; Crivelli, P.; Kenvin, J.; Pérez-Ramírez, J., Mapping the Birth and Evolution of Pores Upon Thermal Activation of Layered Hydroxides. *Chem. Mater.* **2017**, *29*, 4052-4062.
151. Rowlinson, J.; Widom, B., Molecular Theory O [Capillarity (Oxford University Press). Chap: 1982.
152. Tarazona, P.; Evans, R., A Simple Density Functional Theory for Inhomogeneous Liquids: Wetting by Gas at a Solid-Liquid Interface. *Mol. Phys.* **1984**, *52*, 847-857.
153. Tarazona, P.; Marconi, U. M. B.; Evans, R., Phase Equilibria of Fluid Interfaces and Confined Fluids. *Mol. Phys.* **1987**, *60*, 573-595.
154. Seaton, N.; Walton, J.; Quirke, N., A New Analysis Method for the Determination of the Pore Size Distribution of Porous Carbons from Nitrogen Adsorption Measurements. *Carbon* **1989**, *27*, 853-861.
155. Lastoskie, C.; Gubbins, K. E.; Quirke, N., Pore Size Distribution Analysis of Microporous Carbons: A Density Functional Theory Approach. *Journal of Physical Chemistry* **1993**, *97*, 4786-4796.
156. Cimino, R. T.; Kowalczyk, P.; Ravikovitch, P. I.; Neimark, A. V., Determination of Isosteric Heat of Adsorption by Quenched Solid Density Functional Theory. *Langmuir* **2017**, *33*, 1769-1779.
157. Kresge, C. T.; Leonowicz, M. E.; Roth, W. J.; Vartuli, J. C.; Beck, J. S., Ordered Mesoporous Molecular Sieves Synthesized by a Liquid-Crystal Template Mechanism. *Nature* **1992**, *359*, 710-712.

158. Thommes, M., Physical Adsorption Characterization of Ordered and Amorphous Mesoporous Materials. In *Nanoporous Materials: Science and Engineering*, Imperial College Press 2004; Vol. Volume 4, pp 317-364.
159. Schwieger, W.; Machoke, A. G.; Weissenberger, T.; Inayat, A.; Selvam, T.; Klumpp, M.; Inayat, A., Hierarchy Concepts: Classification and Preparation Strategies for Zeolite Containing Materials with Hierarchical Porosity. *Chem. Soc. Rev.* **2016**, *45*, 3353-3376.
160. Pérez-Ramírez, J.; Christensen, C. H.; Egeblad, K.; Christensen, C. H.; Groen, J. C., Hierarchical Zeolites: Enhanced Utilisation of Microporous Crystals in Catalysis by Advances in Materials Design. *Chem. Soc. Rev.* **2008**, *37*, 2530-2542.
161. Hartmann, M.; Schwieger, W., Hierarchically-Structured Porous Materials: From Basic Understanding to Applications. *Chem. Soc. Rev.* **2016**, *45*, 3311-3312.
162. Mason, G.; Everett, D. H., A Model of Adsorption-Desorption Hysteresis in Which Hysteresis Is Primarily Developed by the Interconnections in a Network of Pores. *Proceedings of the Royal Society of London. A. Mathematical and Physical Sciences* **1983**, *390*, 47-72.
163. Ruiz-Martínez, J.; Beale, A. M.; Deka, U.; O'Brien, M. G.; Quinn, P. D.; Mosselmans, J. F. W.; Weckhuysen, B. M., Correlating Metal Poisoning with Zeolite Deactivation in an Individual Catalyst Particle by Chemical and Phase-Sensitive X-Ray Microscopy. *Angew. Chem. Int. Ed.* **2013**, *52*, 5983-5987.
164. Vogt, E. T. C.; Weckhuysen, B. M., Fluid Catalytic Cracking: Recent Developments on the Grand Old Lady of Zeolite Catalysis. *Chem. Soc. Rev.* **2015**, *44*, 7342-7370.
165. Peng, S.; Hu, Q.-H.; Dultz, S.; Zhang, M., Using X-Ray Computed Tomography in Pore Structure Characterization for a Berea Sandstone: Resolution Effect. *Journal of Hydrology* **2012**, *s 472–473*, 254–261.
166. Janssen, A. H.; Koster, A. J.; de Jong, K. P., Three-Dimensional Transmission Electron Microscopic Observations of Mesopores in Dealuminated Zeolite Y. *Angew. Chem. Int. Ed.* **2001**, *40*, 1102-1104.
167. de Jong, K. P.; Zečević, J.; Friedrich, H.; de Jongh, P. E.; Bulut, M.; van Donk, S.; Kenmogne, R.; Finiels, A.; Hulea, V.; Fajula, F., Zeolite Y Crystals with Trimodal Porosity as Ideal Hydrocracking Catalysts. *Angew. Chem. Int. Ed.* **2010**, *49*, 10074-10078.
168. Rao, K. S., Hysteresis in Sorption. I. Permanence of the Hysteresis Loop. Titania Gel Water System. *J. Phys. Chem.* **1941**, *45*, 500-506.
169. Rao, K. S., Hysteresis in Sorption. Ii. Scanning of the Hysteresis Loop. Titania Gel-Water System. *J. Phys. Chem.* **1941**, *45*, 506-512.
170. Rao, K. S., Hysteresis in Sorption. Iii. Permanence and Scanning of the Hysteresis Loop. Silica Gel–Water System. *J. Phys. Chem.* **1941**, *45*, 513-517.
171. Tompsett, G. A.; Krogh, L.; Griffin, D. W.; Conner, W. C., Hysteresis and Scanning Behavior of Mesoporous Molecular Sieves. *Langmuir* **2005**, *21*, 8214-8225.
172. Riedel, R.; Mera, G.; Hauser, R.; Klonczynski, A., Silicon-Based Polymer-Derived Ceramics: Synthesis Properties and Applications-a Review Dedicated to Prof. Dr. Fritz Aldinger on the Occasion of His 65th Birthday. *J. Ceram. Soc. Jpn.* **2006**, *114*, 425-444.
173. Colombo, P., *Polymer Derived Ceramics: From Nano-Structure to Applications*; DEStech Publications, 2010.
174. Lu, P.; Huang, Q.; Liu, B.; Bando, Y.; Hsieh, Y.-L.; Mukherjee, A. K., Macroporous Silicon Oxycarbide Fibers with Luffa-Like Superhydrophobic Shells. *J. Am. Chem. Soc.* **2009**, *131*, 10346-10347.

175. Wilamowska-Zawlocka, M.; Puczkarski, P.; Grabowska, Z.; Kaspar, J.; Graczyk-Zajac, M.; Riedel, R.; Sorarù, G. D., Silicon Oxycarbide Ceramics as Anodes for Lithium Ion Batteries: Influence of Carbon Content on Lithium Storage Capacity. *RSC Advances* **2016**, *6*, 104597-104607.
176. Assefa, D.; Zera, E.; Campostrini, R.; Soraru, G. D.; Vakifahmetoglu, C., Polymer-Derived Sioc Aerogel with Hierarchical Porosity through Hf Etching. *Ceram. Int.* **2016**, *42*, 11805-11809.
177. Soraru, G. D.; Dalcanale, F.; Campostrini, R.; Gaston, A.; Blum, Y.; Carturan, S.; Aravind, P. R., Novel Polysiloxane and Polycarbosilane Aerogels Via Hydrosilylation of Preceramic Polymers. *J. Mater. Chem.* **2012**, *22*, 7676-7680.
178. Pradeep, V. S. Study of Silicon Oxycarbide (Sioc) as Anode Materials for Li-Ion Batteries. Ph.D., University of Trento, Trento, Italy, 2013.
179. Downey, J. S.; McIsaac, G.; Frank, R. S.; Stöver, H. D. H., Poly(Divinylbenzene) Microspheres as an Intermediate Morphology between Microgel, Macrogel, and Coagulum in Cross-Linking Precipitation Polymerization. *Macromolecules* **2001**, *34*, 4534-4541.
180. Tamayo, A.; Mazo, M. A.; Roberto, R.-C.; Martin-Illana, A.; Bedoya, L.; Veiga, M.; Rubio, J., Mesoporous Silicon Oxycarbide Materials for Controlled Drug Delivery Systems. *Chem. Eng. J.* **2015**, *280*.
181. Vakifahmetoglu, C.; Zeydanli, D.; Ozalp, V. C.; Borsa, B. A.; Soraru, G. D., Hierarchically Porous Polymer Derived Ceramics: A Promising Platform for Multidrug Delivery Systems. *Materials & Design* **2018**, *140*, 37-44.
182. M Rosenholm, J.; Sahlgren, C.; Lindén, M., Multifunctional Mesoporous Silica Nanoparticles for Combined Therapeutic, Diagnostic and Targeted Action in Cancer Treatment. *Curr. Drug Targets* **2011**, *12*, 1166-1186.
183. Konegger, T.; Williams, L. F.; Bordia, R. K., Planar, Polysilazane-Derived Porous Ceramic Supports for Membrane and Catalysis Applications. *J. Am. Ceram. Soc.* **2015**, *98*, 3047-3053.
184. Pradeep, V. S.; Ayana, D. G.; Graczyk-Zajac, M.; Soraru, G. D.; Riedel, R., High Rate Capability of Sioc Ceramic Aerogels with Tailored Porosity as Anode Materials for Li-Ion Batteries. *Electrochim. Acta* **2015**, *157*, 41-45.
185. Aguirre-Medel, S.; Jana, P.; Kroll, P.; Sorarù, G. D., Towards Porous Silicon Oxycarbide Materials: Effects of Solvents on Microstructural Features of Poly (Methylhydrosiloxane)/Divynilbenzene Aerogels. *Materials* **2018**, *11*, 2589.
186. Schneider, C. A.; Rasband, W. S.; Eliceiri, K. W., Nih Image to Imagej: 25 Years of Image Analysis. *Nat. Methods* **2012**, *9*, 671-675.
187. Luisa Ojeda, M.; Marcos Esparza, J.; Campero, A.; Cordero, S.; Kornhauser, I.; Rojas, F., On Comparing Bjh and Nldft Pore-Size Distributions Determined from N2 Sorption on Sba-15 Substrata. *PCCP* **2003**, *5*, 1859-1866.
188. Jagiello, J.; Ania, C.; Parra, J. B.; Cook, C., Dual Gas Analysis of Microporous Carbons Using 2d-Nldft Heterogeneous Surface Model and Combined Adsorption Data of N2 and Co2. *Carbon* **2015**, *91*, 330-337.
189. Morishige, K.; Ishino, M., Lower Closure Point of Adsorption Hysteresis in Ordered Mesoporous Silicas. *Langmuir* **2007**, *23*, 11021-11026.
190. Bertier, P., et al., On the Use and Abuse of N2 Physisorption for the Characterisation of the Pore Structure of Shales. *CMS Workshop Lectures* **2016**, *21*, 151–161.
191. Rouquerol, F.; Rouquerol, J.; Sing, K. S.; Llewellyn, P.; Maurin, G., *Adsorption by Powders and Porous Solids : Principles, Methodology and Applications*, 2014.
192. Everett, D. H.; Parfitt, G. D.; Sing, K. S.; Wilson, R., The Sci/Iupac/Npl Project on Surface Area Standards. *J. App. Chem. Biotech.* **1974**, *24*, 199-219.

193. Choma, J.; Jaroniec, M., Determination of the Specific Surface Areas of Non-Porous and Macroporous Carbons. *Adsorption Science & Technology* **2001**, *19*, 765-776.
194. Lang, J. C.; Kenvin, J.; Lee, J. T.; Jiang, J.; Armstrong, D. W., Structural Changes in Chromatographic Supports with Modifidation by Covalently Bound Selectors. ISCC & GCxGC International Meeting, 2017.
195. Seaton, N., Determination of the Connectivity of Porous Solids from Nitrogen Sorption Measurements. *Chem. Eng. Sci.* **1991**, *46*, 1895-1909.
196. Park, J. T.; Roh, D. K.; Patel, R.; Kim, E.; Ryu, D. Y.; Kim, J. H., Preparation of Tio 2 Spheres with Hierarchical Pores Via Grafting Polymerization and Sol–Gel Process for Dye-Sensitized Solar Cells. *J. Mater. Chem.* **2010**, *20*, 8521-8530.
197. Sun, J.-H.; Shan, Z.; Maschmeyer, T.; Coppens, M.-O., Synthesis of Bimodal Nanostructured Silicas with Independently Controlled Small and Large Mesopore Sizes. *Langmuir* **2003**, *19*, 8395-8402.
198. Nakanishi, K., Pore Structure Control of Silica Gels Based on Phase Separation. *J. Porous Mater.* **1997**, *4*, 67-112.
199. Tanaka, H.; Hiratsuka, T.; Nishiyama, N.; Mori, K.; Miyahara, M. T., Capillary Condensation in Mesoporous Silica with Surface Roughness. *Adsorption* **2013**, *19*, 631-641.
200. Chatterjee, A.; Kalia, R. K.; Nakano, A.; Omeltchenko, A.; Tsuruta, K.; Vashishta, P.; Loong, C.-K.; Winterer, M.; Klein, S., Sintering, Structure, and Mechanical Properties of Nanophase Sic: A Molecular-Dynamics and Neutron Scattering Study. *Appl. Phys. Lett.* **2000**, *77*, 1132-1134.
201. Hackley, V. A.; Anderson, M. A.; Spooner, S., A Small-Angle X-Ray Scattering Study of Microstructure Evolution During Sintering of Sol-Gel-Derived Porous Nanophase Titania. *J. Mater. Res.* **1992**, *7*, 2555-2571.
202. Brinker, C. J.; Scherer, G. W., Sol→ Gel→ Glass: I. Gelation and Gel Structure. *J. Non-Cryst. Solids* **1985**, *70*, 301-322.
203. Taheri, P.; Bokka, A.; Asgari, P.; Jeon, J.; Lang, J. C.; Campostrini, R.; Sorarù, G. D.; Kroll, P., Novel Sulfur-Containing Cross-Linking Agent for Si-Based Preceramic Polymers. *Macromolecular Chemistry and Physics* **2020**, *221*, 1900380.
204. Sommer, L. H.; Pietrusza, E. W.; Whitmore, F. C., Peroxide-Catalyzed Addition of Trichlorosilane to 1-Octene. *Journal of the American Chemical Society* **1947**, *69*, 188-188.
205. Speier, J. L.; Webster, J. A.; Barnes, G. H., The Addition of Silicon Hydrides to Olefinic Double Bonds .2. The Use of Group-Viii Metal Catalysts. *Journal of the American Chemical Society* **1957**, *79*, 974-979.
206. Karstedt, B. D. Platinum Complexes of Unsaturated Siloxanes and Platinum Containing Organopolysiloxanes. 1973.
207. Diez-Gonzalez, S.; Nolan, S. P., Copper, Silver, and Gold Complexes in Hydrosilylation Reactions. *Accounts of Chemical Research* **2008**, *41*, 349-358.
208. Marciniec, B., Asymmetric Hydrosilylation of Unsaturated Carbon–Heteroatom Bonds. In *Hydrosilylation: A Comprehensive Review on Recent Advances*, Marciniec, B., Ed. Springer Netherlands: 2009; Vol. 1, pp 341-398.
209. Troegel, D.; Stohrer, J., Recent Advances and Actual Challenges in Late Transition Metal Catalyzed Hydrosilylation of Olefins from an Industrial Point of View. *Coordination Chemistry Reviews* **2011**, *255*, 1440-1459.
210. Radovanovic, E.; Gozzi, M. F.; Gonçalves, M. C.; Yoshida, I. V. P., Silicon Oxycarbide Glasses from Silicone Networks. *Journal of Non-Crystalline Solids* **1999**, *248*, 37-48.

211. Modena, S.; Sorarù, G. D.; Blum, Y.; Raj, R., Passive Oxidation of an Effluent System: The Case of Polymer-Derived Sico. *Journal of the American Ceramic Society* **2005**, *88*, 339-345.
212. Liu, X.; Li, Y.-L.; Hou, F., Fabrication of Sioc Ceramic Microparts and Patterned Structures from Polysiloxanes Via Liquid Cast and Pyrolysis. *Journal of the American Ceramic Society* **2009**, *92*, 49-53.
213. Soraru, G.; Dalcanale, F.; Renzo Campostrini, a.; Gaston, A.; Blum, Y.; Carturan, S.; Parakkulam Ramaswamy, A., Novel Polysiloxane and Polycarbosilane Aerogels Via Hydrosilylation of Preceramic Polymers. *Journal of Materials Chemistry* **2012**, *22*, 7676–7680.
214. Blum, Y.; Macqueen, D. B.; Kleebe, H.-J., Synthesis and Characterization of Carbon-Enriched Silicon Oxycarbides. *Journal of the European Ceramic Society* **2005**, *25*, 143-149.
215. Kleebe, H.-J.; Blum, Y. D., Sioc Ceramic with High Excess Free Carbon. *Journal of the European Ceramic Society* **2008**, *28*, 1037-1042.
216. Nedunchezhian, S.; Sujith, R.; Kumar, R., Processing and Characterization of Polymer Precursor Derived Silicon Oxycarbide Ceramic Foams and Compacts. *Journal of Advanced Ceramics* **2013**, *2*, 318-324.
217. Zhao, N.; Feng, J.; Jiang, Y.; Feng, J., Preparation and Characterization of Si-C-O Aerogel Composites for Thermal Insulation. *Journal of the Chinese Ceramic Society* **2012**, *40*, 19081–19086.
218. Feng, J.; Xiao, Y.; Jiang, Y.; Feng, J., Synthesis, Structure, and Properties of Silicon Oxycarbide Aerogels Derived from Tetraethylortosilicate /Polydimethylsiloxane. *Ceramics International* **2015**, *41*, 5281-5286.
219. Fricke, J.; Emmerling, A., Aerogels. *Journal of the American Ceramic Society* **1992**, *75*, 2027-2035.
220. Pradeep, V. S.; Zera, E.; Graczyk-Zajac, M.; Riedel, R.; Soraru, G., Structural Design of Polymer-Derived Sioc Ceramic Aerogels for High-Rate Li Ion Storage Applications. *Journal of American Ceramic Society* **2016**, *99*, 2977-2983.
221. Aegerter, M. A., Leventis, Nicholas, Koebel, Matthias M. , *Aerogels Handbook*. Springer: New York, NY, 2011.
222. Blum, Y. Hydridosiloxanes as Precursors to Ceramic Products. 1994.
223. Su, D.; Li, Y.-L.; An, H.-J.; Liu, X.; Hou, F.; Li, J.-Y.; Fu, X., Pyrolytic Transformation of Liquid Precursors to Shaped Bulk Ceramics. *Journal of the European Ceramic Society* **2010**, *30*, 1503-1511.
224. A. Pena, M.; Sestelo, J.; A. Sarandeses, L., New Synthetic Applications of Indium Organometallics in Cross-Coupling Reactions. *Synthesis* **2005**, *3*, 485-492.
225. Lewis, L. N.; Stein, J.; Gao, Y.; Colborn, R. E.; Hutchins, G., Platinum Catalysts Used in the Silicones Industry. *Platinum Metals Review* **1997**, *41*, 66-75.
226. Schneider, C. A.; Rasband, W. S.; Eliceiri, K. W., Nih Image to Imagej: 25 Years of Image Analysis. *Nature Methods* **2012**, *9*, 671.
227. Colthup, N. B.; Daly, L. H.; Wiberley, S. E., In *Introduction to Infrared and Raman Spectroscopy (Third Edition)*, Colthup, N. B.; Daly, L. H.; Wiberley, S. E., Eds. Academic Press: 1990.
228. Silverstein, R. M.; Webster, F. X.; Kiemle, D. J.; Bryce, D. L., *Spectrometric Identification of Organic Compounds*, 2015.
229. Bio-Rad Laboratories, I., Spectrabase. http://spectrabase.com/spectrum/1I4NpffmiWI.
230. Liu, R.; Liu, Z., Polythiophene: Synthesis in Aqueous Medium and Controllable Morphology. *Chinese Science Bulletin* **2009**, *54*, 2028-2032.
231. Nyquist, R. A., *Interpreting Infrared, Raman, and Nuclear Magnetic Resonance Spectra*; Elsevier Science, 2001.
232. Goldstein, J., *Scanning Electron Microscopy and X-Ray Microanalysis*; Kluwer Academic/Plenum Publishers: New York, 2003.

233. Zhai, S.-R.; Zhang, L.; Zhai, B.; An, Q.-D., Facile Sol–Gel Synthesis of Thiol-Functionalized Materials from Teos-Mptms-Pmhs System. *Journal of Sol-Gel Science and Technology* **2012**, *61*, 23-33.
234. Dibandjo, P.; Dirè, S.; Babonneau, F.; Soraru, G. D., New Insights into the Nanostructure of High-C Sioc Glasses Obtained Via Polymer Pyrolysis. *Glass Technology - European Journal of Glass Science and Technology Part A* **2008**, *49*, 175-178.
235. Aguirre, S.; Jana, P.; Kroll, P.; Soraru, G., Towards Porous Silicon Oxycarbide Materials: Effects of Solvents on Microstructural Features of Poly(Methylhydrosiloxane)/Divynilbenzene Aerogels. *Materials (Basel)* **2018**, *11*, 2589-2599.
236. Nguyen, V. L.; Laidani, N. B.; Sorarù, G. D., N-Doped Polymer-Derived Si(N)Oc: The Role of the N-Containing Precursor. *Journal of Materials Research* **2015**, *30*, 770-781.
237. Brown, S. S.; Kendrick, T. C.; McVie, J.; Thomas, D. R., 4 - Silicones. In *Comprehensive Organometallic Chemistry Ii*, Abel, E. W.; Stone, F. G. A.; Wilkinson, G., Eds. Elsevier: Oxford, 1995; pp 111-135.
238. Campostrini, R.; D'Andrea, G.; Carturan, G.; Ceccato, R.; Sorarù, G. D., Pyrolysis Study of Methyl-Substituted Si—H Containing Gels as Precursors for Oxycarbide Glasses, by Combined Thermogravimetry, Gas Chromatographic and Mass Spectrometric Analysis. *Journal of Materials Chemistry* **1996**, *6*, 585-594.
239. Raj, R.; Pederiva, L.; Narisawa, M.; Soraru, G. D., On the Onset of Fracture as a Silicon-Based Polymer Converts into the Ceramic Phase. *Journal of the American Ceramic Society* **2019**, *102*, 924-929.
240. Campostrini, R.; Sicurelli, A.; Ischia, M.; Carturan, G., Pyrolysis Study of a Hydride-Sol-Gel Silica: Part I. Chemical Aspects. *Journal of Thermal Analysis and Calorimetry* **2007**, *89*, 633-641.
241. Campostrini, R.; Sicurelli, A.; Ischia, M.; Carturan, G., Pyrolysis Study of a Hydride-Sol-Gel Silica : Part Ii. Kinetic Aspects. *Journal of Thermal Analysis and Calorimetry* **2007**, *90*, 179-184.
242. Pantano, C. G.; Singh, A. K.; Zhang, H., Silicon Oxycarbide Glasses. *Journal of Sol-Gel Science and Technology* **1999**, *14*, 7-25.
243. Linstrom, P. J.; Mallard, W. G., *Nist Chemistry Webbook*; National Institute of Standards and Technology: Gaithersburg MD, 20899; Vol. 69.
244. Campostrini, R.; Ischia, M.; Palmisano, L., Pyrolysis Study of Sol-Gel Derived Tio2 Powders - Part I. Tio2-Anatase Prepared by Reacting Titanium(Iv) Isopropoxide with Formic Acid. *Journal of Thermal Analysis and Calorimetry* **2003**, *71*, 997-1009.
245. Campostrini, R.; Ischia, M.; Palmisano, L., Pyrolysis Study of Sol-Gel Derived Tio2 Powders - Part Ii. Tio2-Anatase Prepared by Reacting Titanium(Iv) Isopropoxide with Oxalic Acid. *Journal of Thermal Analysis and Calorimetry* **2003**, *71*, 1011-1021.
246. Campostrini, R.; Ischia, M.; Palmisano, L., Pyrolysis Study of Sol-Gel Derived Tio2 Powders - Part Iii. Tio2-Anatase Prepared by Reacting Titanium(Iv) Isopropoxide with Acetic Acid. *Journal of Thermal Analysis and Calorimetry* **2004**, *75*, 13-24.
247. Campostrini, R.; Ischia, M.; Palmisano, L., Pyrolysis Study of Sol-Gel Derived Tio2 Powders - Part Iv. Tio2-Anatase Prepared by Hydrolysing Titanium(Iv) Isopropoxide without Chelating Agents. *Journal of Thermal Analysis and Calorimetry* **2004**, *75*, 25-34.
248. Tamayo, A.; Rubio, J.; Rubio, F.; Oteo, J. L.; Riedel, R., Texture and Micro-Nanostructure of Porous Silicon Oxycarbide Glasses Prepared from Hybrid Materials Aged in Different Solvents. *Journal of the European Ceramic Society* **2011**, *31*, 1791-1801.
249. Gesser, H. D.; Goswami, P. C., Aerogels and Related Porous Materials. *Chemical Reviews* **1989**, *89*, 765-788.

250. Sinkó, K., Influence of Chemical Conditions on the Nanoporous Structure of Silicate Aerogels. *Materials* **2010**, *3*, 704-740.
251. Lee, D. H.; Jo, M. J.; Han, S. W.; Yu, S.; Park, H., Polyimide Aerogel with Controlled Porosity: Solvent-Induced Synergistic Pore Development During Solvent Exchange Process. *Polymer* **2020**, *205*, 122879.
252. Teo, N.; Jana, S. C., Solvent Effects on Tuning Pore Structures in Polyimide Aerogels. *Langmuir* **2018**, *34*, 8581-8590.
253. Pircher, N.; Carbajal, L.; Schimper, C.; Bacher, M.; Rennhofer, H.; Nedelec, J.-M.; Lichtenegger, H. C.; Rosenau, T.; Liebner, F., Impact of Selected Solvent Systems on the Pore and Solid Structure of Cellulose Aerogels. *Cellulose* **2016**, *23*, 1949-1966.
254. Kenvin, J.; Mitchell, S.; Sterling, M.; Warringham, R.; Keller, T. C.; Crivelli, P.; Jagiello, J.; Pérez-Ramírez, J., Quantifying the Complex Pore Architecture of Hierarchical Faujasite Zeolites and the Impact on Diffusion. *Advanced Functional Materials* **2016**, *26*, 5621-5630.
255. Rodponthukwaji, K.; Wattanakit, C.; Yutthalekha, T.; Assavapanumat, S.; Warakulwit, C.; Wannapakdee, W.; Limtrakul, J., Catalytic Upgrading of Carboxylic Acids as Bio-Oil Models over Hierarchical Zsm-5 Obtained Via an Organosilane Approach. *RSC Advances* **2017**, *7*, 35581-35589.
256. Mitchell, S.; Pinar, A. B.; Kenvin, J.; Crivelli, P.; Kärger, J.; Pérez-Ramírez, J., Structural Analysis of Hierarchically Organized Zeolites. *Nature Communications* **2015**, *6*, 8633.
257. Warringham, R.; Mitchell, S.; Murty, R.; Schäublin, R.; Crivelli, P.; Kenvin, J.; Pérez-Ramírez, J., Mapping the Birth and Evolution of Pores Upon Thermal Activation of Layered Hydroxides. *Chemistry of Materials* **2017**, *29*, 4052-4062.